

Chapter 1 Figure Legends

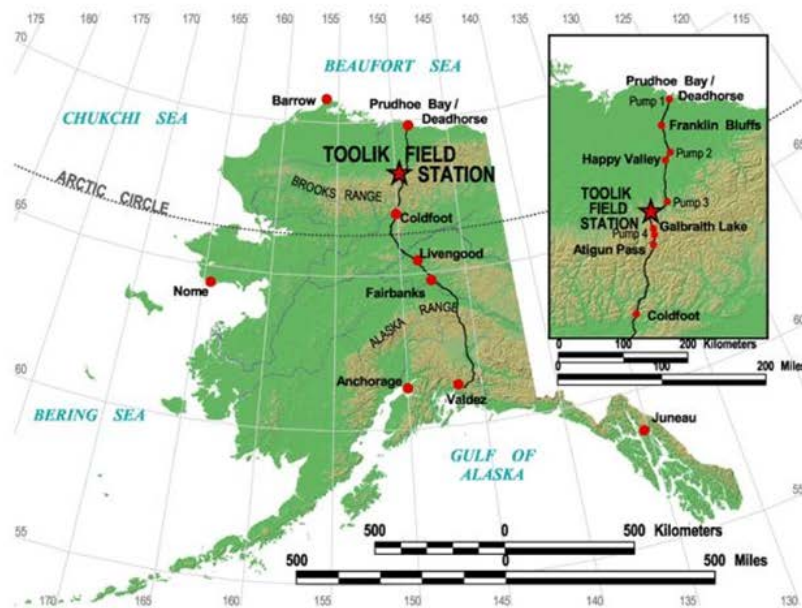
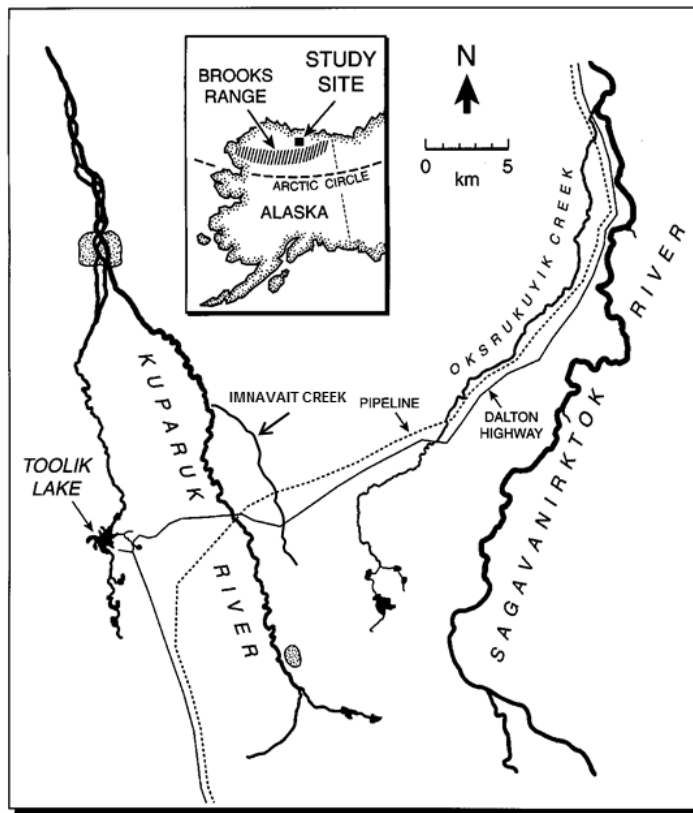


Fig. 1.1. Location of the Arctic LTER field site.



The Arctic LTER site is the upper Kuparuk River drainage basin. This includes the entire drainage basin of the river draining Toolik Lake. Measurements have also been made on Oksrukuyik Creek and along the Sag River

Fig. 1.2. Map of the Arctic LTER site (Toolik Lake, watersheds, Kuparuk River, Imnaviat Creek, Sagavanirktok River, and Oksrukuyik).

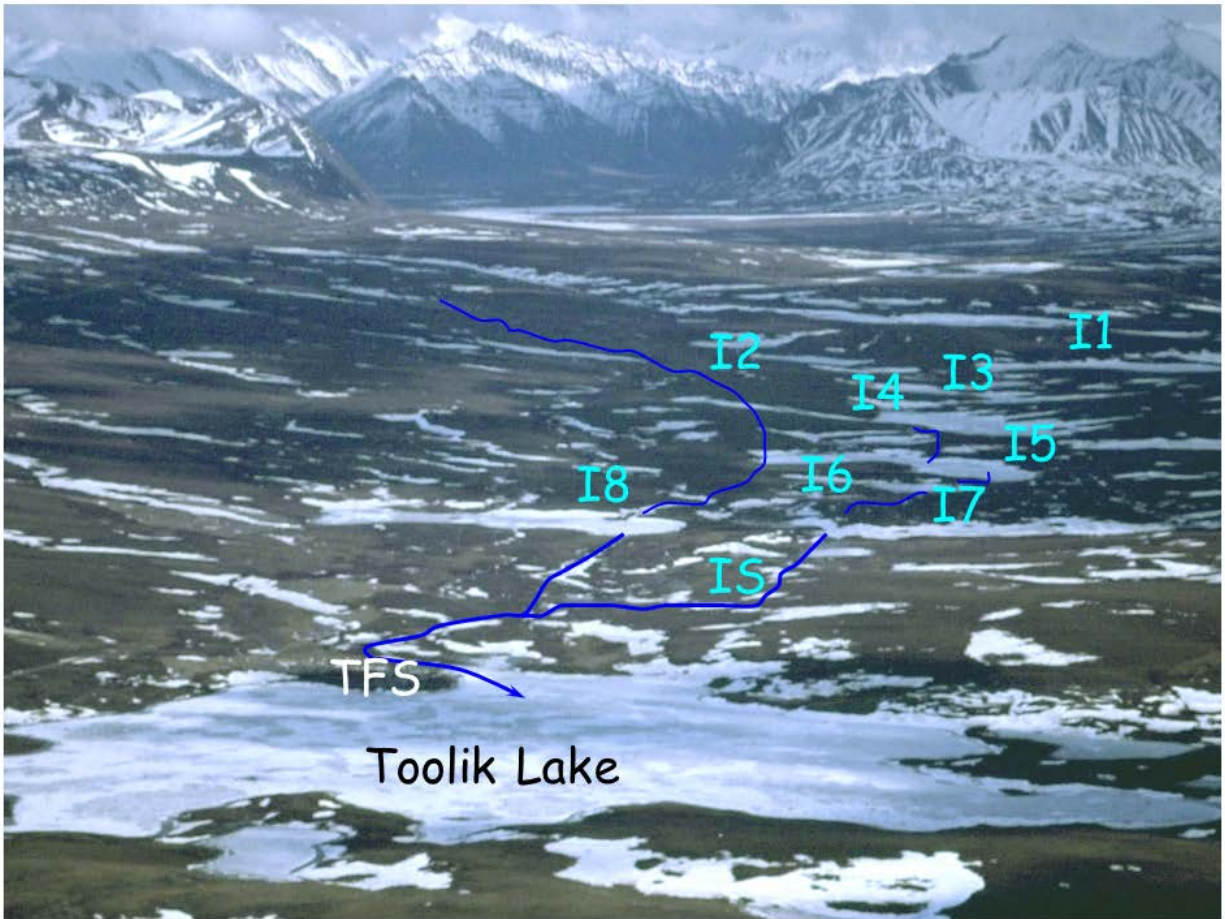


Fig. 1.3. Toolik Lake, the Toolik Field Station (TFS), inlet stream, inlet lakes (“I series”), and the Brooks Range.

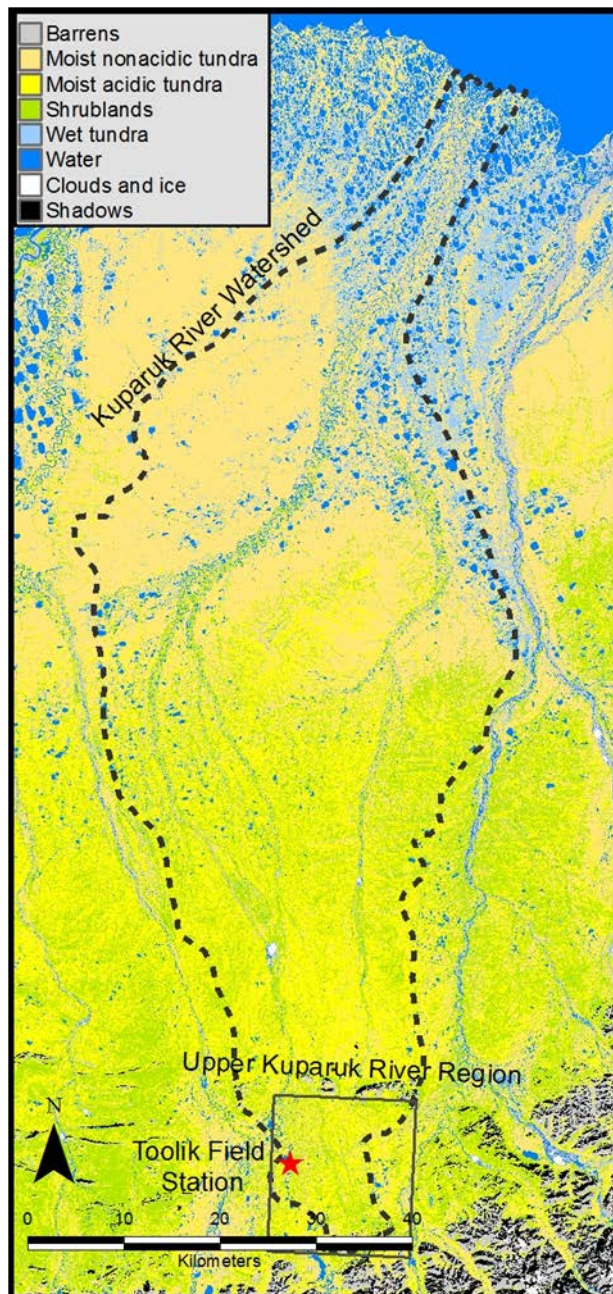


Fig. 1.4. The Kugaruk River watershed and the distribution of vegetation. Based on Muller et al. (1998).

METEOROLOGICAL INPUTS

June - August, 1995

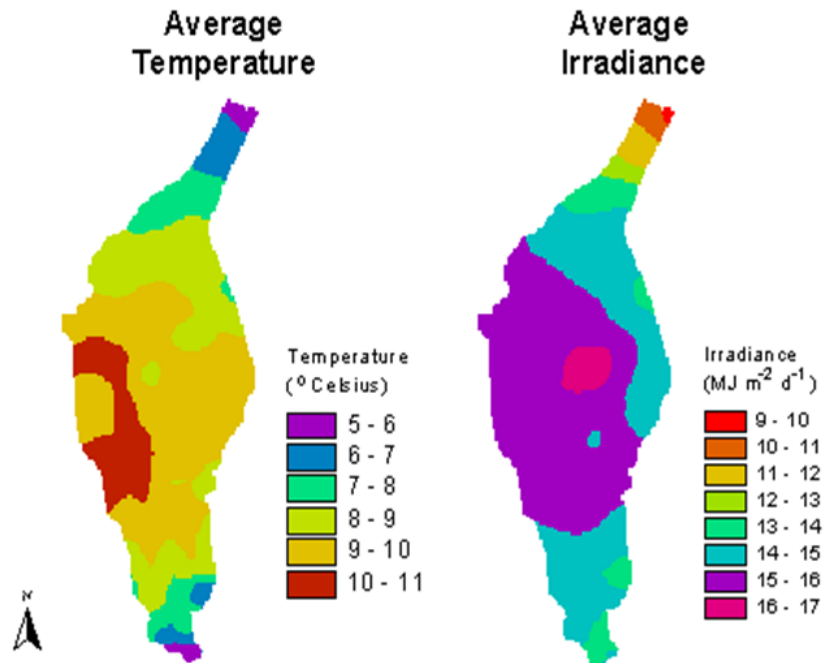


Fig. 1.5. Summer (June, July, August) average temperatures and irradiance in the Kugaruk River basin (data from Williams et al. 2001).

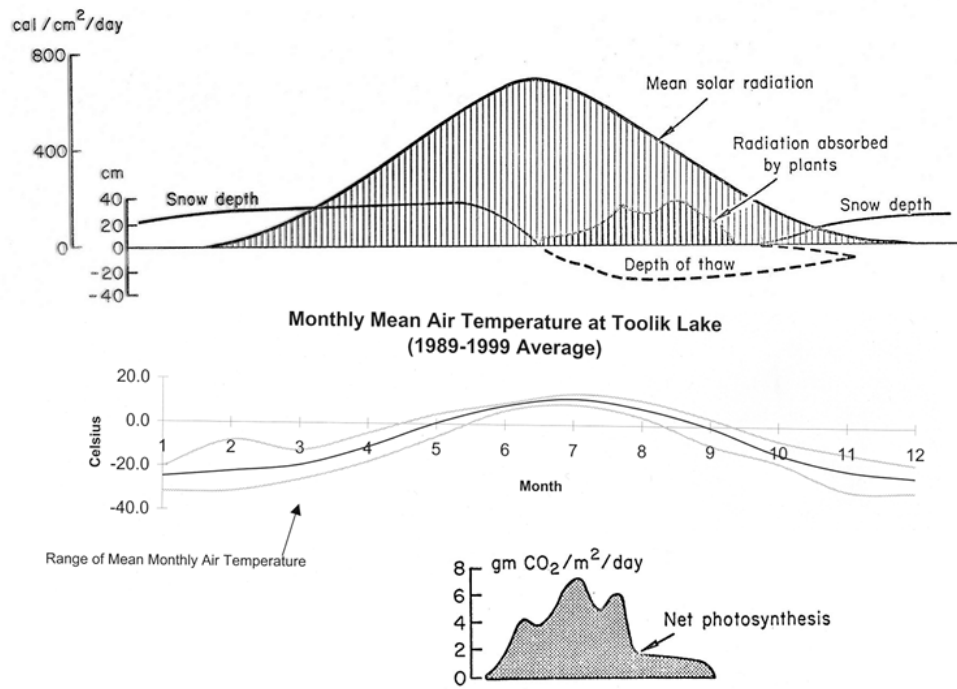


Fig. 1.6. Annual course of solar radiation, snow depth, depth of thaw, mean air temperatures, and net photosynthesis at Toolik Lake, Alaska.

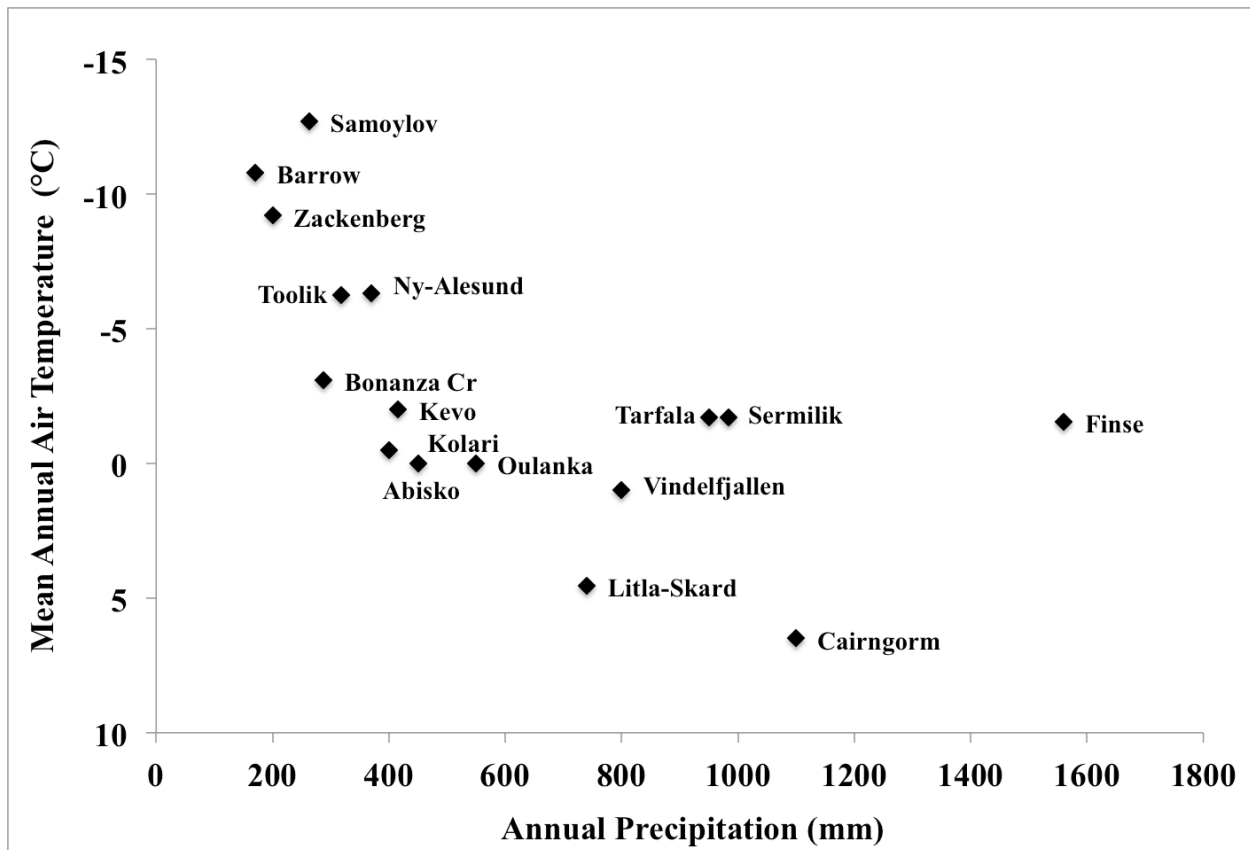


Fig. 1.7. Toolik Field Station mean annual air temperature and precipitation in relation to other northern field stations (see www.eu-interact.org for location). The site locations are Samoylov, Lena Delta, Siberia; Barrow, Alaska; Zackenberg, northeast Greenland; Ny-Alesund, Svalbard; Bonanza Creek, Fairbanks, Alaska; Kevo, Finland; Finse, Norway; Abisko, northern Sweden; Litla-Skard, Iceland.

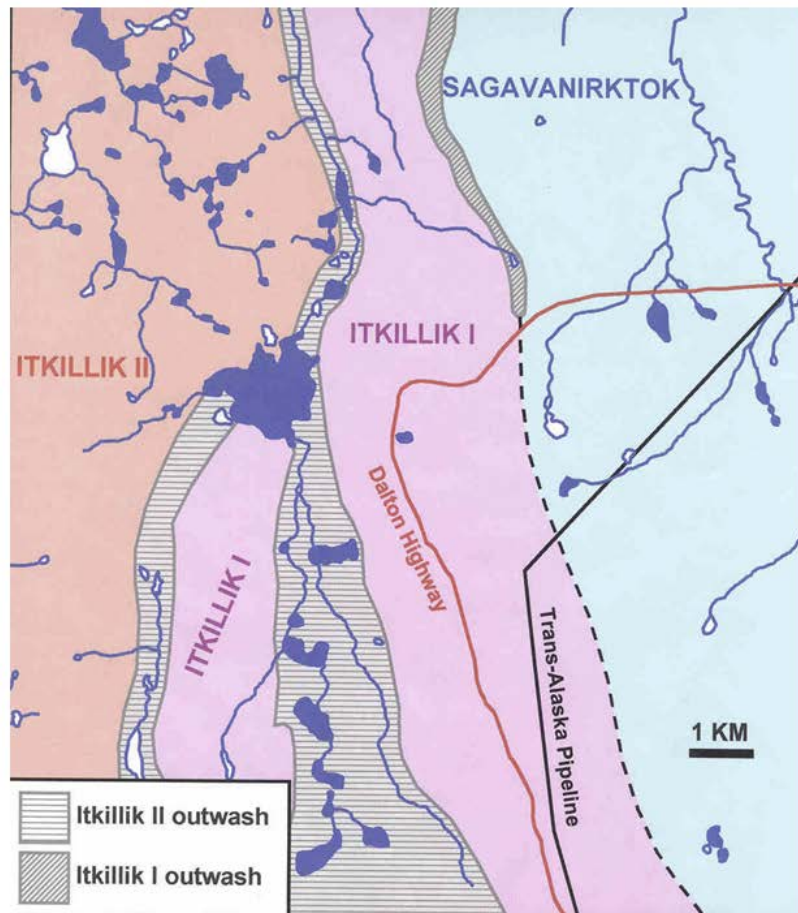


Fig. 1.8. The different ages of soils near the Arctic LTER site resulting from glacial advances northward from the valleys of the Brooks Range. Toolik is the large lake in the center of the picture. The Sagavanirktok advance was >300,000 years ago, the Itkillik I was ~60,000 years ago, and the Itkillik II was ~10,000 years ago. Based on map in Hamilton (2003).



Fig. 1.9. Long-term experiments in moist acidic tundra near Toolik Lake. The experimental treatments at this site are fertilization, heating, shading, and grazer exclusion.

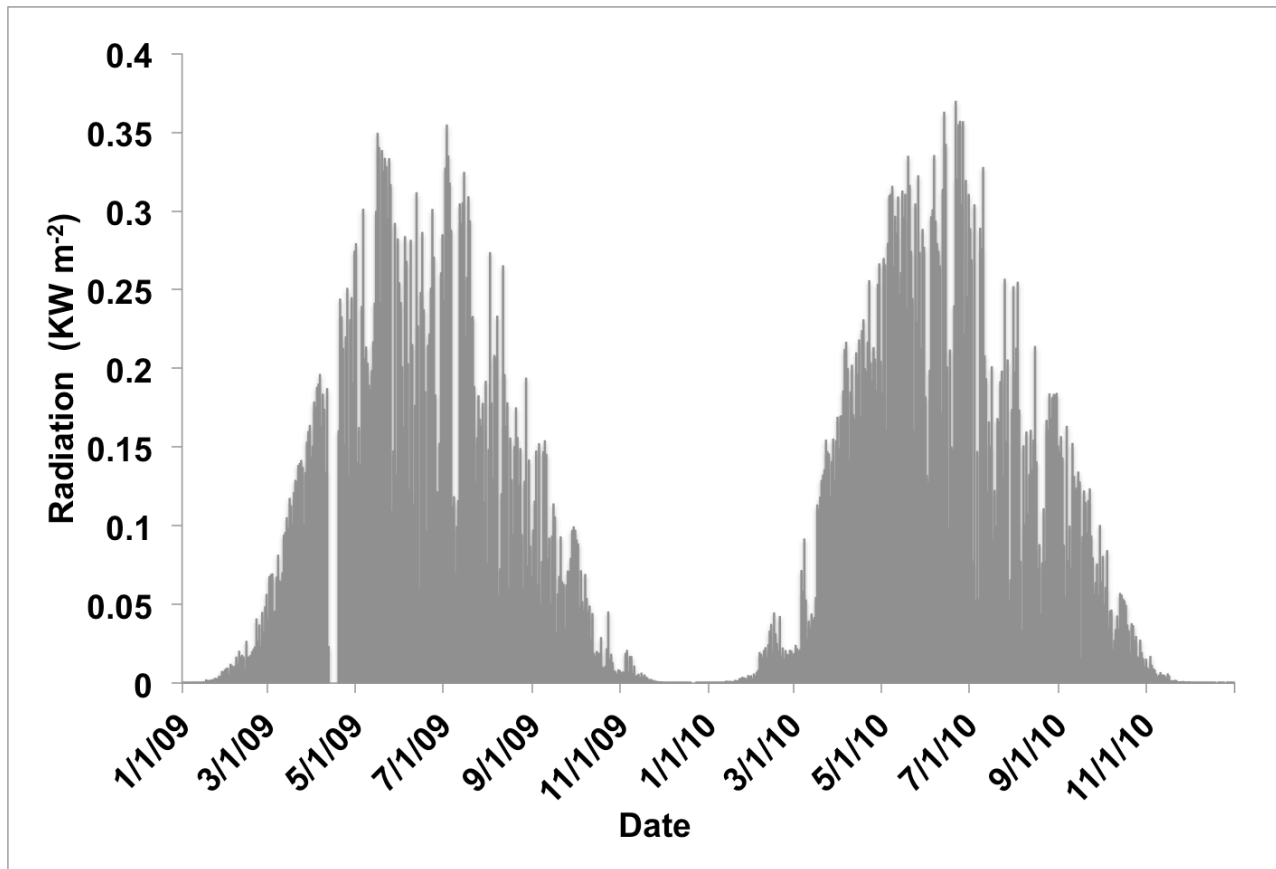


Fig. 2.1. Daily averaged incoming solar radiation at the Toolik LTER from 1 Jan 2009 to 31 Dec 2010.

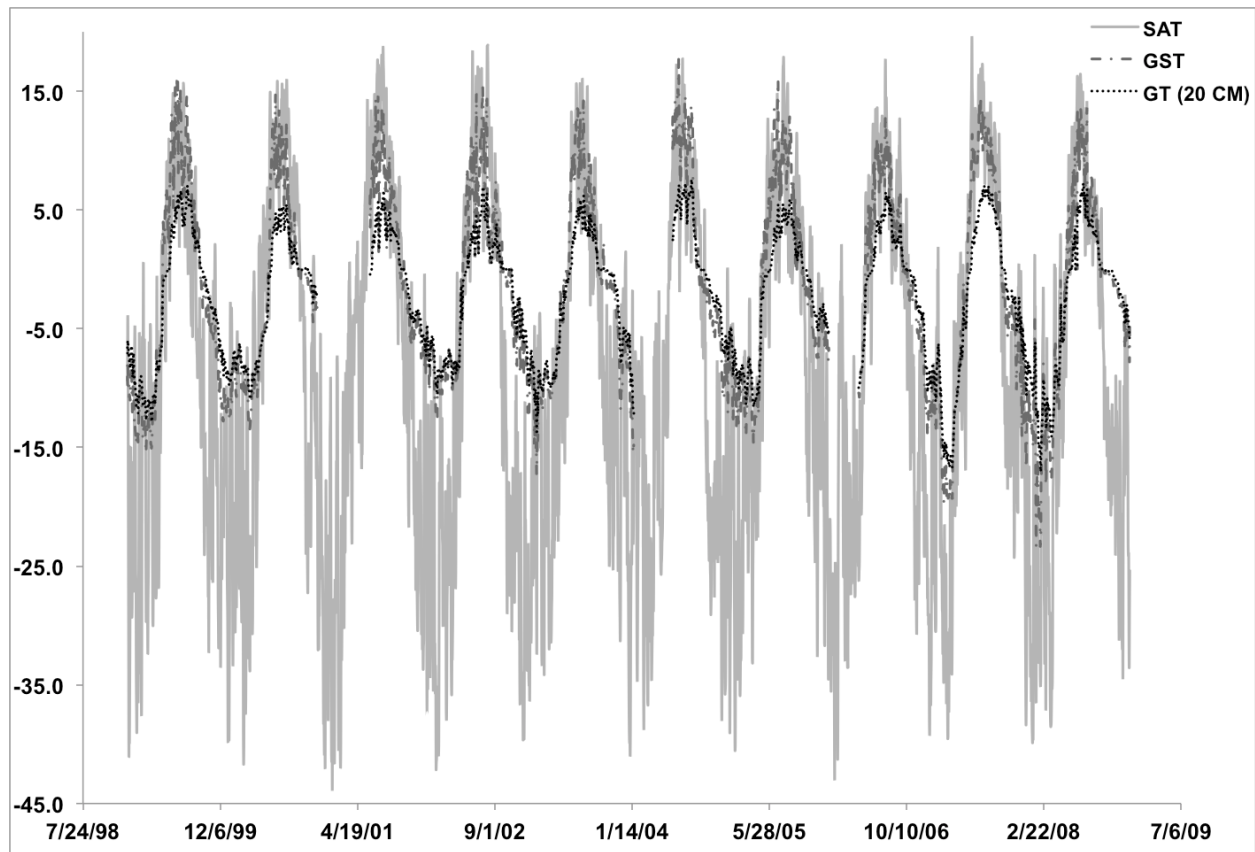


Fig. 2.2. Daily average surface air temperature (SAT, solid line), ground surface temperature (dot-dash line) and ground temperature at 20 cm depth (dotted line) at Toolik LTER from 1 Jan 1999 to 31 Dec 2008 (x-axis labeled as month/day/year).

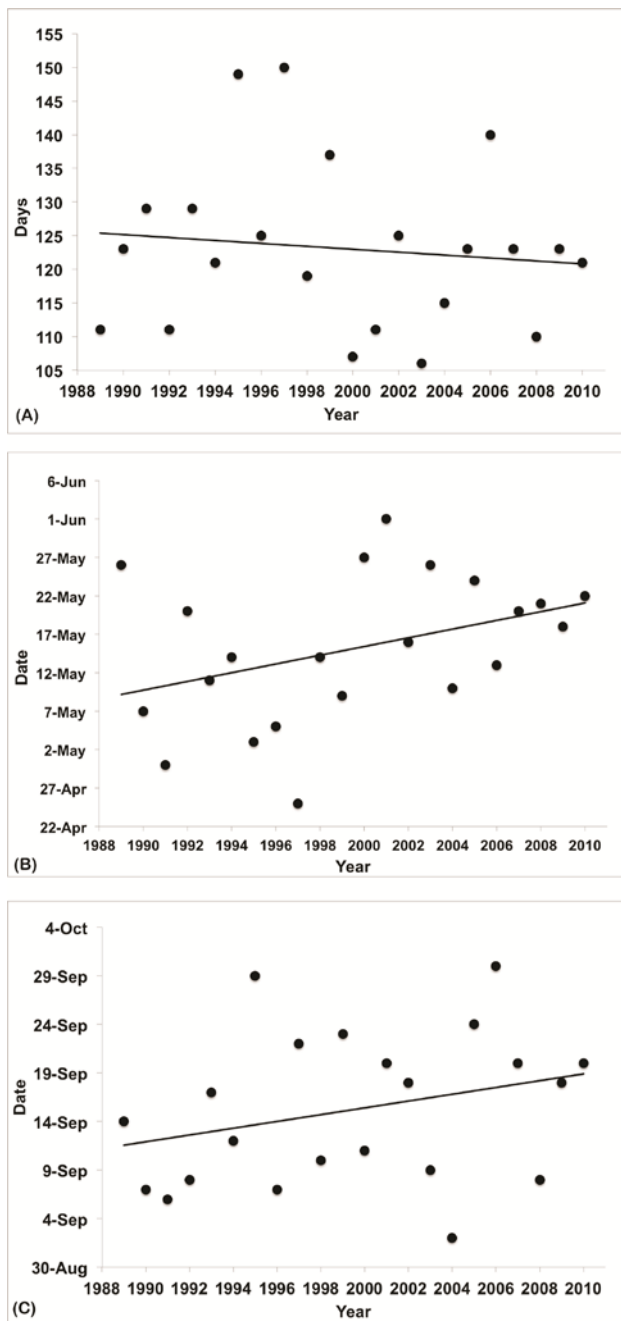


Fig. 2.3. (A) Length of growing season from 1989 to 2010; $R^2 = 0.013$, $p = 0.61$ fails student's t-test at confidence interval (CI) = 95%. (B) Start date of growing season from 1989 to 2010; $R^2 = 0.149$, $p = 0.08$ fails t-test at CI = 95%. (C) End date of growing season from 1989 to 2010; $R^2 = 0.085$, $p = 0.19$ fails t-test at CI = 95%.

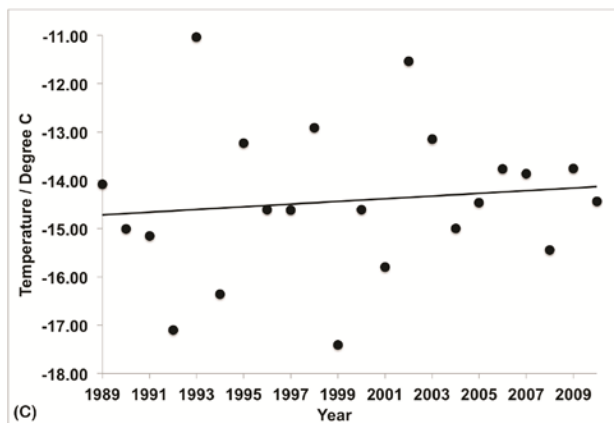
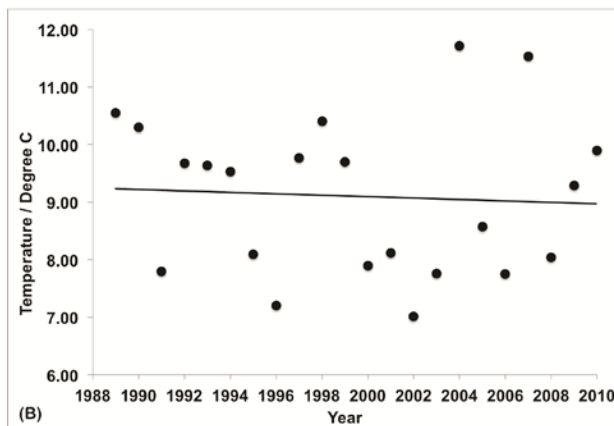
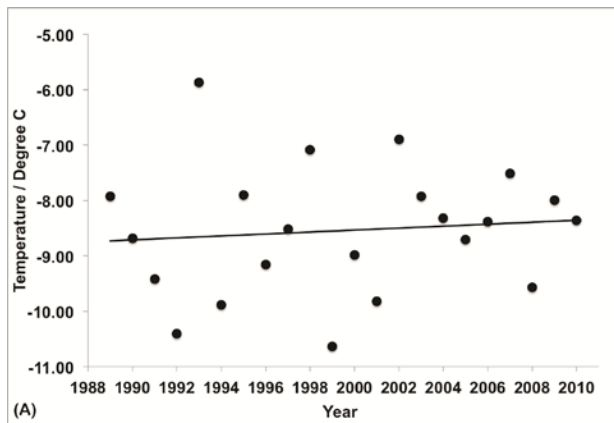


Fig. 2.4. (A) Annual mean Toolik LTER surface air temperature (SAT) at 1 m height from 1989 – 2010; $R^2 = 0.009$, $p = 0.66$ fails student's t-test at confidence interval (CI) = 95%. (B) Mean summer Toolik LTER SAT 1 m from 1989 – 2010; $R^2 = 0.003$, $p = 0.79$ fails t-test at CI = 95%. (C) Mean winter Toolik LTER SAT 1 m 1989 – 2010; $R^2 = 0.013$, $p = 0.61$ fails t-test at CI = 95%.

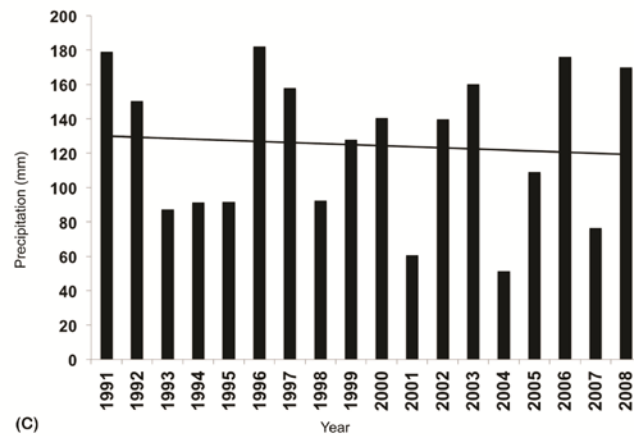
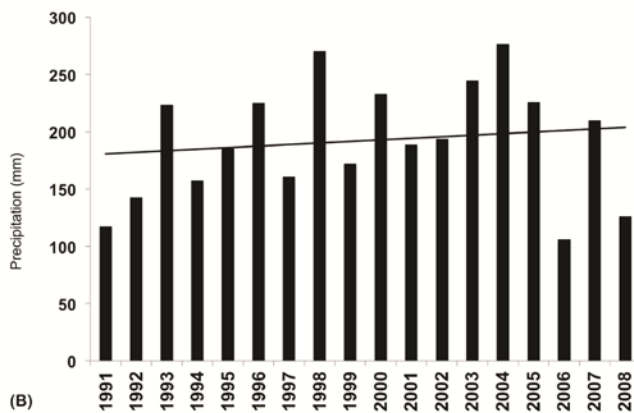
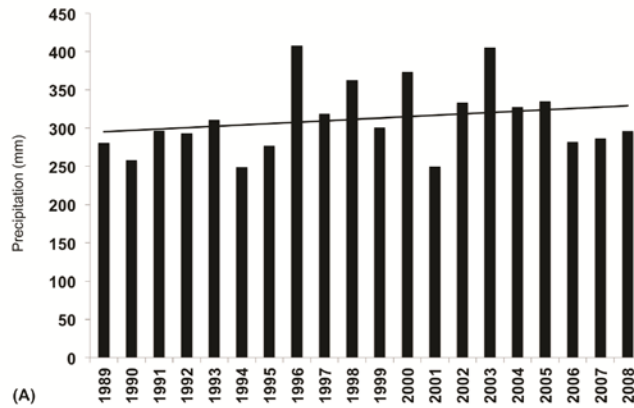


Fig. 2.5. (A) Annual mean Toolik LTER precipitation (mm) from 1989 – 2008; $R^2 = 0.053$, $p = 0.33$ fails student's t-test at confidence interval (CI) = 95%. (B) Mean summer precipitation (mm) from 1989 – 2008; $R^2 = 0.021$, $p = 0.25$ fails t-test at CI = 95%. (C) Mean winter precipitation (mm) 1989 – 2008; $R^2 = 0.006$, $p = 0.77$ fails t-test at CI = 95%.

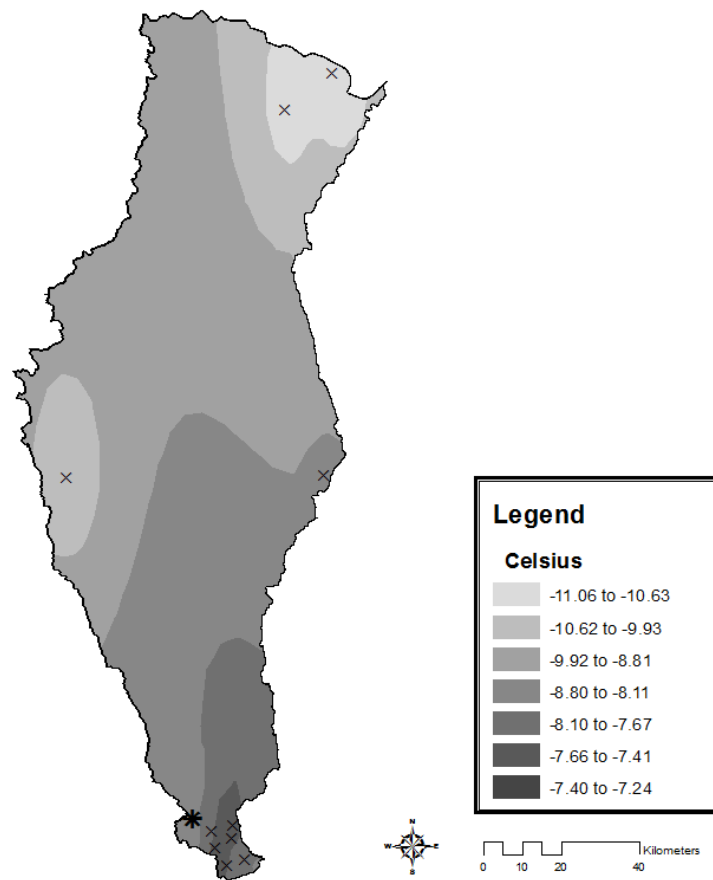


Fig. 2.6. Mean annual isotherms (°C) in the Kuparuk River Basin (bold outline), 1989 – 2012. The Toolik LTER is denoted by “*” and other meteorological stations by “+”.

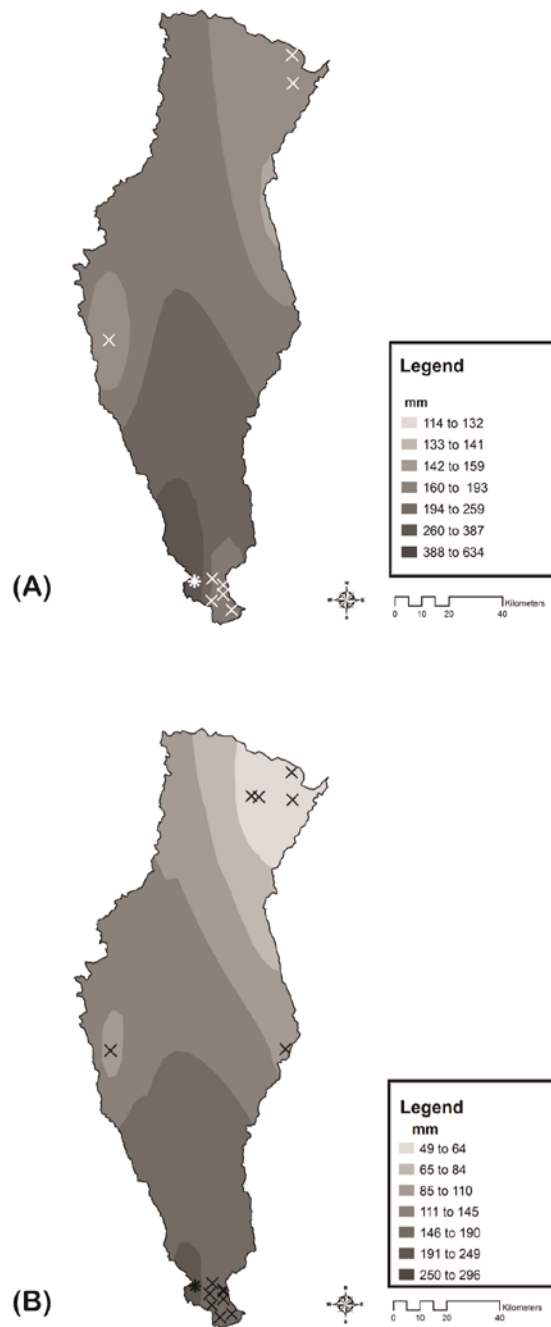


Fig. 2.7. Mean annual (A) and mean summer (B) isohyets (lines of constant precipitation, mm yr⁻¹) in the Kuparuk River Basin (bold outline), 1989 – 2010. The Arctic LTER is denoted by “*” and other meteorological stations by “+”.

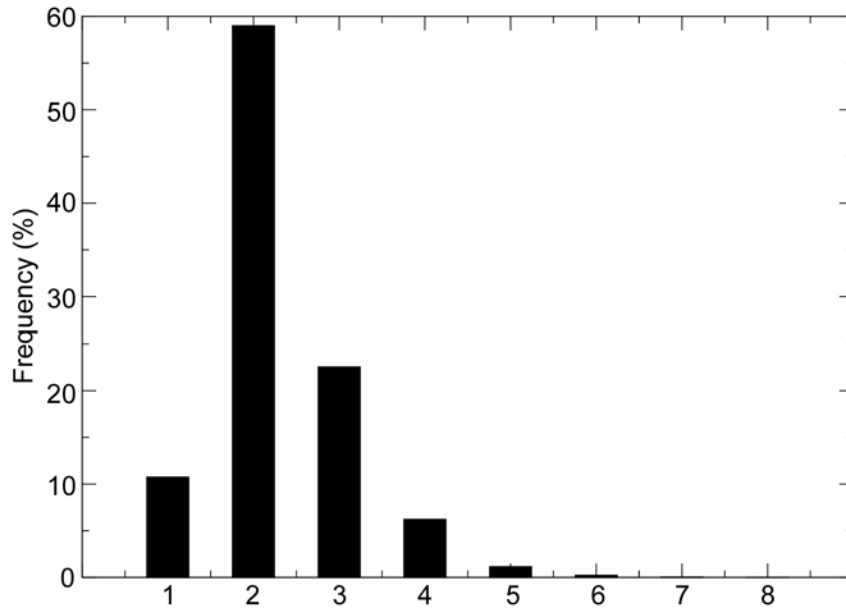


Fig. 2.8. Frequency histogram of wind speeds observed at the Arctic LTER, 1989 - 2010. The wind speed categories are as follows: 1 = $U < 1 \text{ m s}^{-1}$, 2 = $1 \text{ m s}^{-1} < U < 4 \text{ m s}^{-1}$, 3 = $4 \text{ m s}^{-1} < U < 7 \text{ m s}^{-1}$; 4 = $7 \text{ m s}^{-1} < U < 10 \text{ m s}^{-1}$, 5 = $10 \text{ m s}^{-1} < U < 13 \text{ m s}^{-1}$, 6 = $13 \text{ m s}^{-1} < U < 16 \text{ m s}^{-1}$, 7 = $16 \text{ m s}^{-1} < U < 19 \text{ m s}^{-1}$; 8 = $U > 19 \text{ m s}^{-1}$.

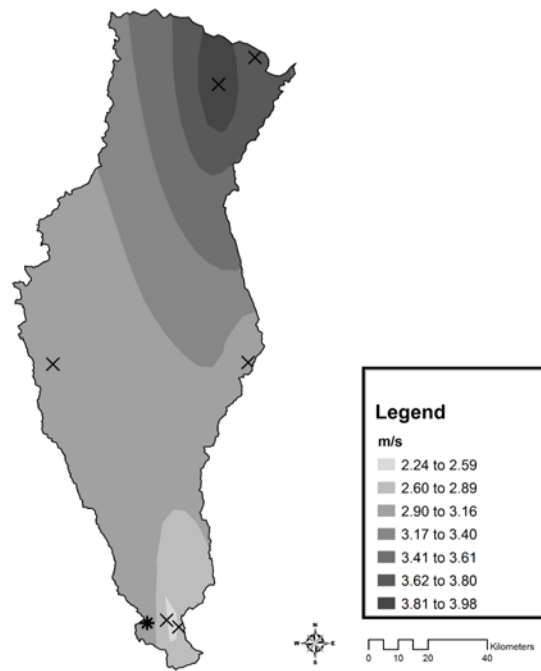


Fig. 2.9. Mean annual isotachs (lines of constant windspeed, m s^{-1}) in the Kuparuk River Basin (bold outline). The Arctic LTER is denoted by “*”.

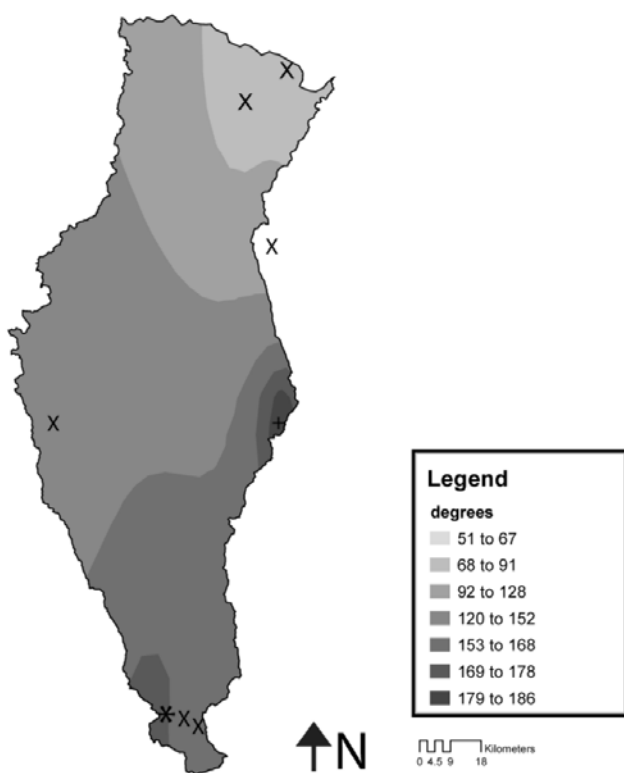


Fig. 2.10. Mean annual isogons (lines of constant wind direction, °) in the Kuparuk River Basin (bold outline). The Arctic LTER is denoted by “*”.

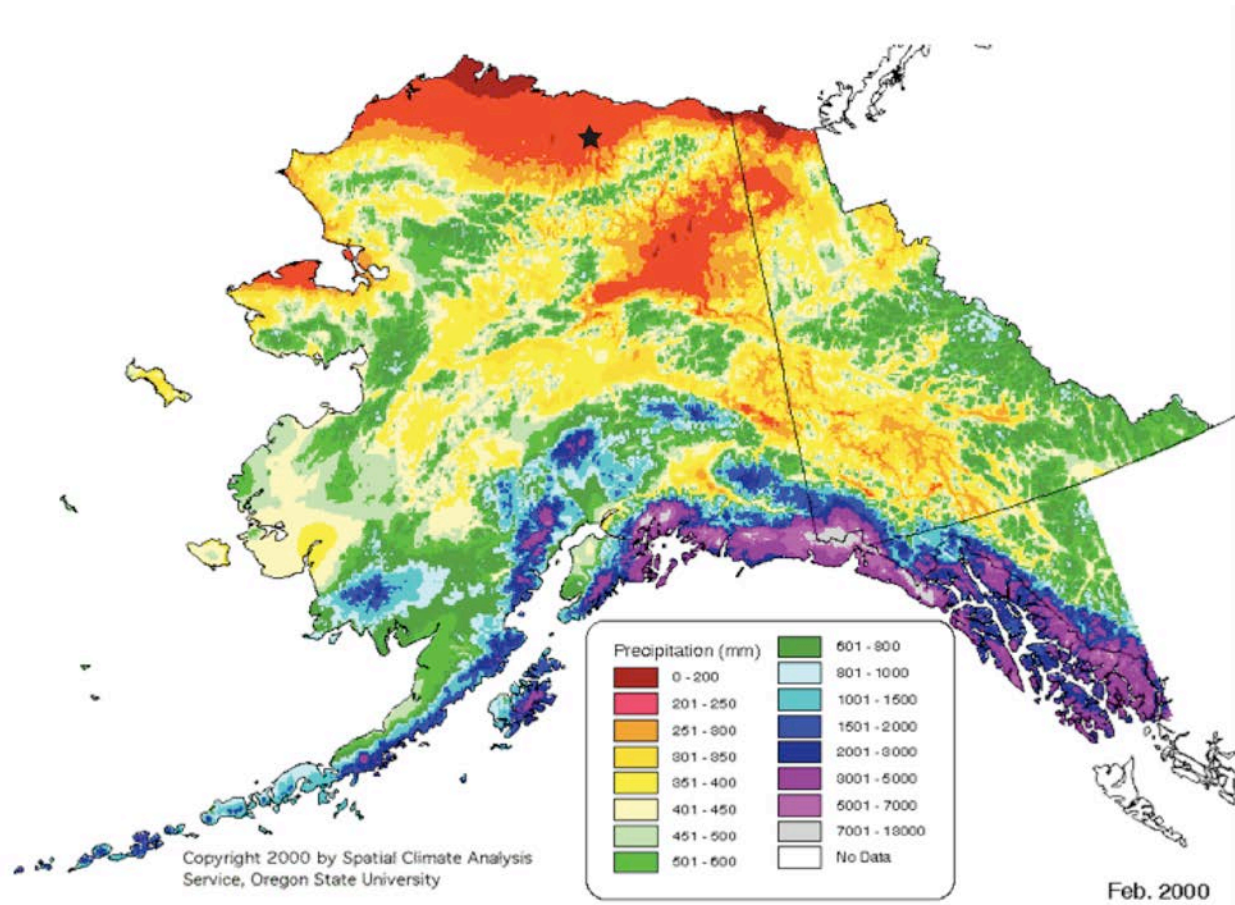


Fig. 2.11. Mean Annual Precipitation for 1961 – 2000 (with permission, copyright 2000, PRISM Climate Group, Oregon State University). Approximate location of the Toolik Field Station has been marked with a star.

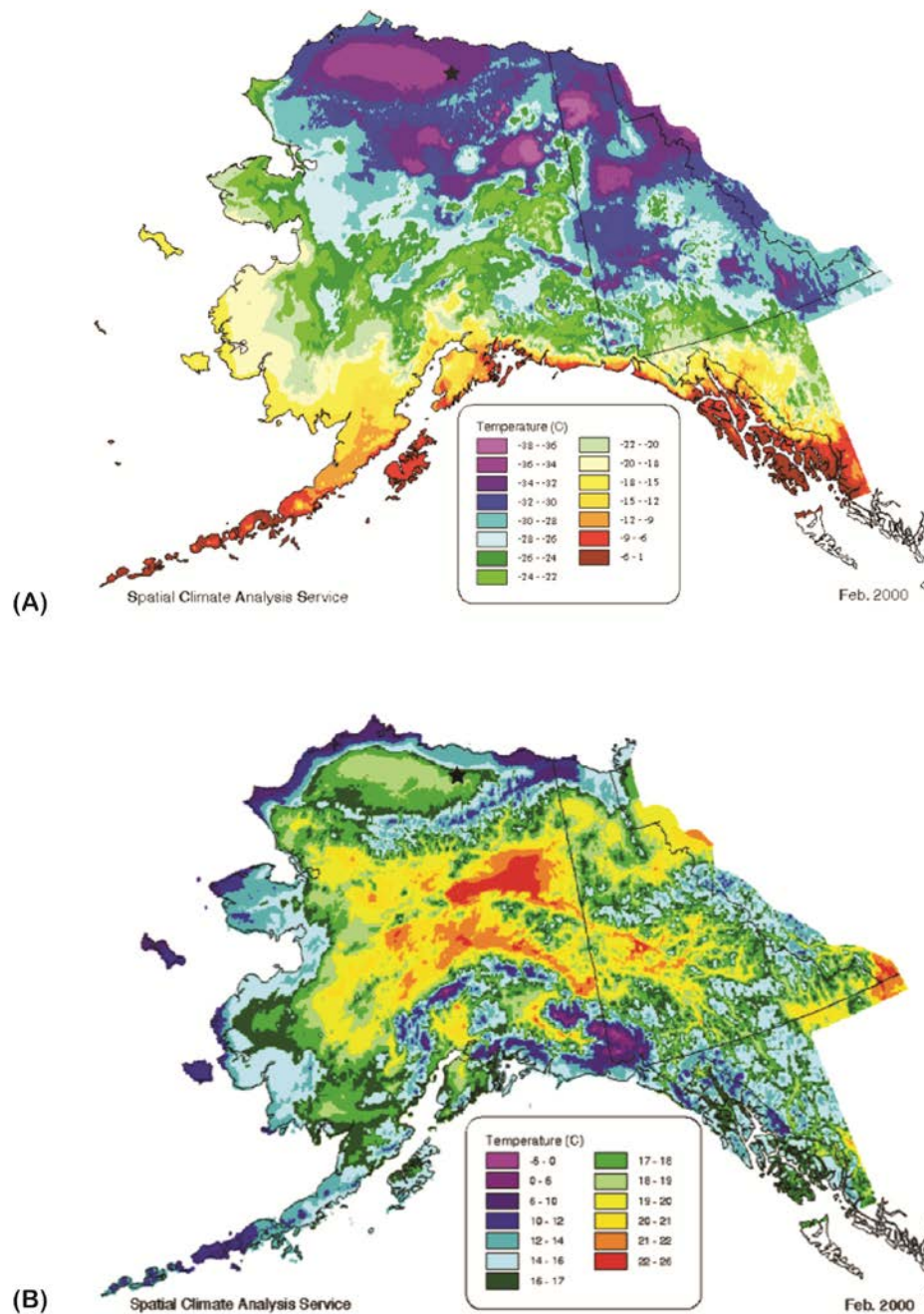


Fig. 2.12. (A) January Mean Minimum Temperature for 1961 – 2000. (B) July Mean Maximum Temperature for 1961-2000. Approximate location of the Toolik Field Station has been marked with a star. All with permission, copyright 2000, PRISM Climate Group, Oregon State University.

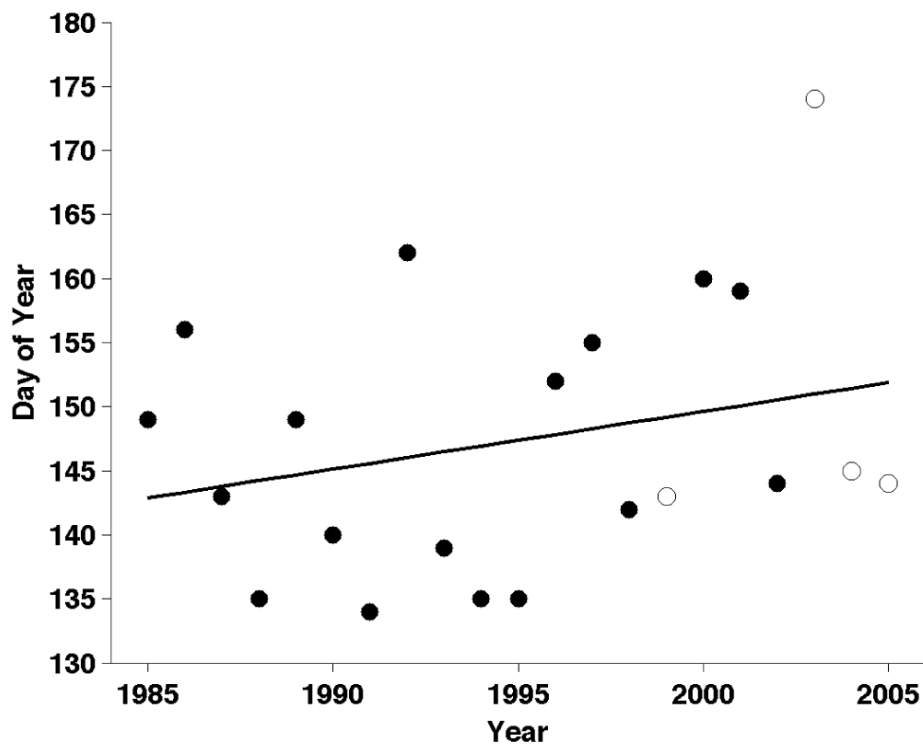


Fig. 2.13. The day of year on which snow melted away to bare ground in the Imnavait Basin. Data are from D. Kane and L. Hinzman (Pers. Comm.). Closed circles are end-of-snow season dates that were observed precisely. Open circles are inferred from observations taken within a few days of final melt. While these data show a trend of +0.45 days later melt per year, it is not statistically significant ($R^2 = 0.26$, $p = 0.25$ fails student's t-test with a 90% confidence interval).

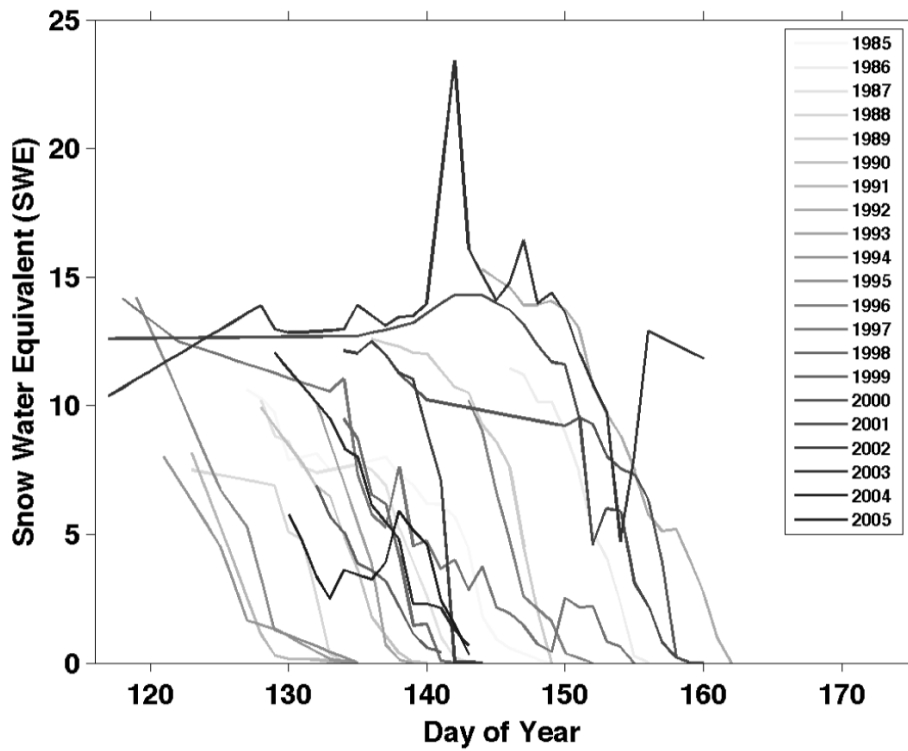


Fig. 2.14. Snowpack depletion curves (snow water equivalent versus day of year) for the Imnavait Basin. Data are from Kane and Hinzman (2007). These basin averages are calculated from fixed transects.

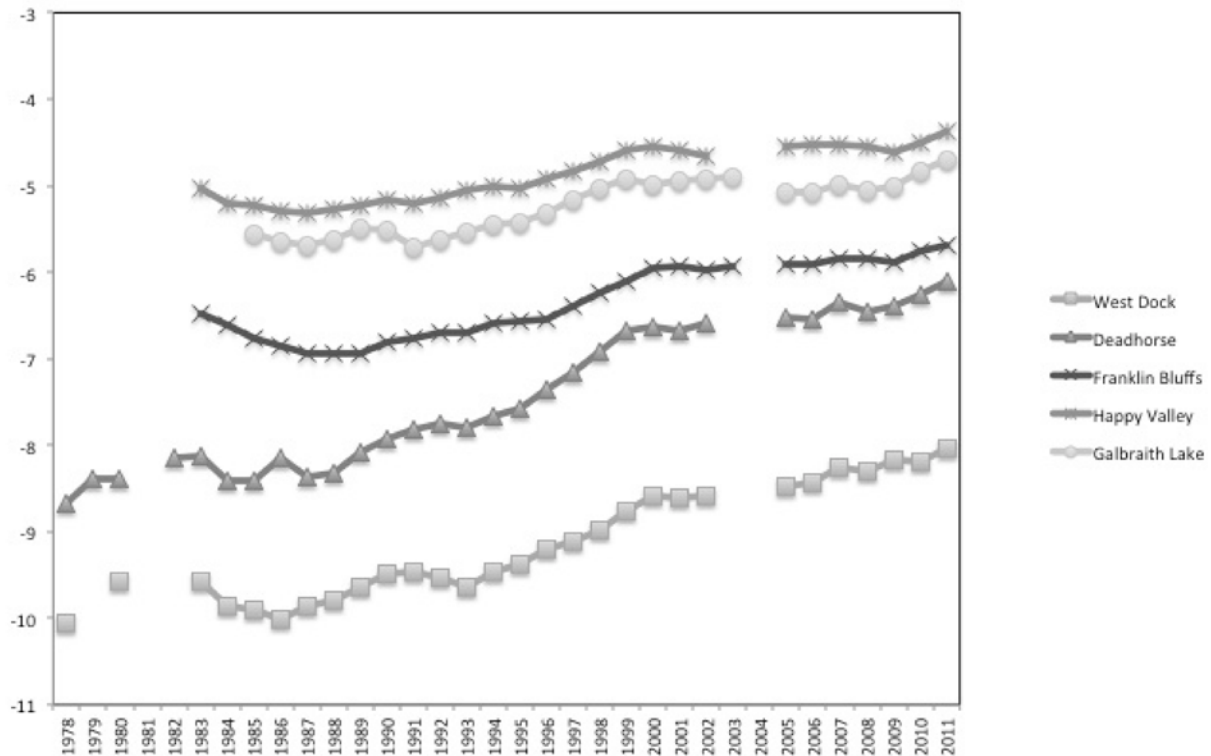


Fig. 2.15. Time series of permafrost temperatures measured in Alaska showing warming trends between 1983 and 2009. Measurements are at 20 m depths at several sites across the continuous permafrost zone. The Arctic LTER lies between Happy Valley (to the north) and Galbraith Lake (to the south). Source: Romanovsky and Osterkamp (2012).

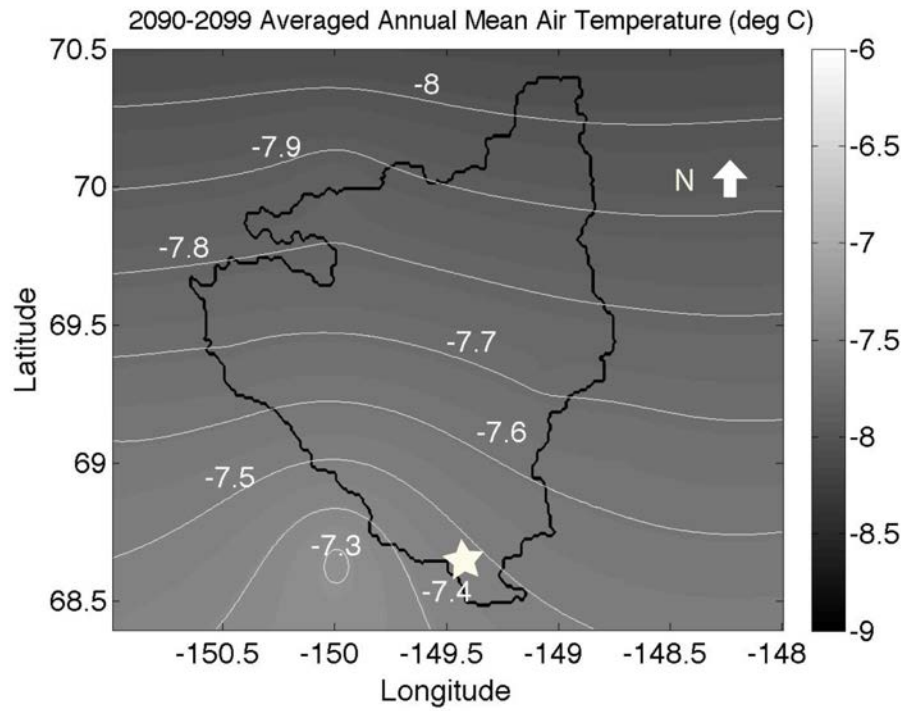


Fig. 2.16. Average annual mean surface air temperature for the Kuparuk River Basin between 2090 and 2099 predicted by 5 GCMs. The location of the Arctic LTER is marked by a star.

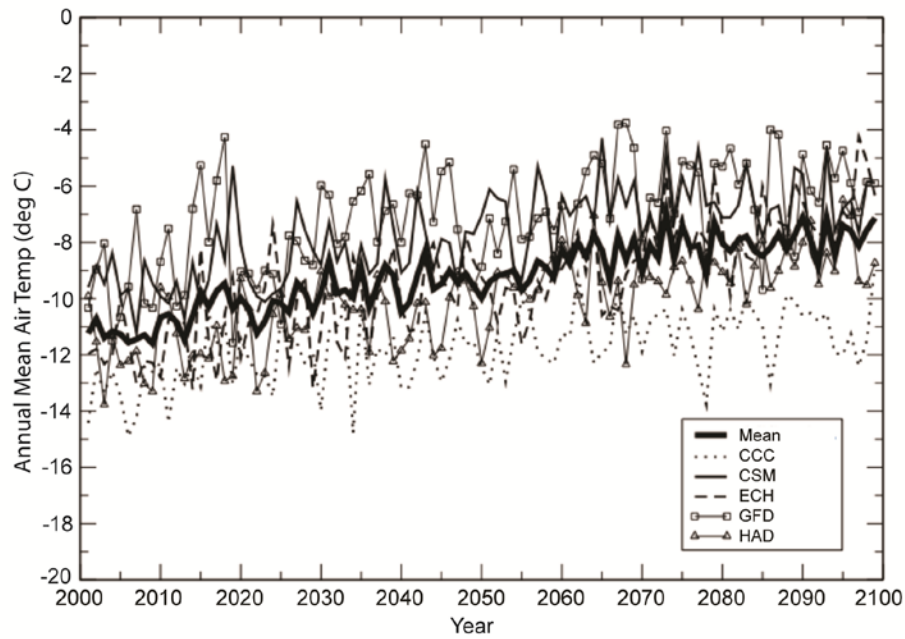


Fig. 2.17. Time series of annual mean surface air temperature over the Kuparuk River basin between 2001 and 2099 simulated by the CCC, CSM, ECH, GFD, and HAD models, and the multi-model mean.

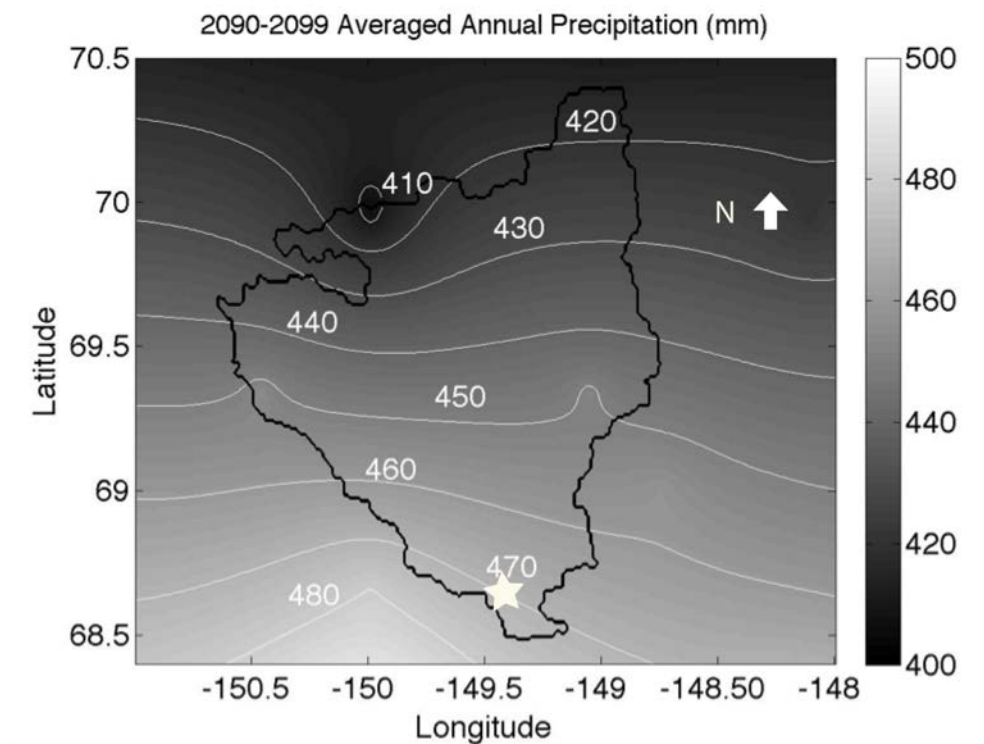


Fig. 2.18. Averaged annual precipitation (mm) between 2090 and 2099 predicted by five GCMs (CCC, CSM, ECH, GFD, and HAD). The location of the Arctic LTER is marked by a star.

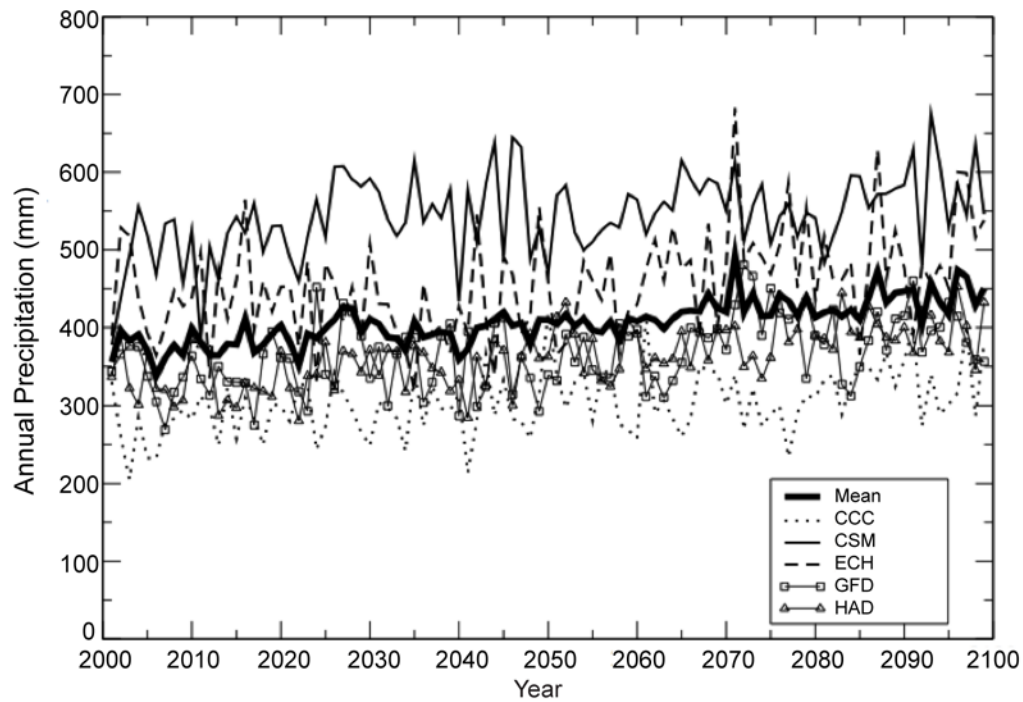


Fig. 2.19. Time series of annual precipitation predicted for the Kuparuk River basin between 2090 and 2099 simulated by five GCMs (CCC, CSM, ECH, GFD, HAD) and the multi-model mean.

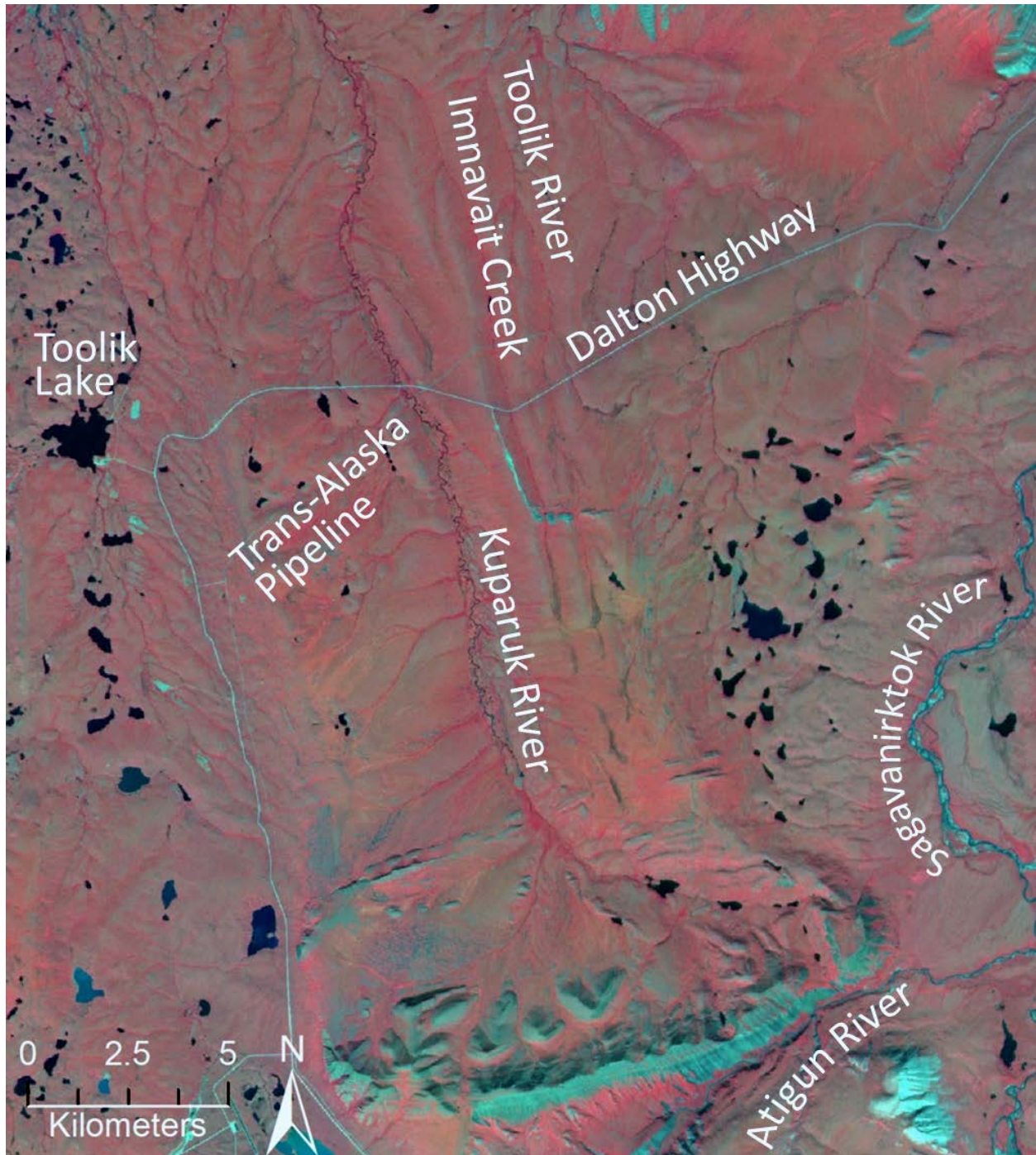


Fig. 3.1. False color-infrared SPOT satellite image of the mapped area in the Toolik Lake region. Surfaces glaciated during the Itkillik glaciations have a browner tone and numerous lakes, whereas areas glaciated during the older Sagavanirktok glaciation have a brighter red tone and

few lakes (see

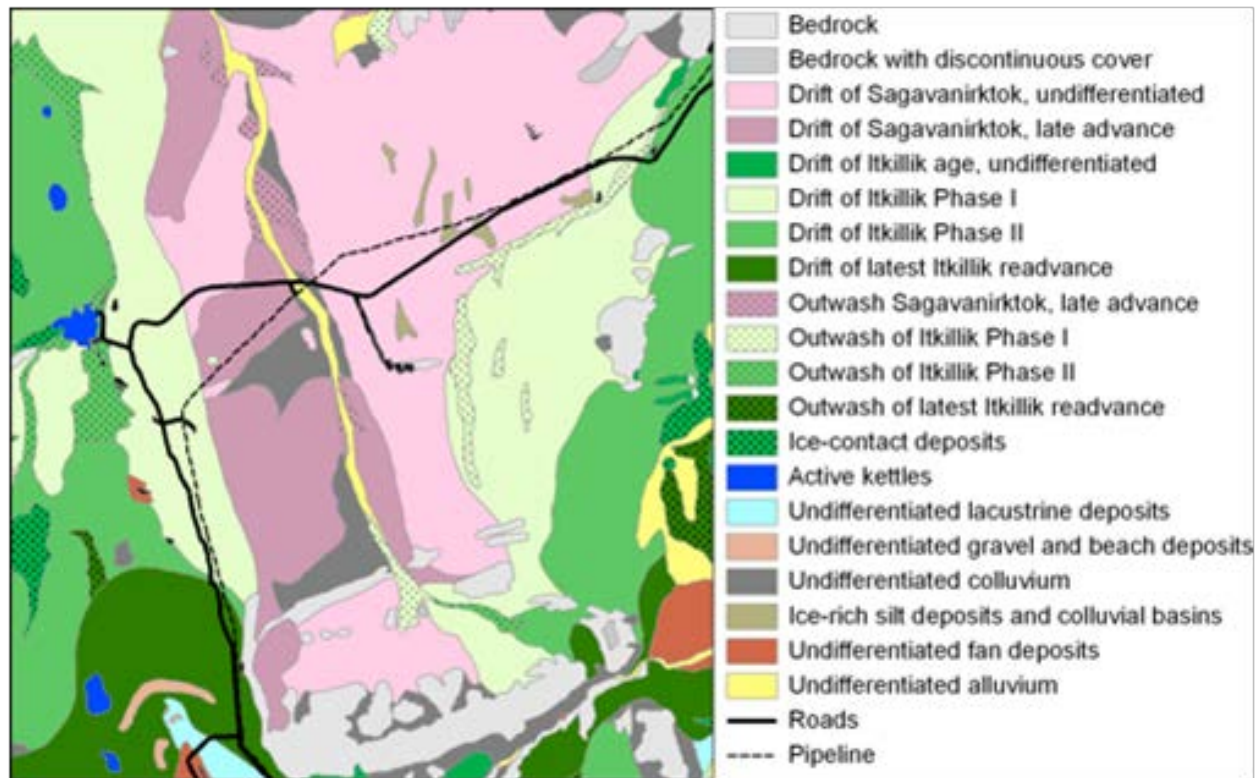


Fig. 3.2 for glacial boundaries). The brightest red areas, e.g., along streams and water tracks, are densely vegetated with shrubs. More intermediate red tones are generally tussock tundra with varying amounts of shrubs. The more brownish tones are less densely vegetated and include dry tundra, nonacidic tundra, and wet tundra. Rocky areas are either light colored, such as the limestone in the lower right corner or greenish gray as in the sandstones and conglomerates along the north side of the Atigun River. Image taken 28 July 1989. [INSERT COLOR IMAGE]

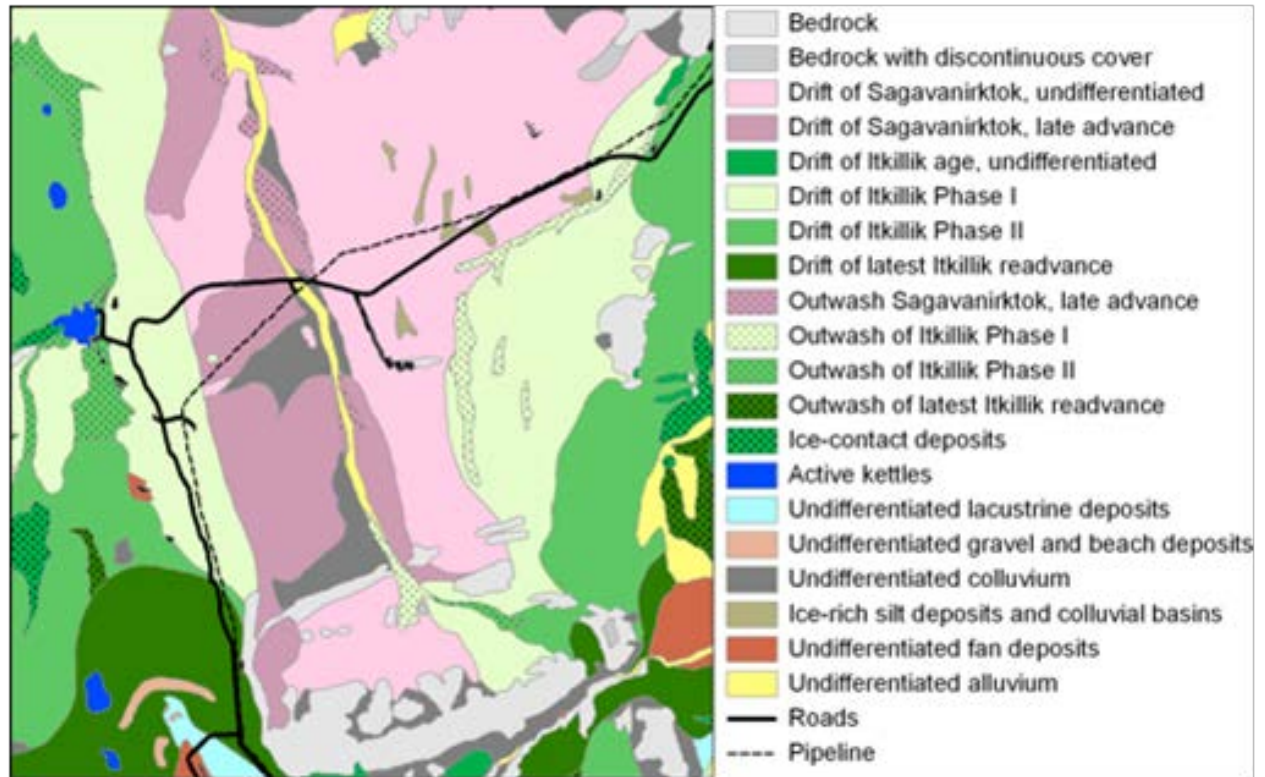


Fig. 3.2. Simplified glacial geology map of the Upper Kuparuk River region (based on Hamilton 2003a). [INSERT COLOR MAP]



Fig. 3.3. Glaciated terrain of Sagavanirktok and Itkillik-II age. Top – Sagavanirktok-age moraine, Imnavait Creek vicinity. Note long smooth flanking slopes and continuous vegetation cover broken only by dispersed large, weathered erratic boulders of resistant lithology. The vegetation is a rather homogeneous cover of tussock tundra. The cottongrass, *Eriophorum vaginatum*, is flowering profusely in this photo. Bottom - Drift and outwash surfaces of Itkillik II age, looking northeast from Jade Mountain, west of Toolik Lake. Note narrow moraine crests,

steep flanking slopes, and discontinuous vegetation cover on the moraine and kame features. Minor as well as major depositional features are well preserved. (Photos by D. A. Walker.)

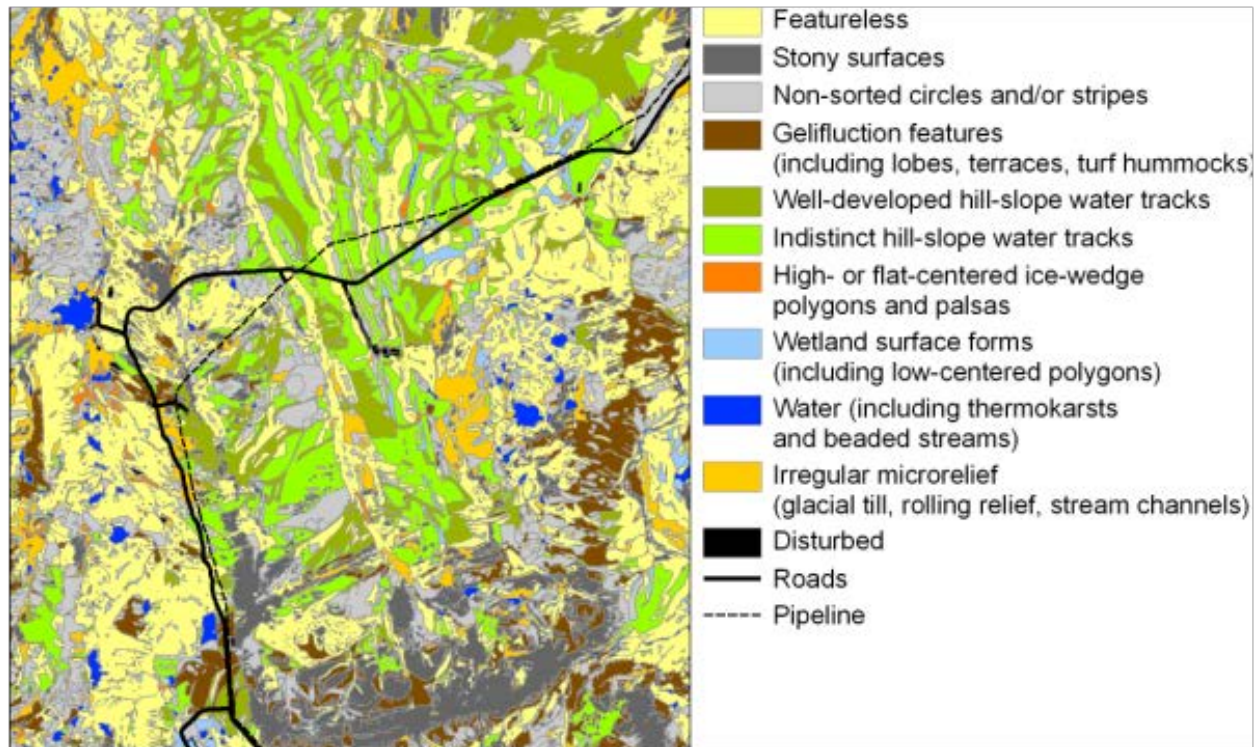


Fig. 3.4. Surface geomorphology of the upper Kuparuk River region (based on Walker and Maier 2008). [INSERT COLOR MAP]

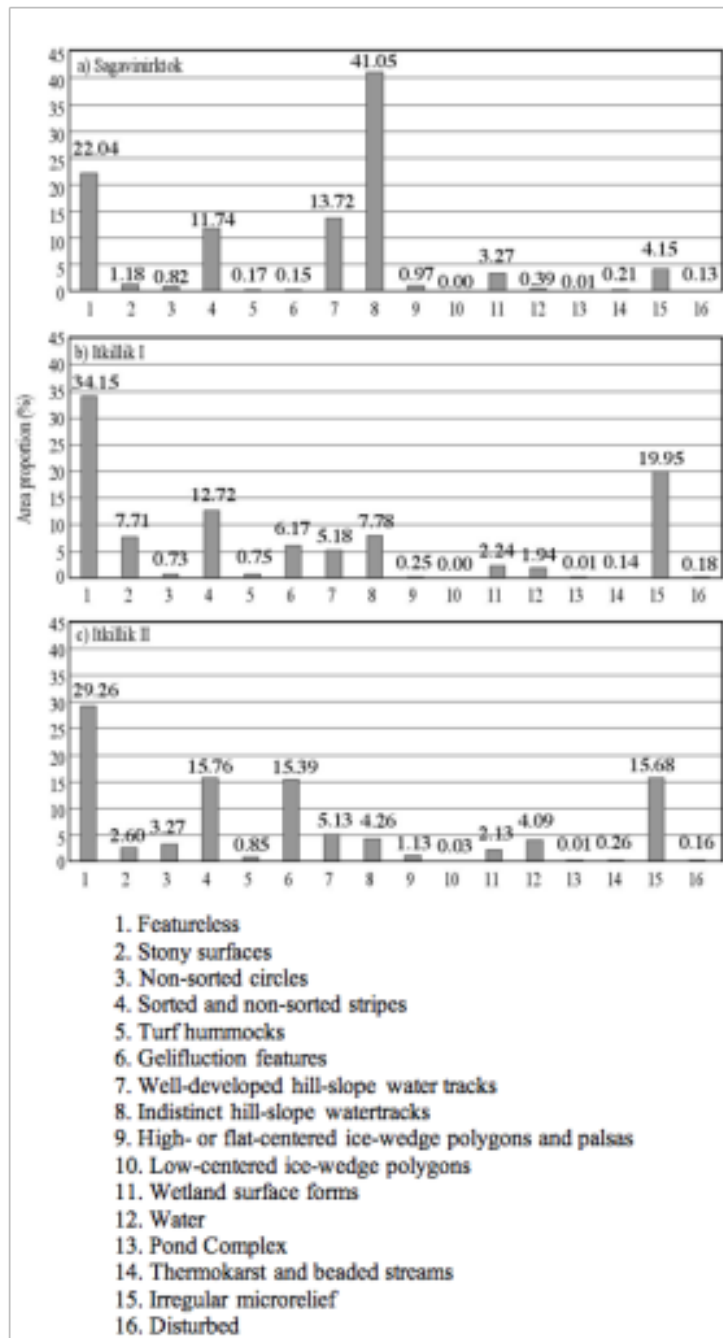


Fig. 3.5. Area analysis of surface geomorphology units (Fig. 3.4) on each glacial surface. (based on Munger et al. 2008). [INSERT COLOR MAP]

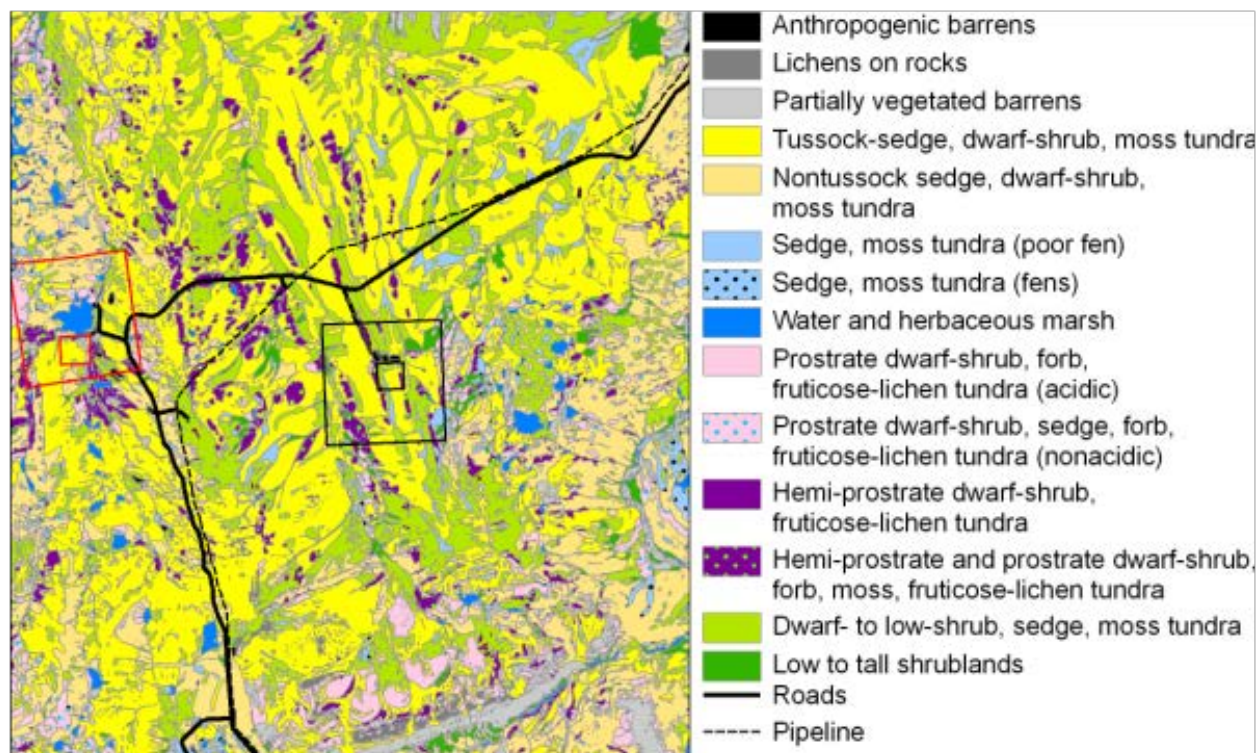


Fig. 3.6. Vegetation of the Upper Kupa-ruk River region. Red rectangles are areas of vegetation maps at Toolik Lake LTER research area (Walker and Maier 2008). Black boxes are areas of maps of research areas at Imnavait Creek (described in Walker and Walker 1996). [INSERT COLOR MAP]

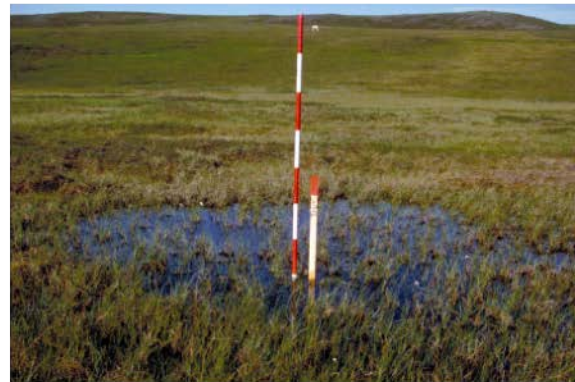
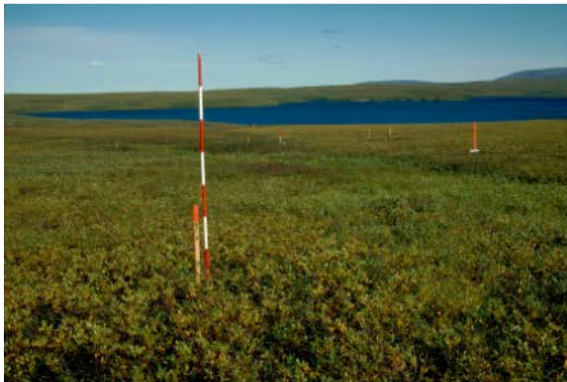
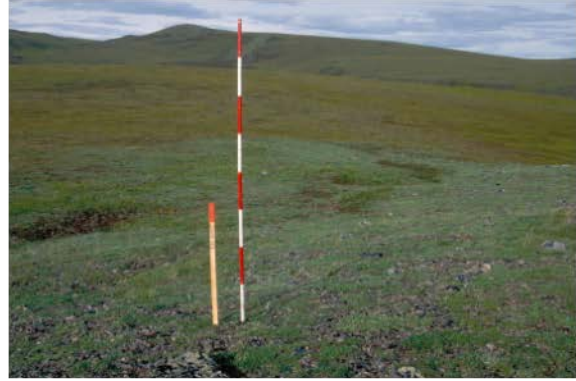


Fig. 3.7. Common plant communities in the Toolik Lake region: Top left - barrens, *Cetraria nigricans*-*Rhizocarpon geographicum* comm. on block field of Itkillik-I-age surface; Top right - dry acidic tundra, *Selaginello sibericae*-*Dryadetum octopetalae* on south-facing Itkillik-II-age kame west side of Toolik Lake; Middle left - snowbed, *Carici microchaetae*-*Cassiopetum tetragonae* on steep north-facing slope of Itkillik-II-age till deposit; Middle right - moist nonacidic tundra, *Dryado integrifoliae*-*Caricetum bigelowii* on Itkillik-II-age hill slope west of Toolik Lake;

Lower left - shrub tundra, *Sphagno-Eriophoretum vaginati betuletosum nanae* in water track margin; and Lower right - wetland, *Carex aquatilis-Carex chordorrhiza* comm. in rich fen complex on Itkillik II surface. Also



see

Fig. 3.3 for photo of tussock tundra (*Sphagno-Eriophoretum vaginati typicum*), the most common and zonal vegetation type in the region. Photos by D. A. Walker.

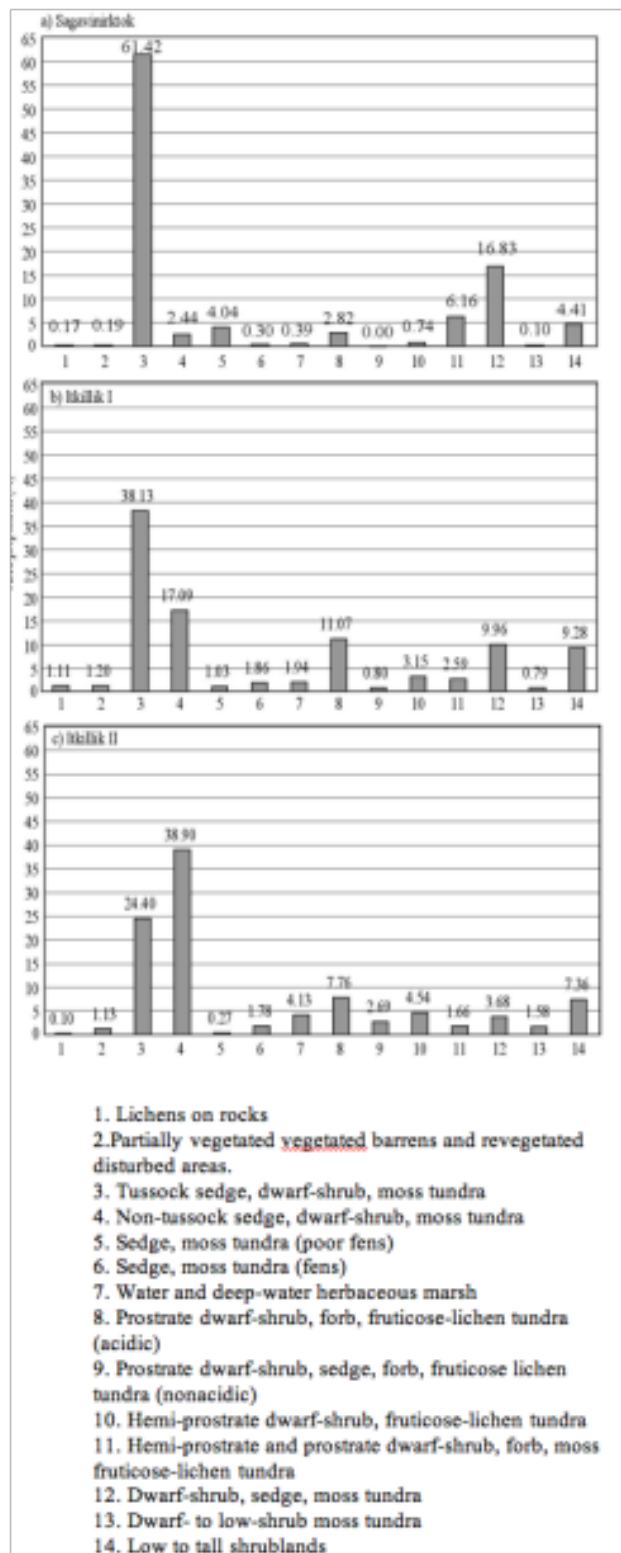


Fig. 3.8. Area analysis of vegetation units (from Fig. 3.7) on the major glacial units (from Munger et al. 2008.)

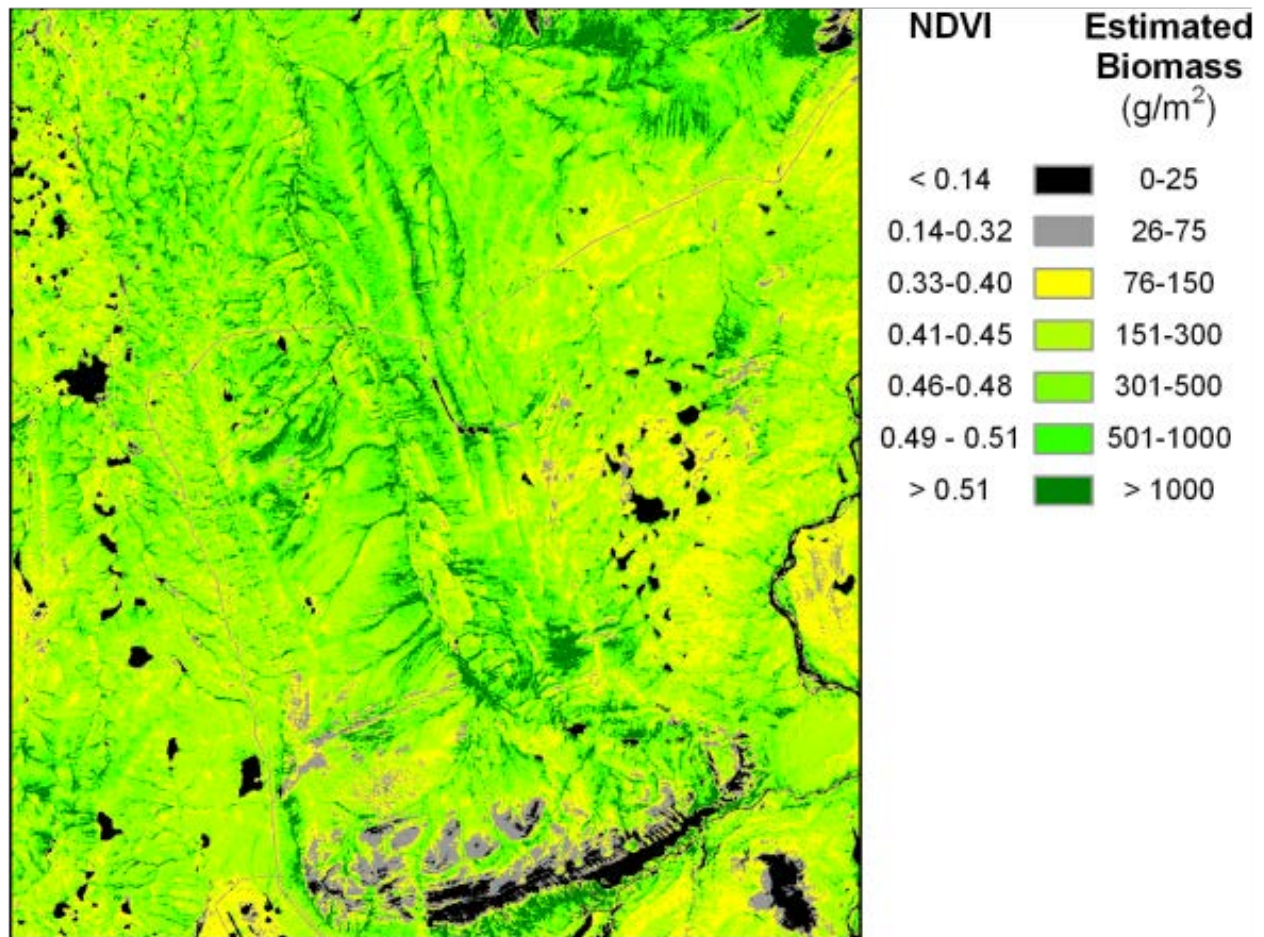


Fig. 3.9. NDVI of the Upper Kupa-ruk River region. The image is from a SPOT-1 multispectral image acquired 29 July 1989. $NDVI = (NIR - R) / (NIR + R)$, where R is the reflectance in the red band (630-690 nm) and the NIR is the reflectance in the near infrared band (760-900 nm). Compare the pattern on the NDVI image with the glacial geology map (Fig. 3.2) and note greater biomass per unit area on the older Sagavanirktok-age surfaces. Based on Shippert et al. (1995). [INSERT COLOR MAP]

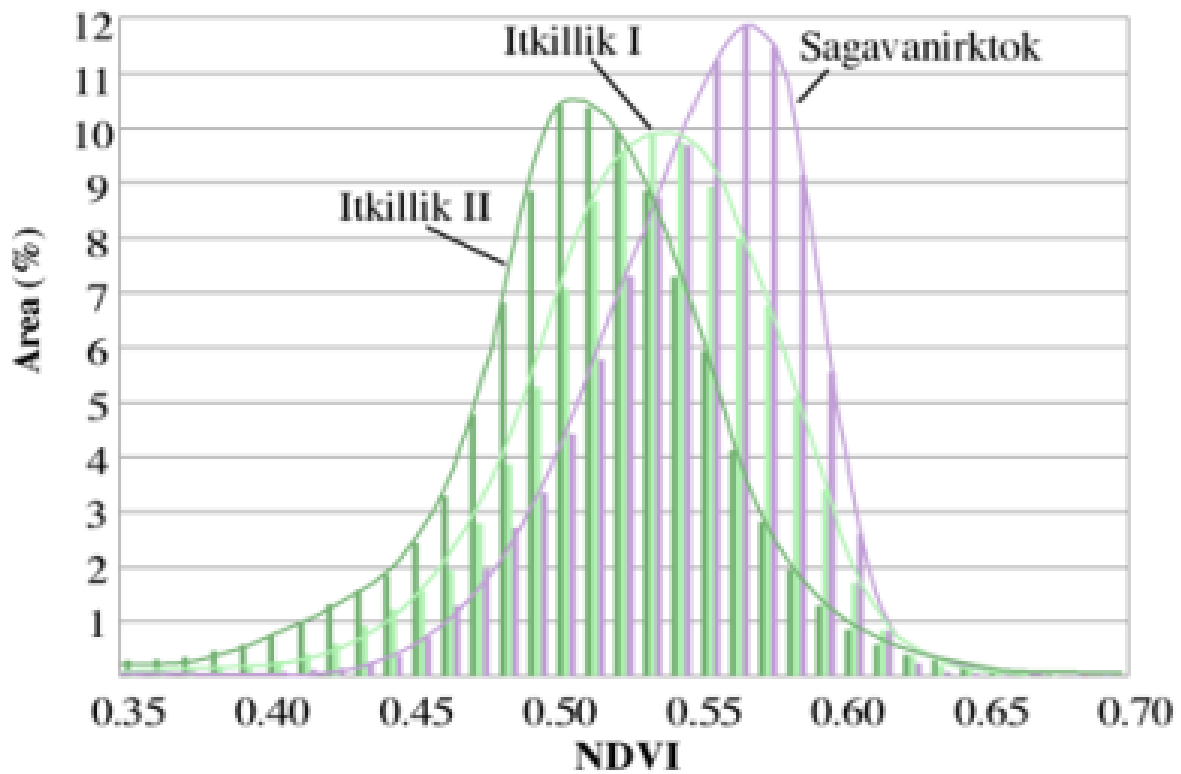


Fig. 3.10. Distribution of NDVI on three glacial units in the Toolik Lake region. Curves represent smoothed data for 45 NDVI classes (based on Munger et al. 2008).

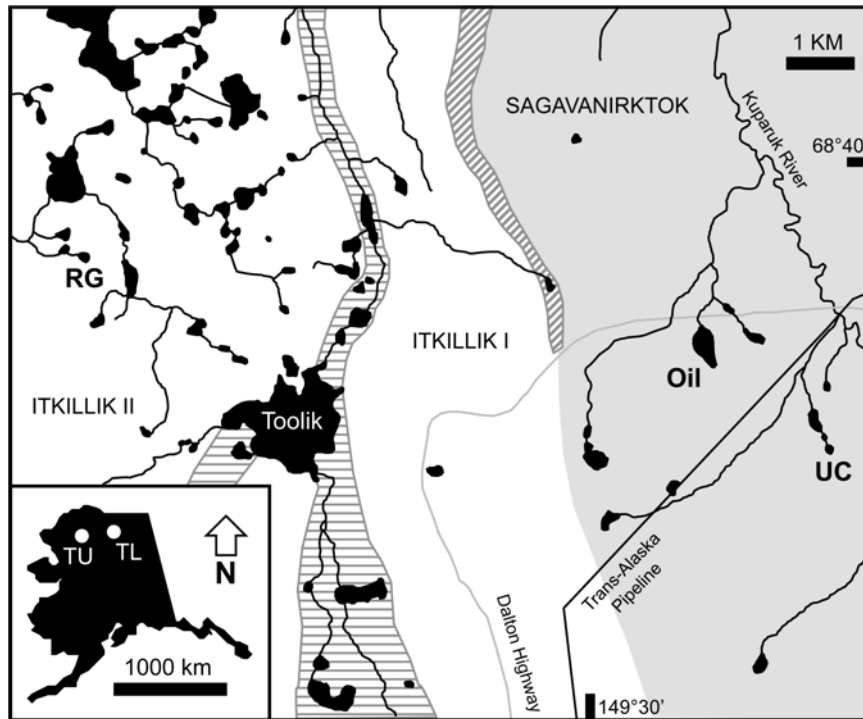


Fig. 4.1. Map of glacial geology and study sites in the Toolik Lake area of the arctic foothills, northern Alaska. The Sagavanirktok glaciated surface is shaded gray, the Itkillik I and II surfaces are white, and areas of Itkillik I and II outwash are indicated by diagonal and horizontal lines, respectively (Walker et al. 1995, Hamilton 2003). Paleoecological study sites include Red Green Lake (Oswald et al. 2003b), Toolik Lake (Bergstrom 1984, Bixby 1992), Oil Lake (Eisner and Colinvaux 1992, Oswald unpublished), and Upper Capsule Lake (Oswald et al. 2003b). The inset map shows the locations of Toolik Lake (TL) and Tukuto Lake (TU; Oswald et al. 1999) in northern Alaska.

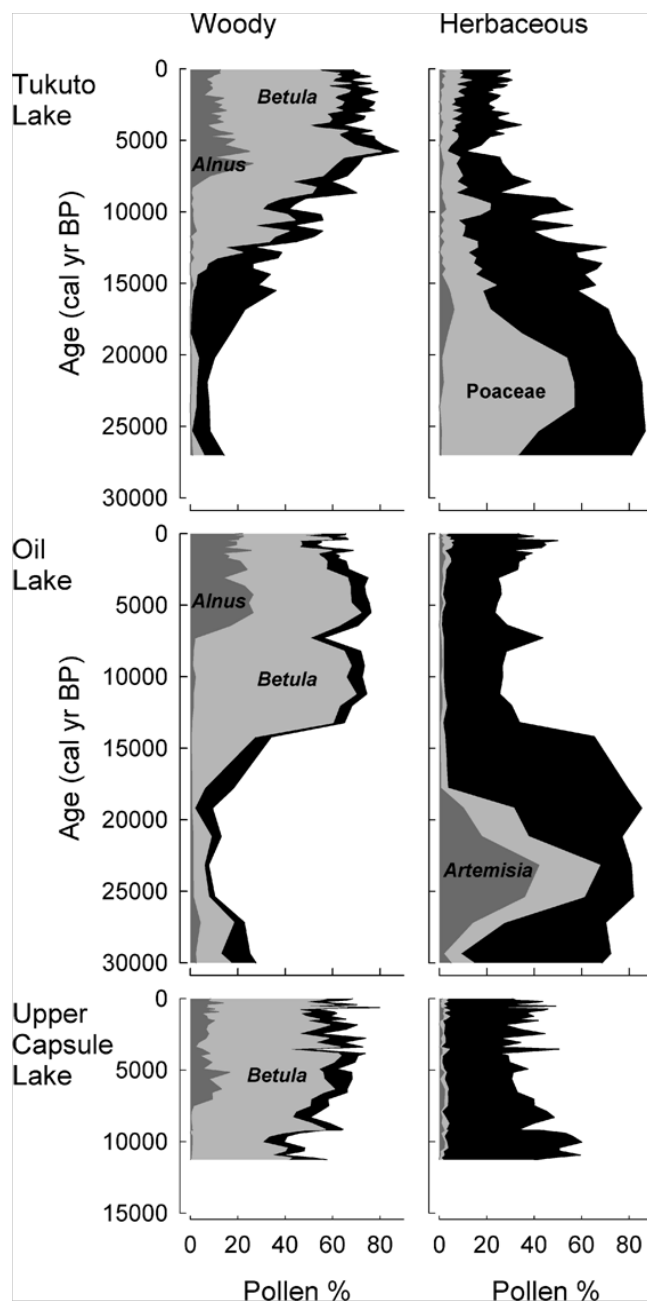


Fig. 4.2. Pollen data from Tukuto Lake (Oswald et al. 1999), Oil Lake (Oswald unpublished), and Upper Capsule Lake (Oswald et al. 2003b). Left-hand graphs show woody taxa; black fill is total woody, light gray is *Betula*, and dark gray is *Alnus*. Right-hand graphs show herbaceous taxa; black fill is total herbaceous, light gray is Poaceae, and dark gray is *Artemisia*.

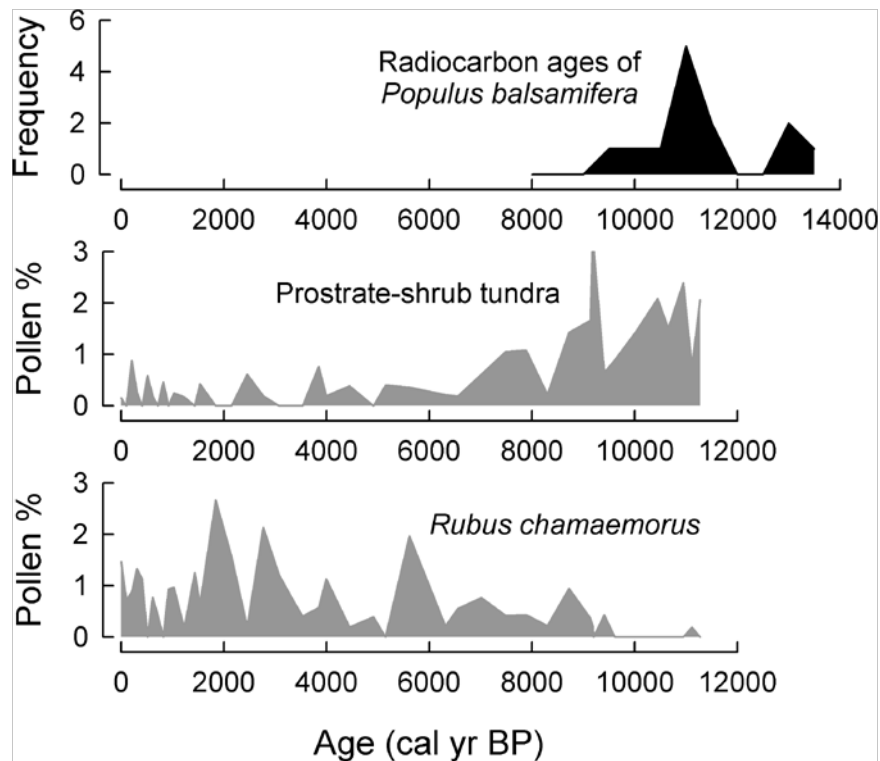


Fig. 4.3. Diagrams showing: ^{14}C dates on *Populus* wood occurring beyond its present-day range limit in arctic Alaska (Hopkins et al. 1981, Mann et al. 2002, Kaufman et al. 2004); Upper Capsule Lake pollen-percentage sum for taxa indicative of prostrate-shrub tundra (Oswald et al. 2003a,b); and Upper Capsule Lake pollen percentages for *Rubus chamaemorus*, an indicator of organic soils and tussock tundra (Oswald et al. 2003a,b).

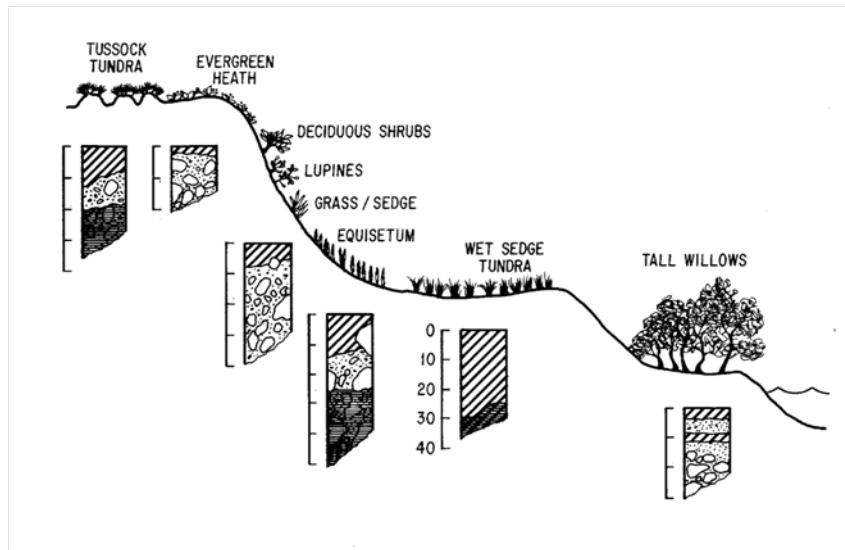


Fig. 5.1. A typical toposequence of tundra vegetation and soils along a series of river terraces above the Sagavanirktok River. The horizontal distance is 50-250 m; vertical distance is 5-7 m. Soil profile depths are in cm. In the soil profiles, hatched areas indicate the upper organic mat with a mix of loess, till, and river gravel below. Dark shading at bottom indicates permafrost; where there is no dark shading the profile does not extend to the bottom of the active (annually thawed) layer (from Giblin et al. 1991).

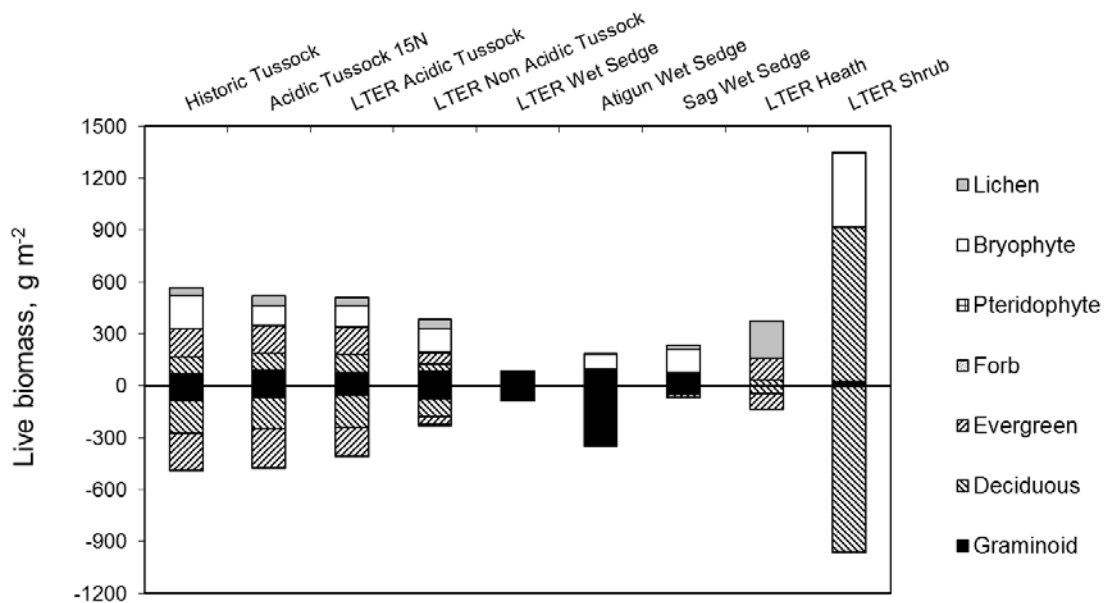


Fig. 5.2. Peak-season (late July-early August) aboveground biomass and belowground stem mass in control plots of tundras near Toolik Lake. The first four sites are acidic and nonacidic tussock tundras; fifth through seventh sites are wet sedge tundras; eighth site is a dry heath, ninth site is a riparian shrub tundra. Aboveground biomass is shown as positive values on the vertical axis; belowground stem mass shown as negative values. Root biomass is not shown. Composition of the vegetation is indicated by separating biomass by plant functional type. Data are averages of harvests in 2 to 4 different years, except for the Atigun wet sedge and LTER shrub sites. Original data in Shaver et al. 1998, 2001, Mack et al. 2004, Shaver and Chapin 1991, McKane et al. 1995, Gough et al. 1996, 2002, and Hobbie et al. 2005.

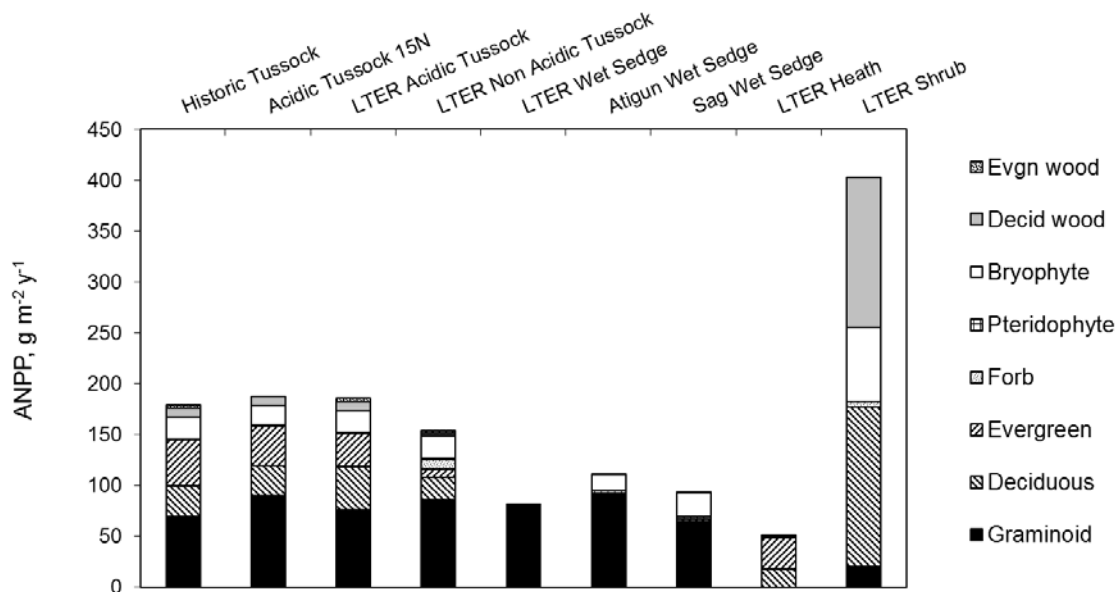


Fig. 5.3. Aboveground Net Primary Production at the same sites as Fig. 5.2, determined from peak-season (late July-early August) harvests. The apical growth component of production was determined directly by separation of new leaves, twigs, and inflorescences in the harvests. Bryophyte production and wood production components were estimated by assuming constant percentage growth rates for bryophyte biomass and for evergreen and deciduous woody stems (Chapin et al. 1995). Lichen production was not measured or estimated at any site.

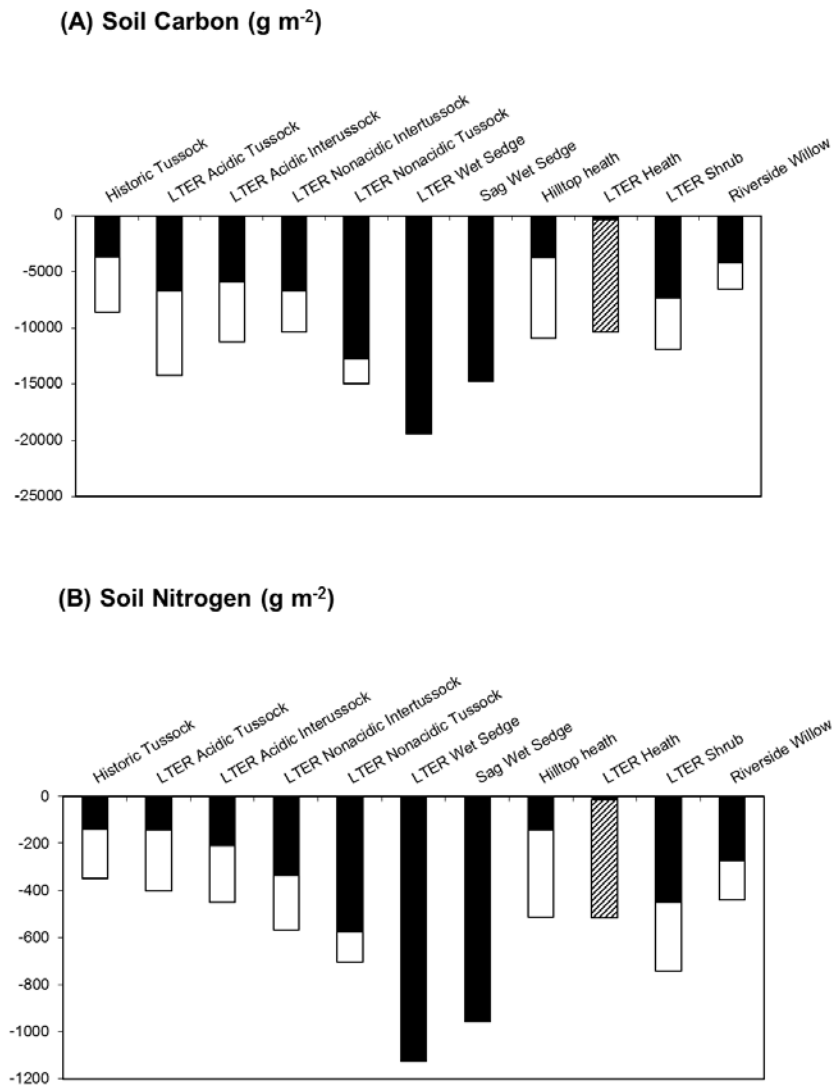
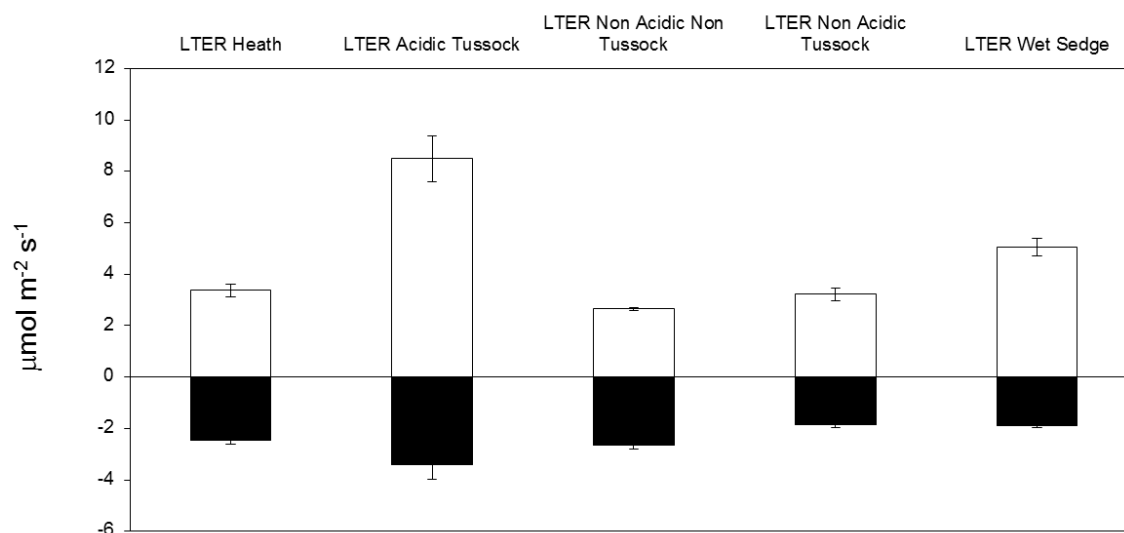


Fig. 5.4. Soil C stocks (top) and N stocks (bottom) in tussock, wet sedge, heath, and shrub tundras. Shown are the total amounts of C and N within the seasonally-thawed, “active layer”. The upper (black) segment indicates amounts within the organic horizon, and the lower (clear) segment indicates amounts within the mineral soil. Where there is no clear segment the soil did not thaw beneath the organic mat. In the “LTER Heath” site the depth of thaw is unknown so the C and N stocks in the upper 50 cm of soil are estimated (hatched segment). Inclusion of C and N stocks frozen within the upper meter of permafrost would increase the total stocks by at least 100% (Ping et al. 1997, 2008).

(A) GPP and R_E



(B) NEE

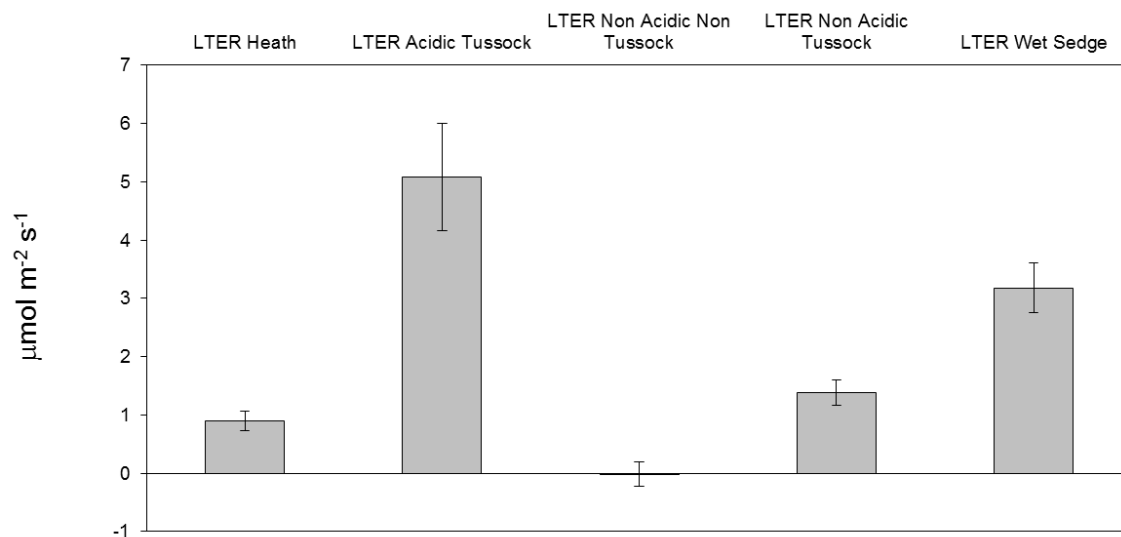


Fig. 5.5. Mid-season summer values for (A) GPP (open) and R_E (closed), and (B) NEE (same as NEE) at core LTER sites. GPP and NEE are predicted values at $600 \mu\text{mol m}^{-2} \text{s}^{-1}$ PPFD (Photosynthetically active Photon Flux Density), from light response curves in Street et al. (2007).

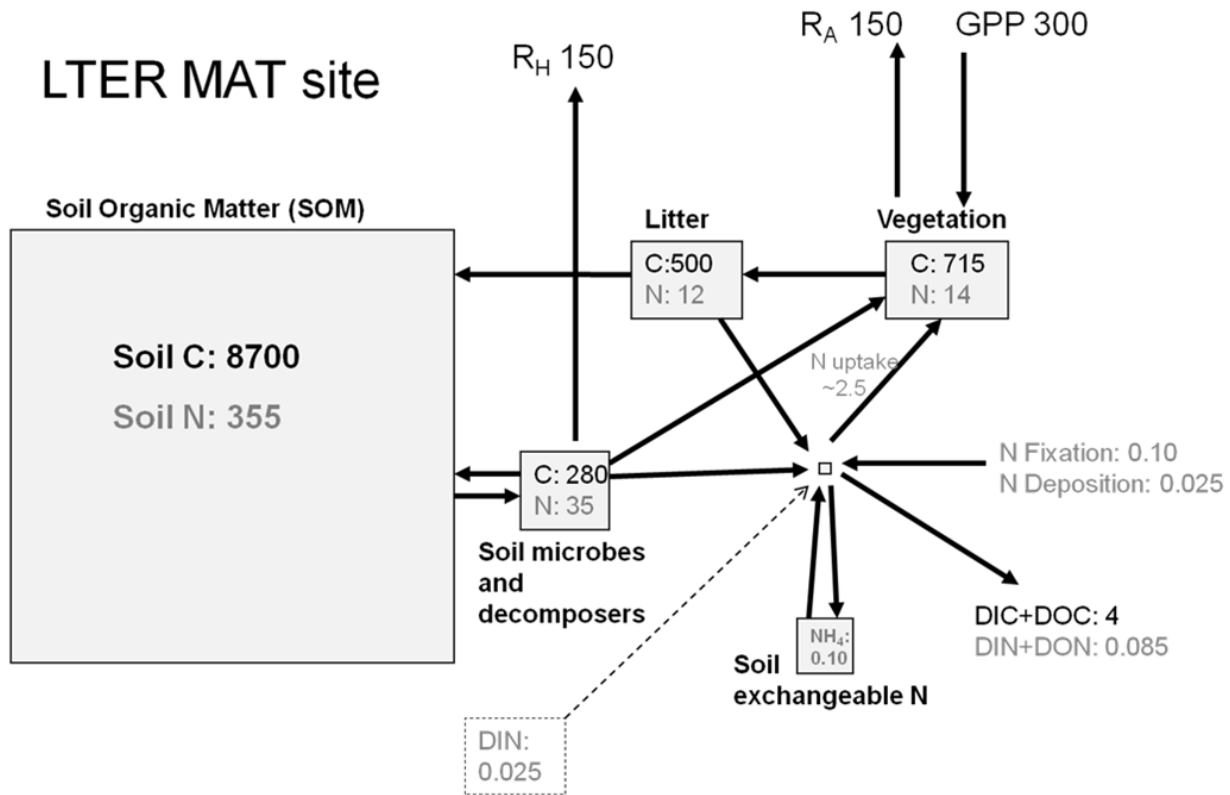


Fig. 5.6. Summary of C (black) and N (grey) budgets in Moist Acidic Tundra at Toolik Lake. Pool sizes (boxes) in g m⁻²; fluxes (arrows) in g m⁻² yr⁻¹; the dashed box and arrow indicate the DIN pool size (very small). Values are estimates, chosen for consistency among the numerous individual studies described in this chapter.

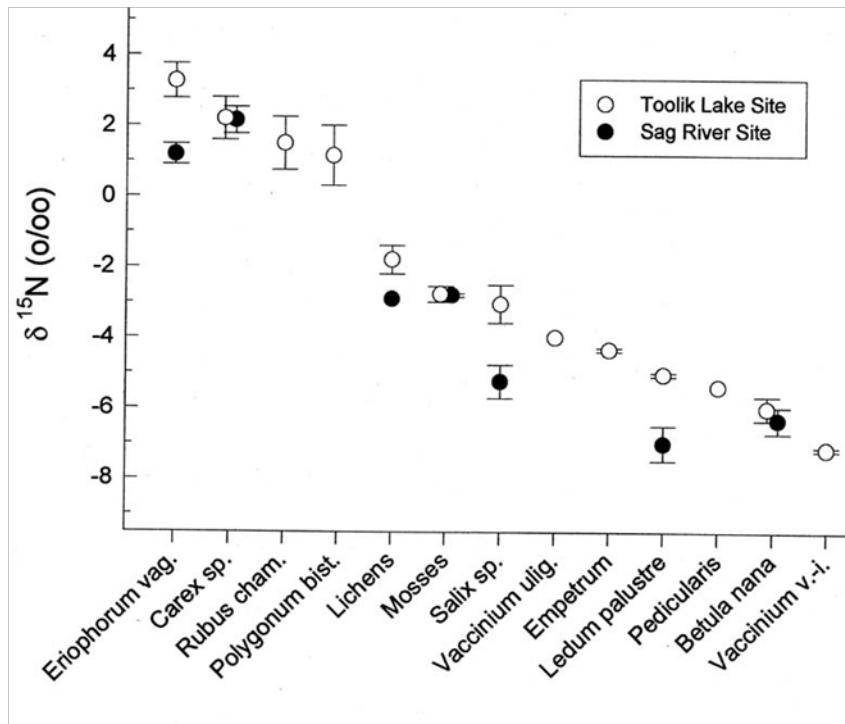
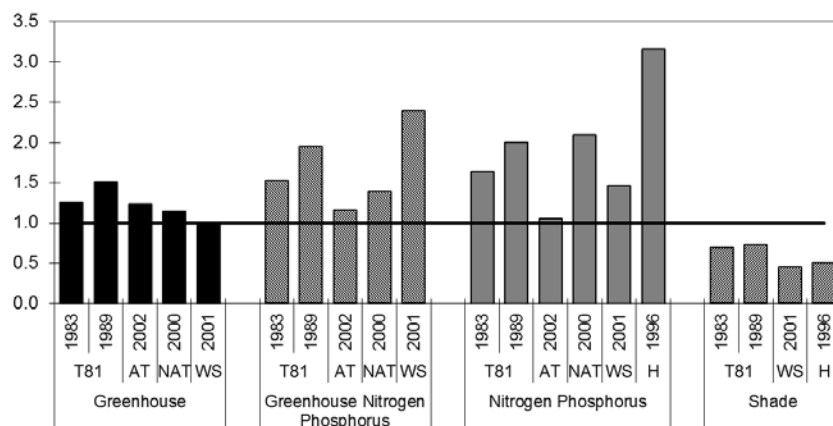


Fig. 5.7. Natural abundance N isotope ratios of leaves of common species of moist acidic tundra (from Nadelhoffer et al. 1996). Leftmost species are graminoids, Rightmost species are mostly woody evergreen Ericaceae or deciduous shrubs.

(A) New Aboveground Vascular, Treatment:Control



(B) Total Aboveground Vascular, Treatment:Control

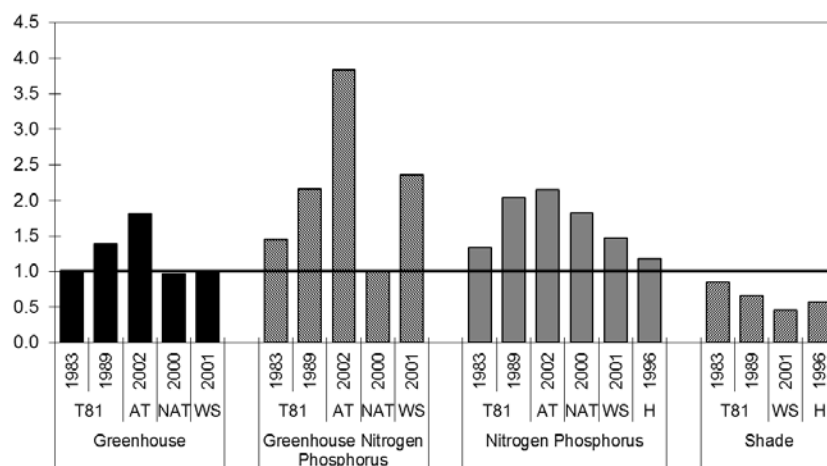


Fig. 5.8. Response index (treatment value:control value) of (A) New aboveground vascular plant growth and (B) Total aboveground vascular biomass in greenhouse, fertilizer, and shade treatments in acidic and nonacidic tussock, wet sedge, and heath tundras. (N.B.: results of 1994 harvest of LTER wet sedge tundra not shown due to anomalously low production and biomass in control plots, leading to anomalously high response indices in all treatments in 1994.) The horizontal axis indicates treatment (Greenhouse, Greenhouse Nitrogen Phosphorus, Nitrogen Phosphorus, or Shade), Site (T81 = 1981 Historic Tussock, AT = LTER Acidic Tussock, NAT = LTER Nonacidic Tussock, WS = LTER Wet Sedge, H = LTER Heath), and year of sampling.

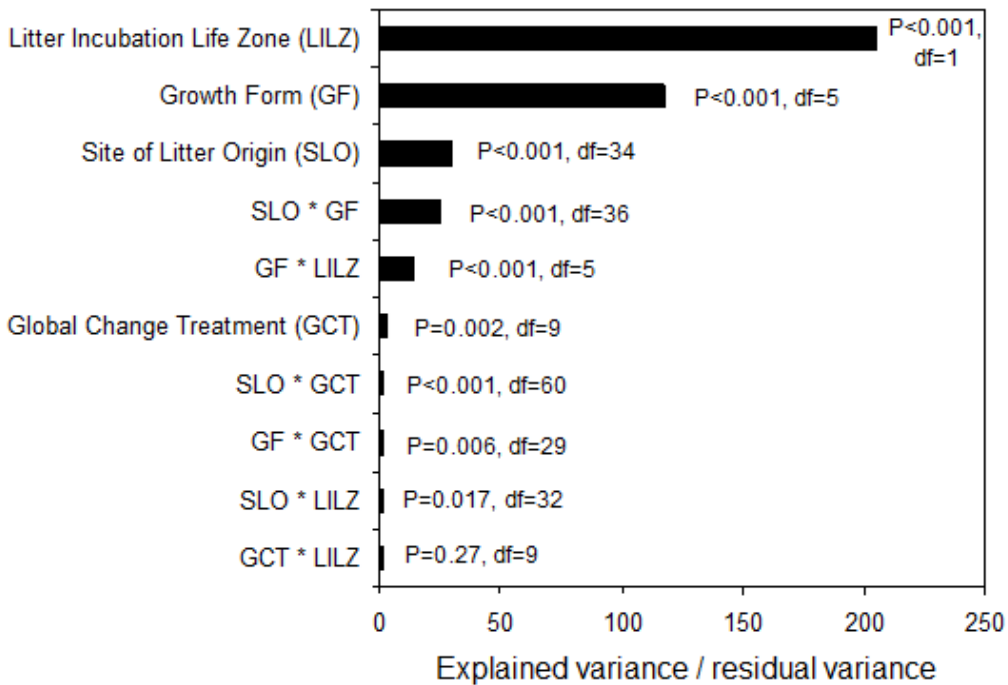


Fig. 5.9. Results of a 4-way analysis of variance unraveling the key biotic and abiotic effects on % mass loss of leaf litters, based on the predominant plant species in 33 experiments in arctic and alpine sites in the Northern Hemisphere (see Fig. 1). Mass loss % data were arcsine(square-root(100/x)) transformed prior to analysis. Total df = 1824 (from Cornellisen et al. 2007.)

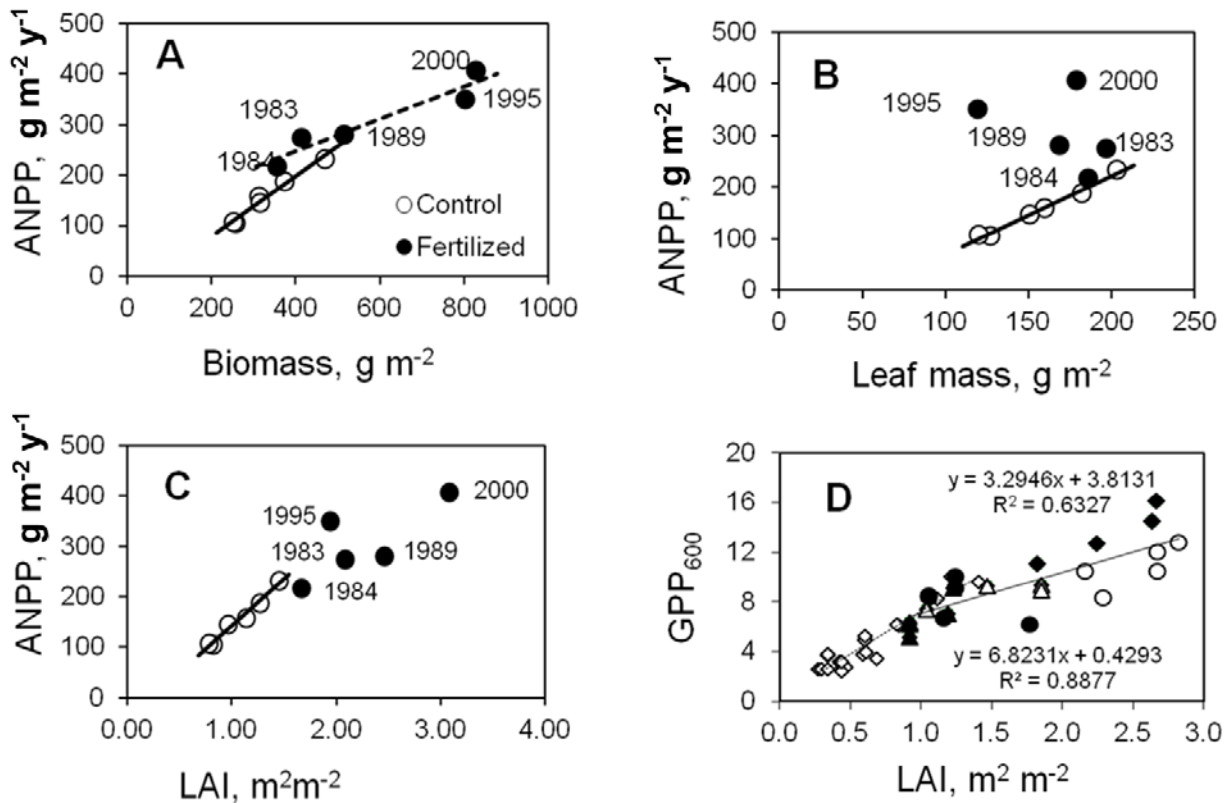


Fig. 5.10. Gross primary production (GPP) and aboveground net primary production (ANPP) are closely correlated with leaf area even as species composition changes among years or with fertilizer addition. Data in panels A, B, C from control and fertilized moist tussock tundra at Toolik Lake. Data in panel D from control and fertilized plots in 5 different tundras at Toolik Lake. In Panel D, GPP_{600} is GPP at $600 \mu\text{mol m}^{-2} \text{s}^{-1}$ photosynthetically active photon flux. Open and filled symbols represent data from control and fertilized plots, respectively. Circles = LTER acidic tussock tundra, diamonds = nonacidic nontussock tundra, triangles = heath tundra. Original data in Chapin et al. 1995, Shaver et al. 2001, and Mack et al 2004.

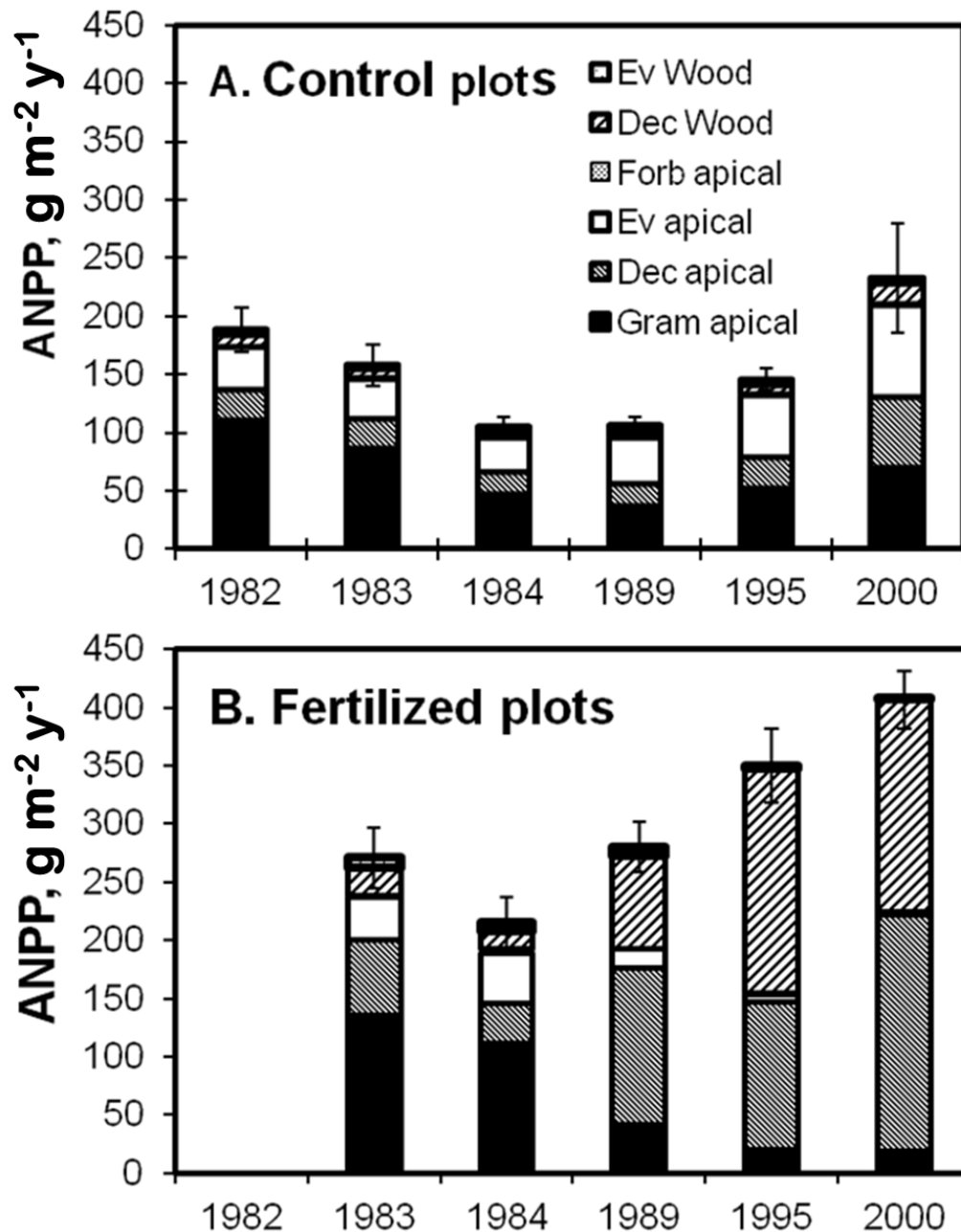


Fig. 5.11. (A) Aboveground net primary production (ANPP) in unfertilized control plots of moist acidic tundra at Toolik Lake, Alaska, over six harvests between 1982 and 2000. Although the 2000 harvest occurred after 20 years of climate warming, we cannot say for sure whether the greater total ANPP and the greater productivity of deciduous shrubs in 2000 is the result of warming or is within the “normal” range of ANPP. (B) ANPP in fertilized plots at the same site,

where fertilizer addition (N+P) began in 1981. The initial fertilizer response was dominated by graminoids, with a long-term dominance by deciduous shrubs and a large increase in wood production apparent only after 1989. Ev wood = wood production in evergreen shrubs; Dec wood = wood production in deciduous shrubs; Ev apical = leaf and twig production in evergreens; Dec apical = leaf and twig production in deciduous shrubs; Gram apical = leaf and culm production by grasses and sedges. Details are published in Chapin et al. (1995), Shaver et al. (2001), and Mack et al. (2004).

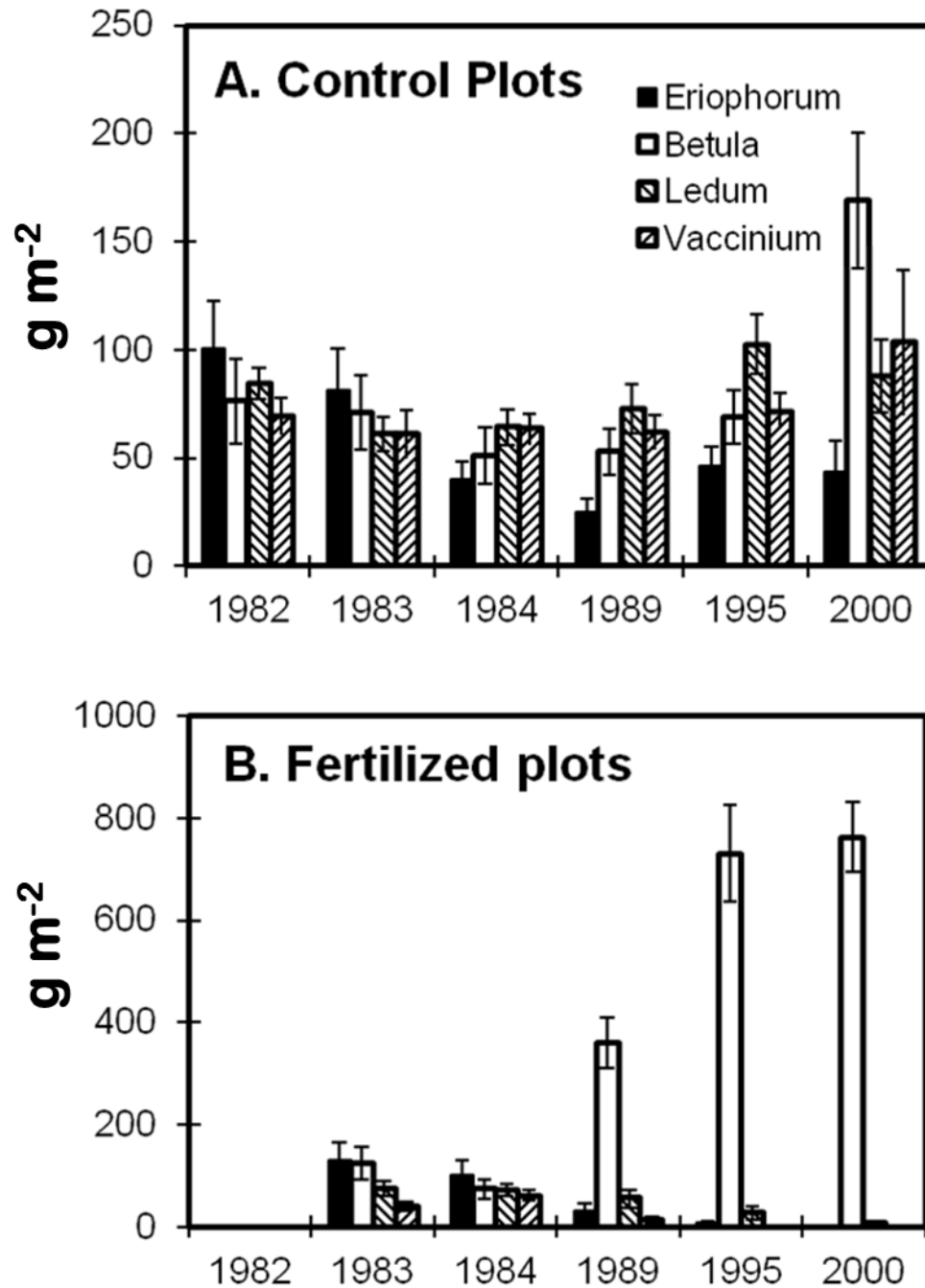


Fig. 5.12. Biomass of the four most abundant species in moist acidic tundra at Toolik Lake, in (A) control and (B) fertilized plots. Here biomass includes aboveground biomass and belowground stems but not roots. Original data in Chapin et al. (1995), Shaver et al. (2001), and Mack et al. (2004).

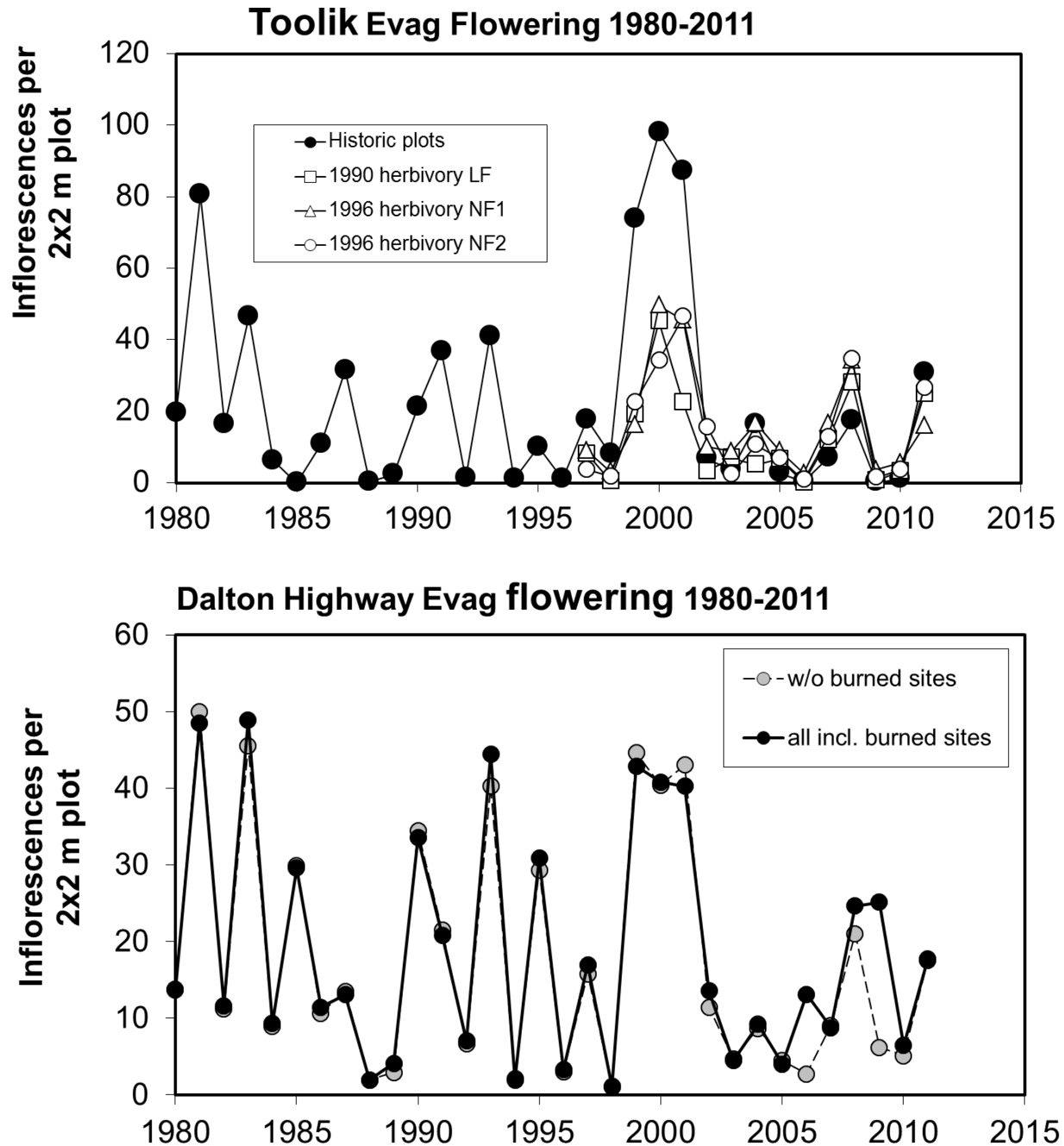


Fig. 5.13. Mean number of inflorescences of *Eriophorum vaginatum* in 2x2 meter plots at Toolik Lake (top) and in similar plots along the Dalton Highway (bottom; in most years n = 21-23 sites, 1979-2011). In the upper panel, different symbols represent different sets of control plots in moist acidic tundra. In the lower panel, black symbols include all data while grey symbols are means not including 3 sites that were

burned in 2004-2005. Data for 1979-1982 were published in Shaver et al. (1986). In the upper panel, different symbols represent different sets of control plots in moist acidic tundra. In the lower panel, black symbols include all data while grey symbols are means not including 3 sites that were burned in 2004-2005. Data for 1979-1982 were published in Shaver et al. (1986).

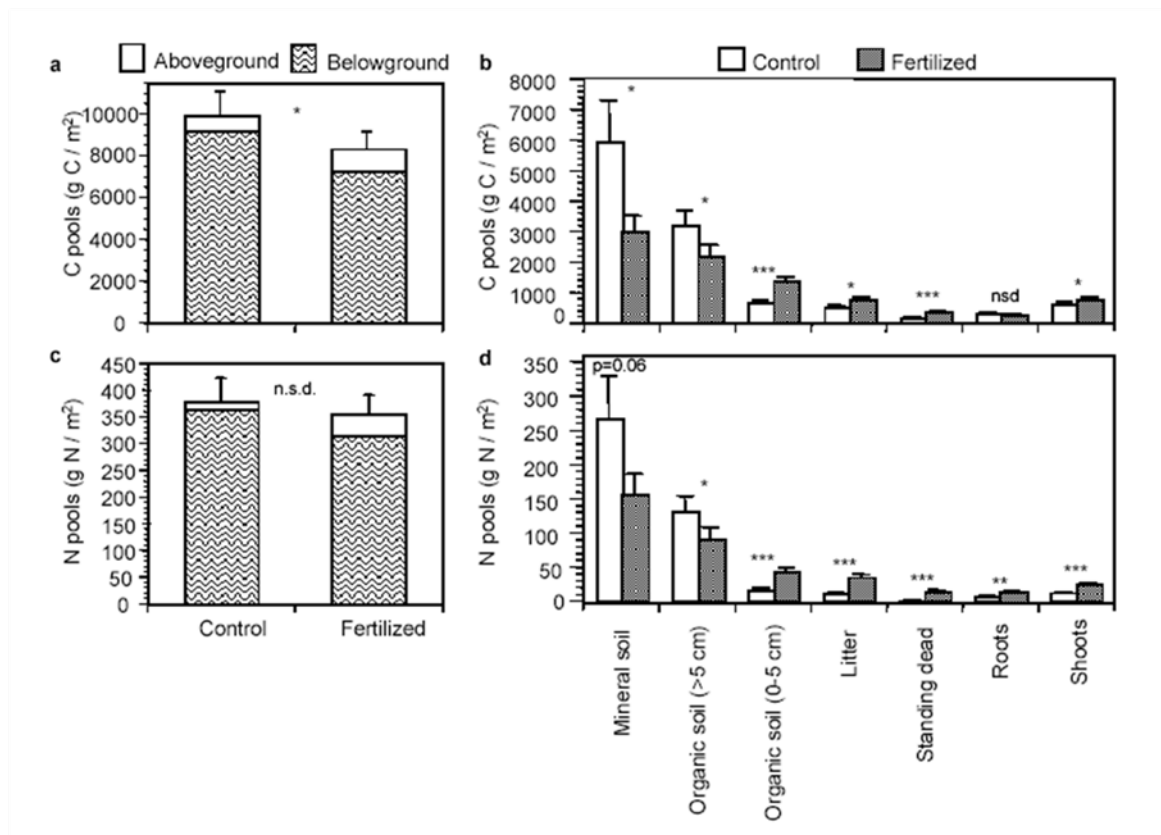


Fig. 5.14. Effects of fertilizer on tundra carbon and nitrogen pools after 20 years of fertilization. Mean (± 1 standard error) above- and belowground carbon (A) and nitrogen (C) pools in unmanipulated control and fertilized treatments of moist acidic tundra near Toolik Lake, Alaska. Aboveground pools include shoots, standing dead plant material, and rhizomes. Belowground pools include surface litter, roots, and organic and mineral soil. Mean (± 1 standard error) carbon (B) and nitrogen (D) pools in plant and soil compartments (from Mack et al. 2004).

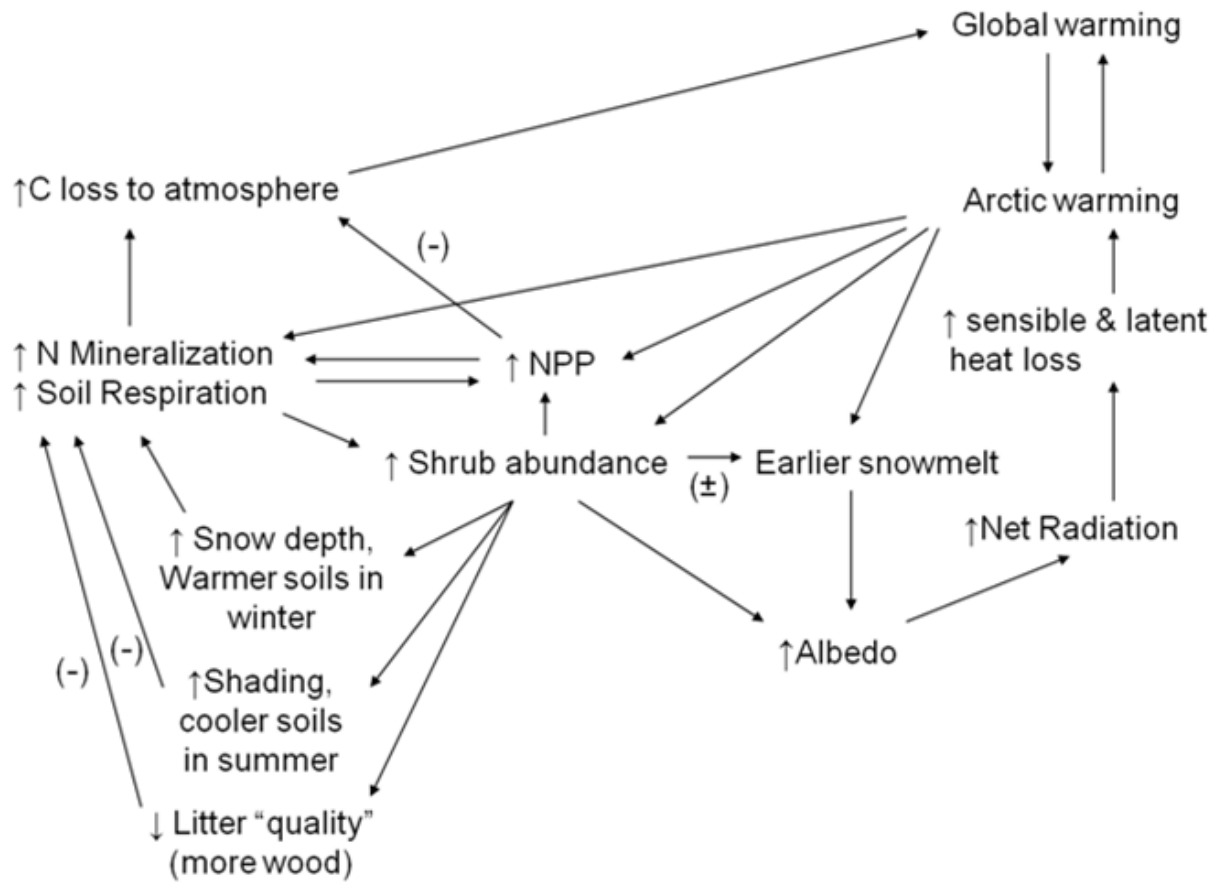


Fig. 5.15. Feedbacks on drivers of change, as explained in text.

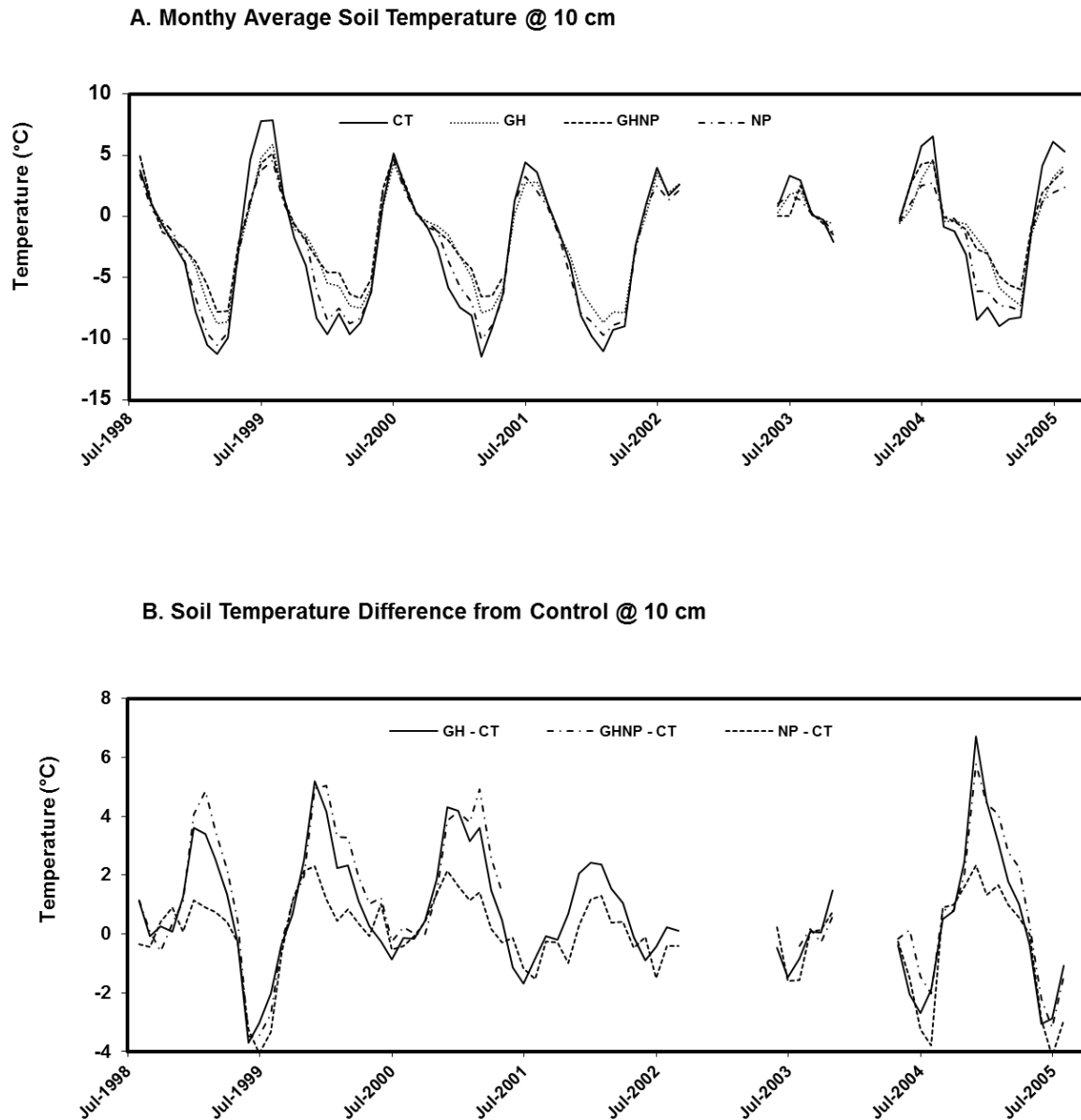


Fig. 5.16. Soil temperatures beneath shrub-dominated experimental plots are warmer in winter and colder in summer than in controls. (A) Monthly average soil temperature at 10 cm depth in LTER experimental plots in Moist Acidic Tundra (MAT) at Toolik Lake, 1993-2005. (B) Difference from control (Treatment – Control) in monthly average soil temperature at the same plots. CT = control plots; GH = greenhouse

plots; NP = N+P fertilized plots; GHNP = greenhouse plus fertilizer plots.
Source: Arctic LTER data base.

Chapter 5 Vignette Figure Legends

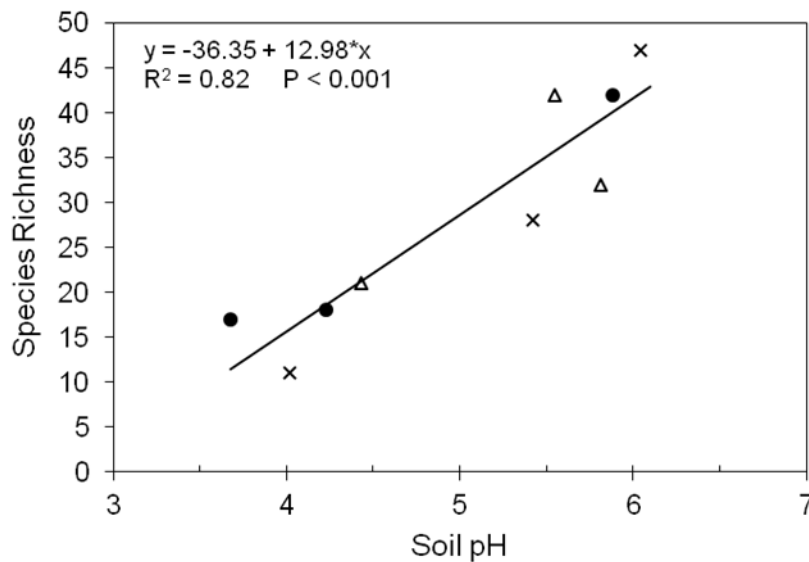


Fig. 5.V1. Relationship between soil pH and vascular plant species richness for snowbed (triangle), watertrack (x) and tussock tundra (circles); from Gough et al. (2000).

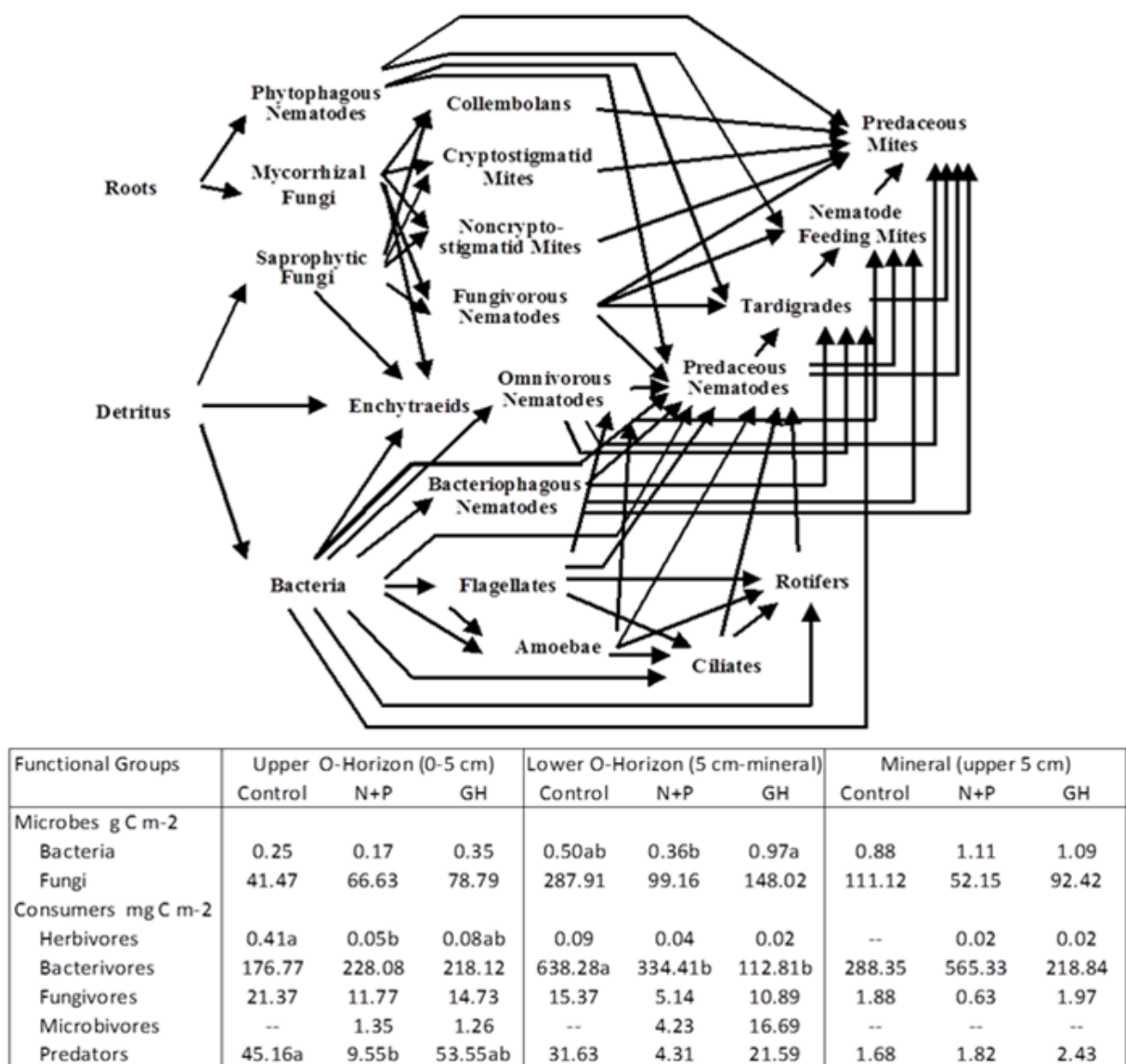


Fig. 5.V2. The belowground food web of the moist acidic tussock (MAT) tundra with biomass estimates of functional groups for three soil horizons from control, N+P, and Greenhouse treatments. Sampling occurred during the summer of 2008. N+P treatments and GH treatments were initiated in 1996 and 1989, respectively. Fungi = saprophytic fungi + mycorrhizal fungi; Herbivores = phytophagous nematodes; Fungivores = collembolans, cryptostigmatid mites, non-cryptostigmatid mites, fungivorous nematodes; Bacterivores = bacteriophagous nematodes + flagellates + amoebae + ciliates + rotifers; Microbivores = enchytraeids; Predators = omnivorous nematodes +

predaceous nematodes + tardigrades + nematode feeding mites + predaceous mites. Letters that differ indicate significant differences among treatments within soil horizon.

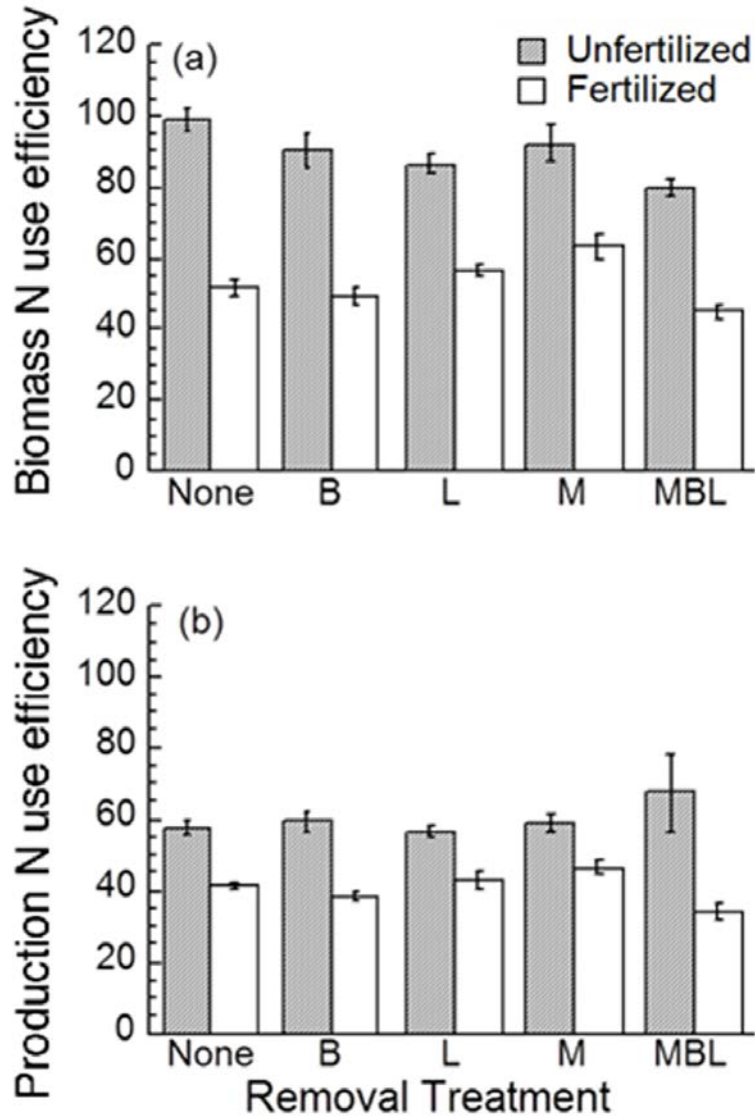


Fig. 5.V3. Ecosystem N use efficiencies of (A) total plant biomass and (B) vascular production after six years of removal and fertilization. Removal treatments were as follows: None = no removal (controls), B = removal of *Betula nana*, L = removal of *Ledum palustre*, M = removal of all mosses, MBL = combined removal of mosses, *B. nana*, and *L. palustre*.

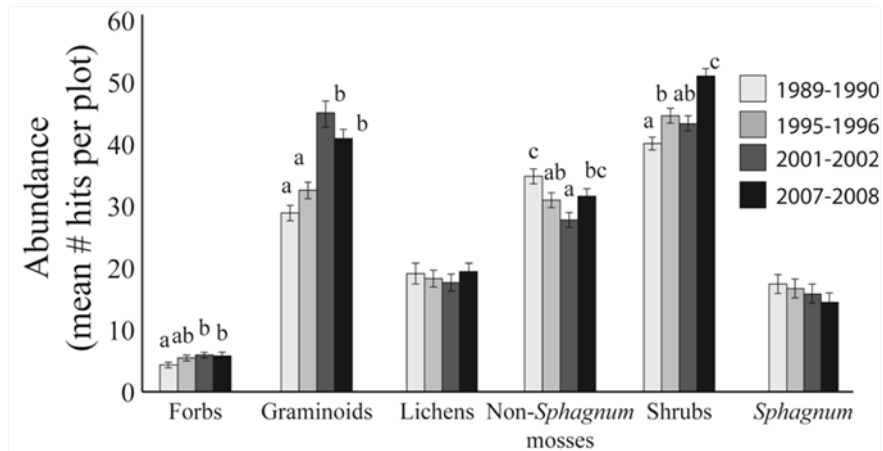


Fig. 5.V4. The mean number of total hits per plot of different vegetation growth forms located at the Imnavait Creek and Toolik grids from 1989-1990 to 2007-2008 (letters above the bars indicate significant differences, error bars represent standard errors).

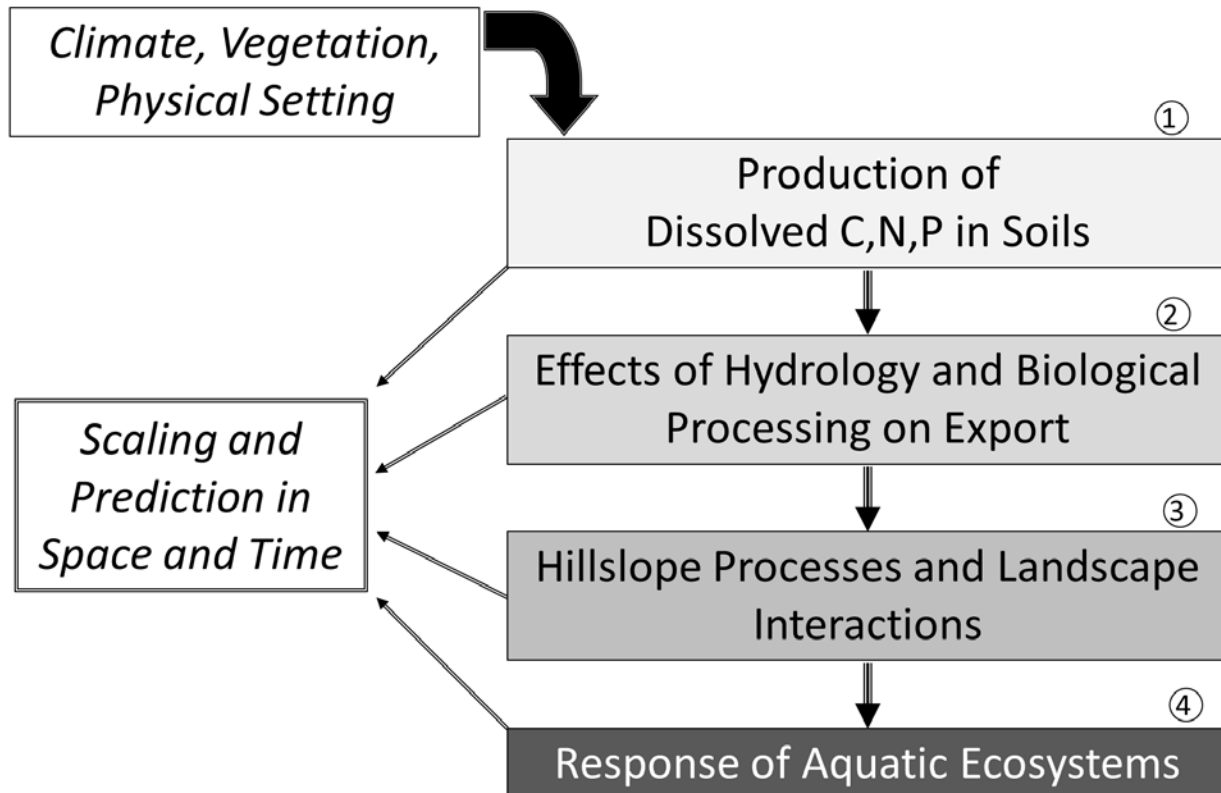


Fig. 6.1. Conceptual model for organizing the Arctic LTER land-water interactions research. Each of the numbered boxes on the right represents major research efforts.

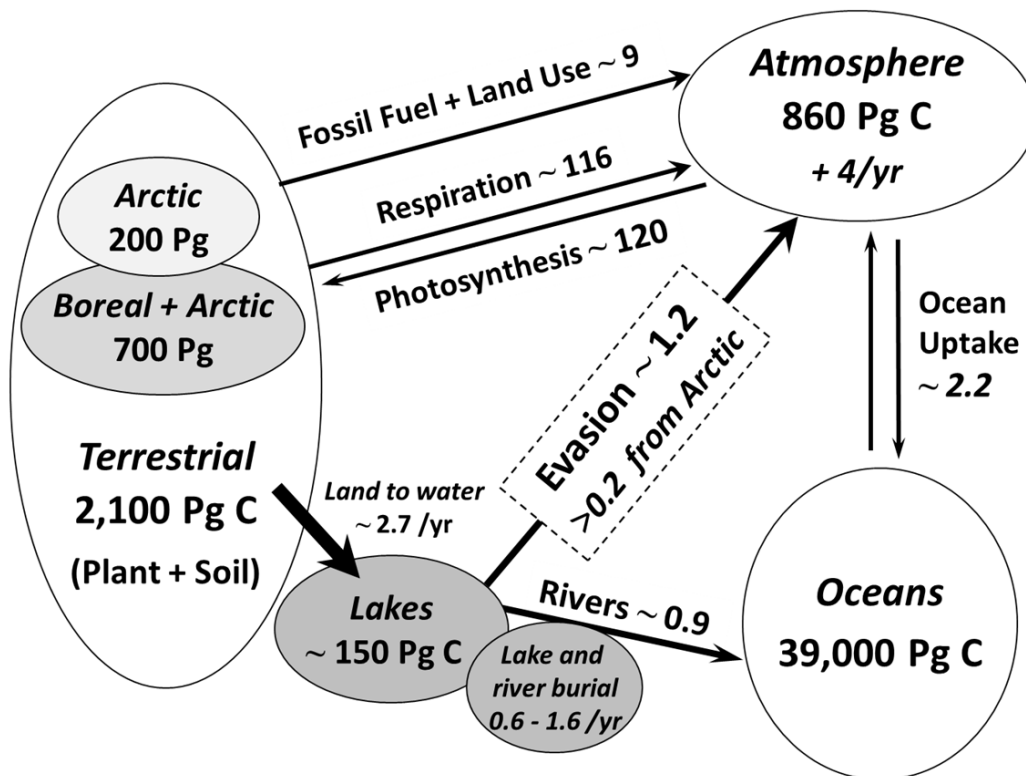
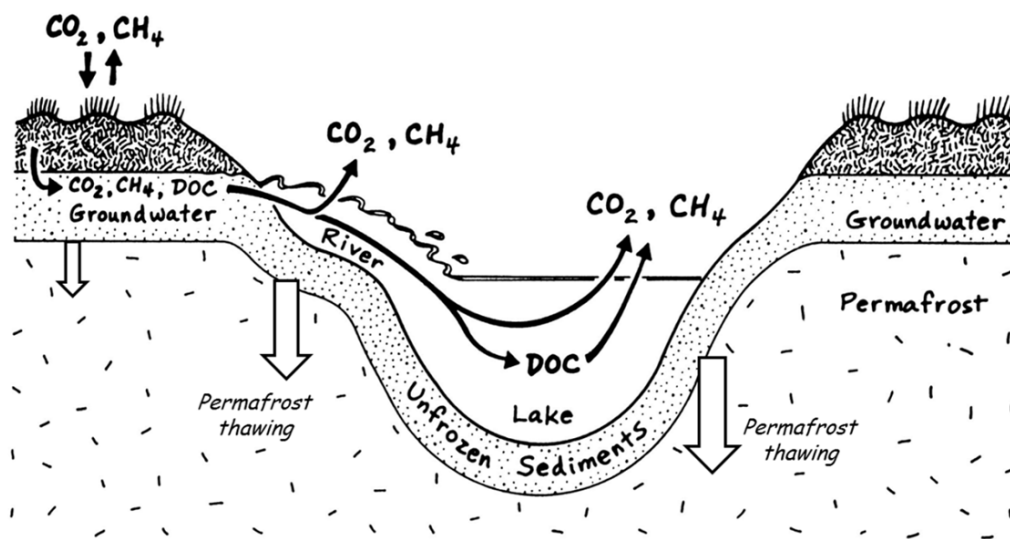


Fig. 6.2. Schematic showing land-water transfer paths of C gases and how hydrological flowpaths may deepen with future permafrost thawing (large arrows in soil), especially beneath streams and lakes (Top). The importance of these water to atmosphere gas transfers in the global C

cycle (Bottom) (data from Kling et al. 1991, 1992; Kling 1995; Canadell et al. 2007; Battin et al. 2009; Aufdenkampe et al. 2011).

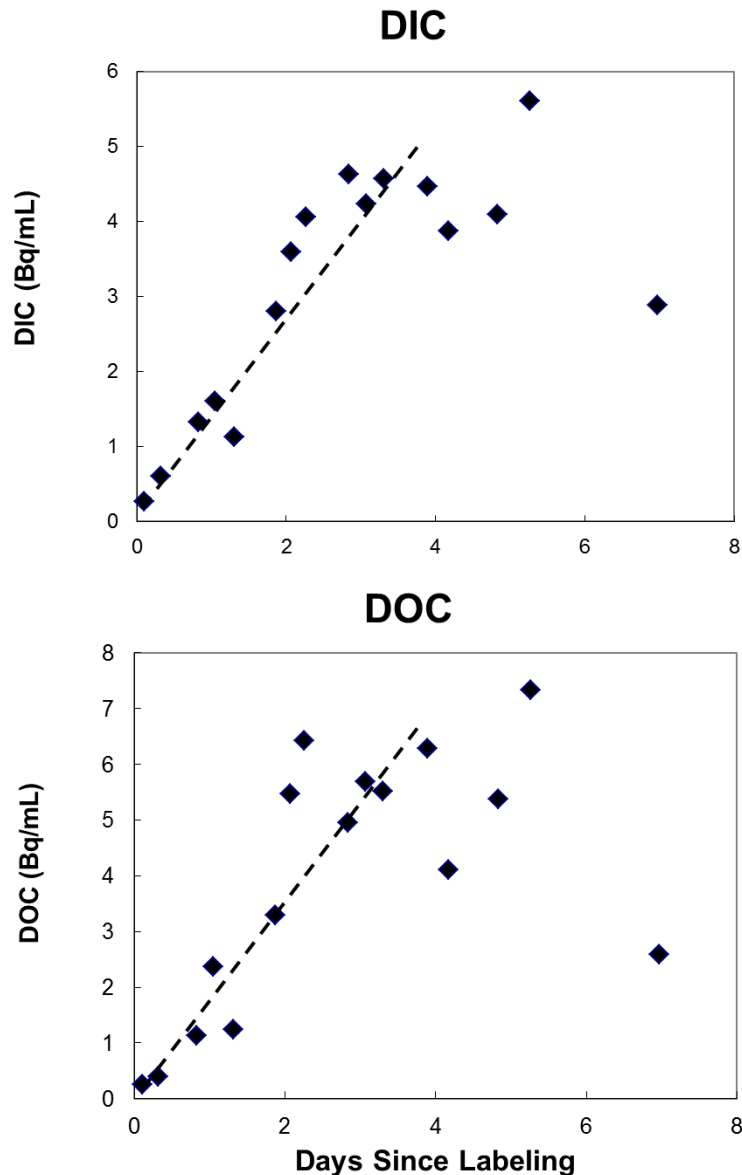


Fig. 6.3. Activity of ^{14}C in dissolved inorganic C (DIC) and dissolved organic C (DOC) in soil waters of tussock tundra vegetation versus days since labeling plants with $^{14}\text{CO}_2$. Dashed line represents the production rate of ^{14}C compounds originating in roots and released into the soil waters (data from LTER; G. Kling, K. Nadelhoffer, M. Sommerkorn, K. Judd (unpublished)).

Landscape Diversity and Microbial Dynamics

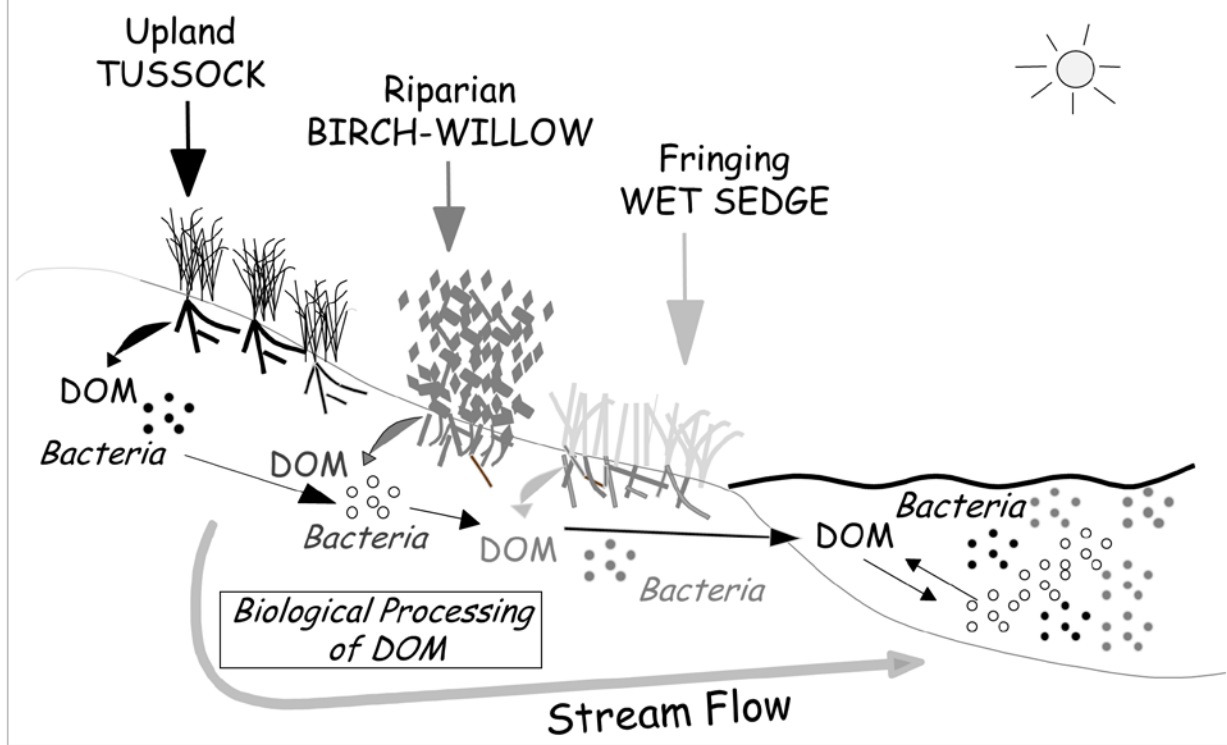


Fig. 6.4. Conceptual model of landscape and microbial diversity showing fidelity of DOM character and soil bacterial communities to overlying vegetation, and mixing of DOM and bacteria moving down the landscape and into receiving waterbodies.

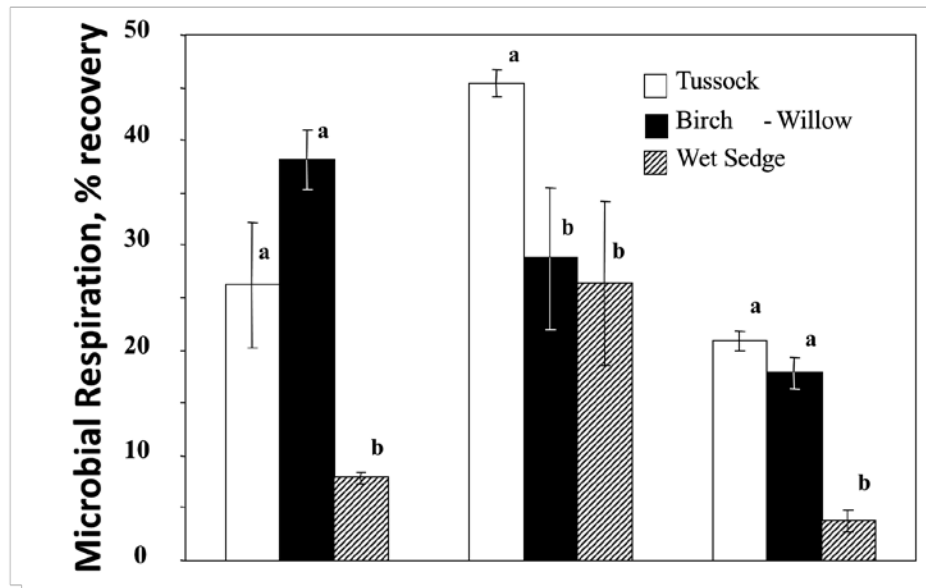


Fig. 6.5. Total C processing of ^{13}C -labelled compounds representing cellulose, chitin, and lignin in soils as represented by microbial respiration. Processing rates varied by compound (not shown) and by the location on the landscape (vegetation communities). With permission from Zak and Kling (2006).

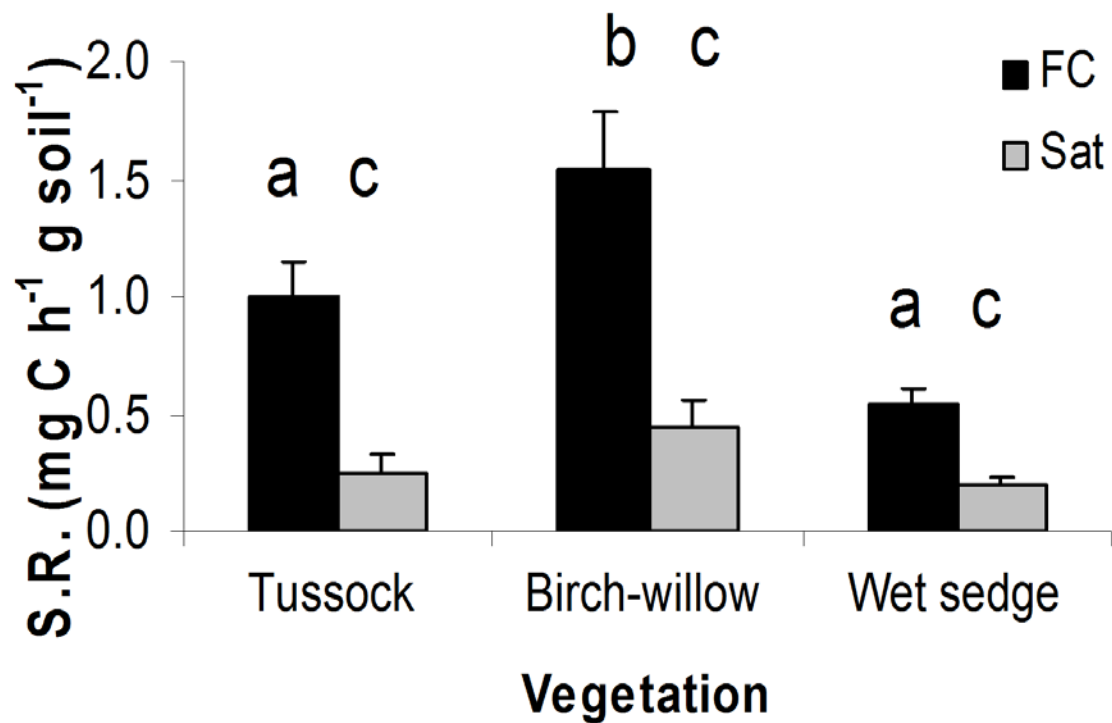


Fig. 6.6. Effects of moisture on soil respiration (S. R.) in ~1L airtight glass jars. Black indicates soils at field capacity (FC) conditions and grey indicates saturated (Sat) conditions. Respiration (\pm standard error, N=4) was measured by gas chromatography of headspace CO₂ from 20-30 g of soil with large roots and rhizomes removed added to the jars. Tussock and birch-willow soils received a “water addition” treatment (saturated; grey bars) and wet sedge soils received a “drying” treatment (to field capacity; black bar). Data from K. Judd (unpublished).

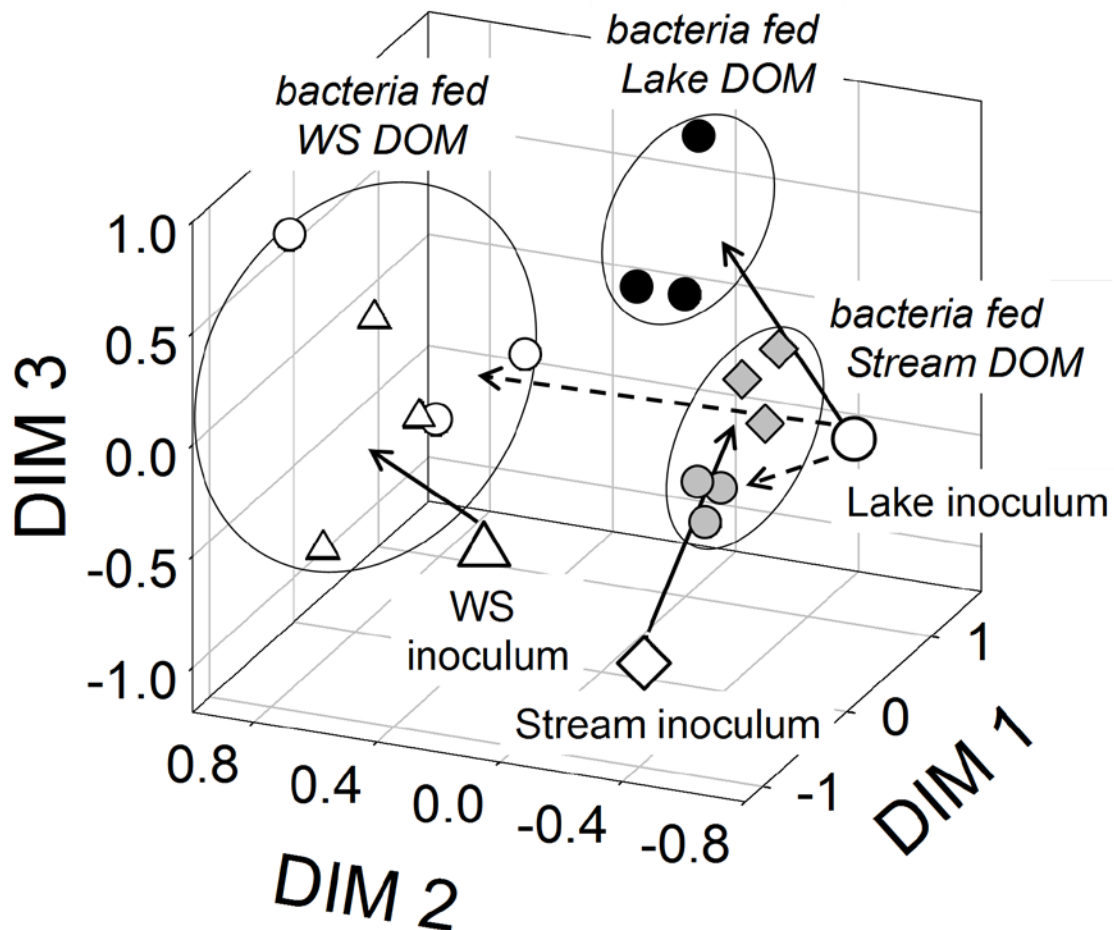


Fig. 6.7. Changes in bacterial community composition in experimental and control mesocosms. Multidimensional scaling shows the direction of change in bacterial community composition from the beginning (initial inoculum, large symbols at arrow tail) to the end (small symbols at arrow head). Symbol shape represents the source of the bacterial inoculum (circle = lake; diamond = stream; square = wet sedge soil water), and symbol shading indicates the DOM source (black = lake; gray = stream; open = soil water). Note that the “control” community for comparisons was the ending, not the beginning, community (modified with permission from Judd et al. 2006).

Phytoplankton-based Summer Community:
Moderate Bacterial Activity

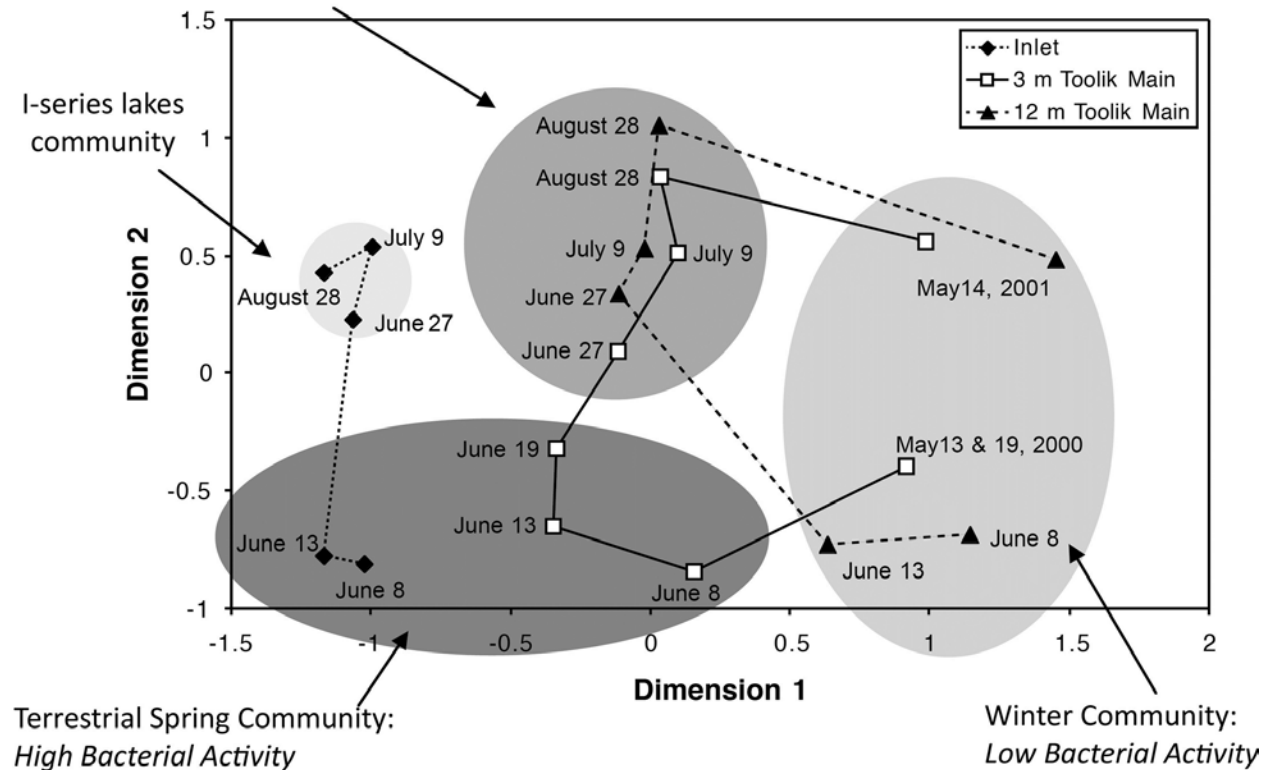


Fig. 6.8. Multidimensional scaling calculated from DGGE banding patterns, showing consistent shifts in bacterial productivity and community composition in Toolik Lake throughout the annual cycle (modified with permission from Crump et al. 2003).

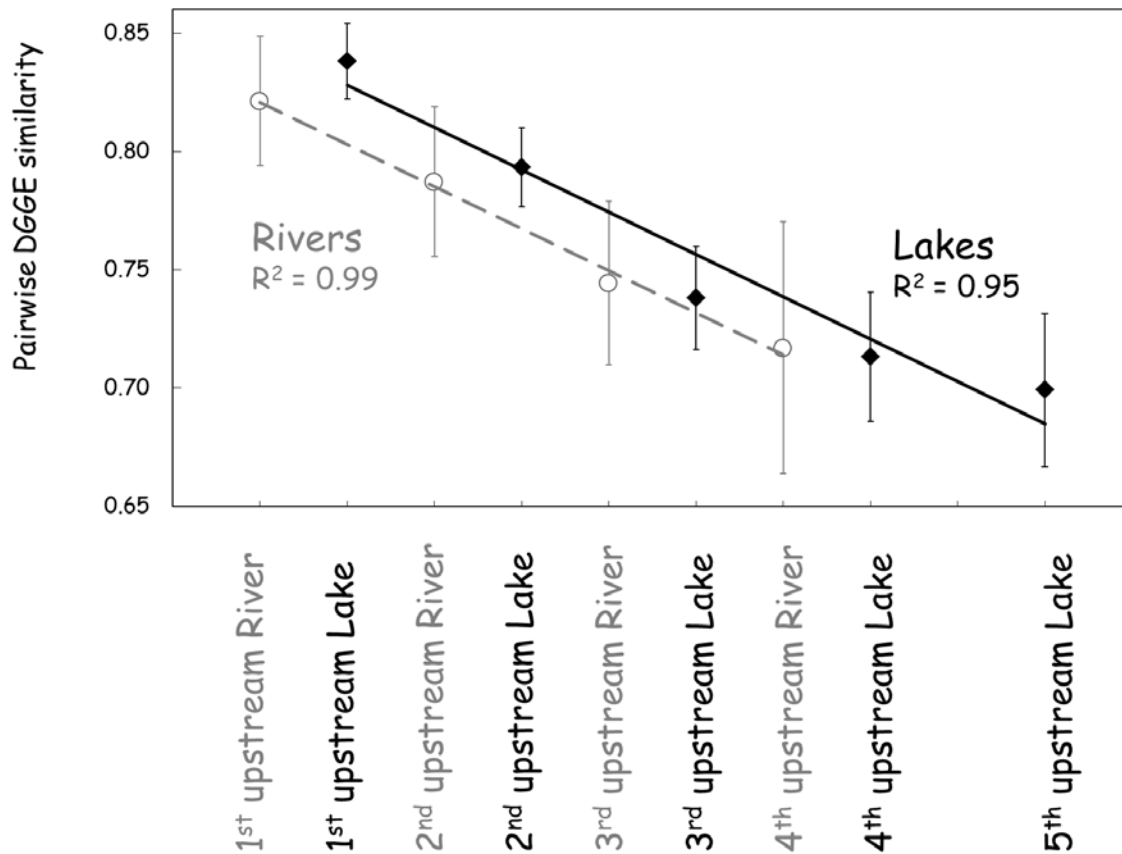


Fig. 6.9. Average pairwise similarity values for DGGE banding patterns plotted against the degree of landscape separation. This separation is a categorical variable representing the number of upstream lakes or inlets separating two sites. X-axis values of '1st upstream lake' mean that comparisons are made between any lake and its closest upstream lake, and '1st upstream river' compares a lake inlet stream with its closest, nearby inlet stream. X-axis values of '2nd upstream lake or stream' represent a separation of two upstream lakes or two lake inlets. Error bars indicate standard error of all possible combinations within a category (with permission from Crump et al. 2007).

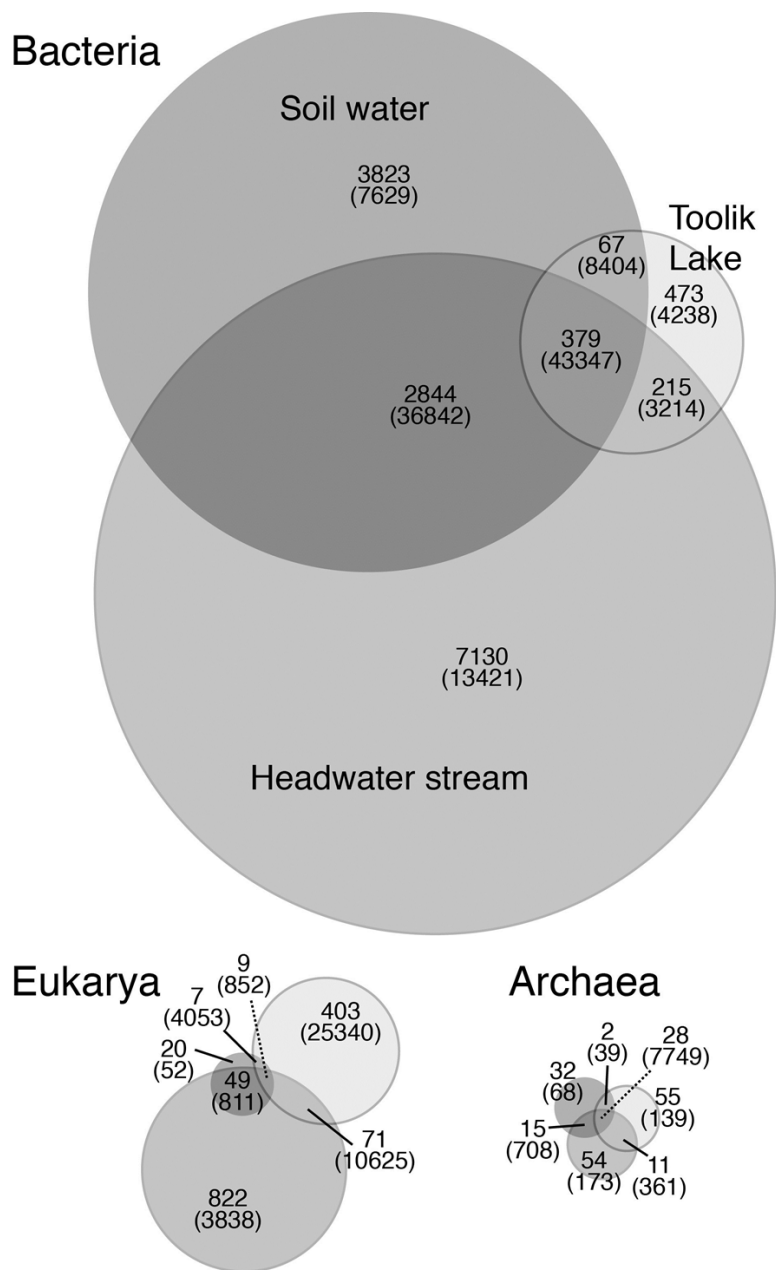
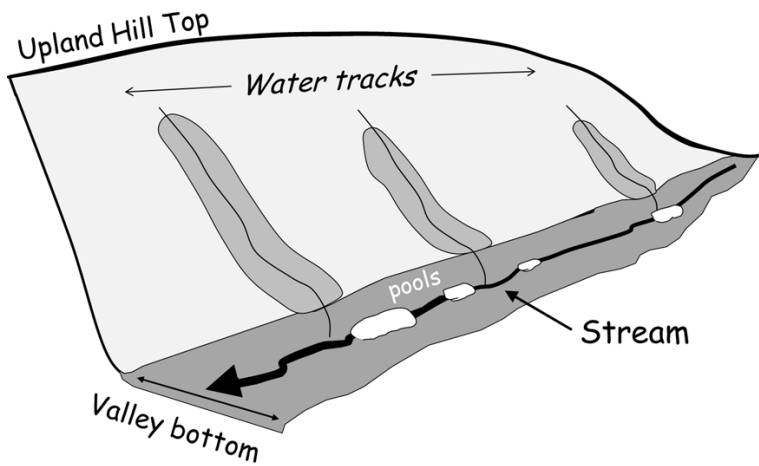


Fig. 6.10. Venn diagram showing the number of shared bacterial, archaeal and eukaryotic taxa (in bold, defined by 97% sequence similarity) among soil water, headwater stream, and lake samples. The three circles indicating soil, stream, and lake are in the same relative position for each group shown, Bacteria, Archaea, and Eukarya. The number of sequences associated with taxa is shown in parentheses (with permission from Crump et al. 2012).

A Hillslope as a Model Landscape



Controls on biogeochemical processes and catchment export

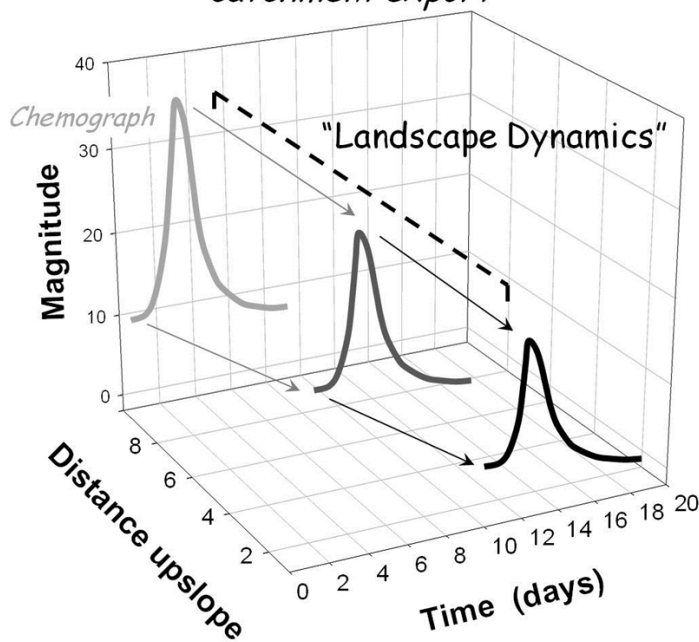


Fig. 6.11. The hillslope (Top) as a representative landscape model, with landscape components represented by the toposequence from upland heath to mid-slope tussock tundra to valley wet sedge vegetation, connected hydrologically by water tracks and riparian birch-willow vegetation. "Landscape dynamics" (Bottom) in 3-D can be represented by changes in patterns or processes (e.g., a chemograph of soil water chemistry) moving from upslope to downslope and through time.

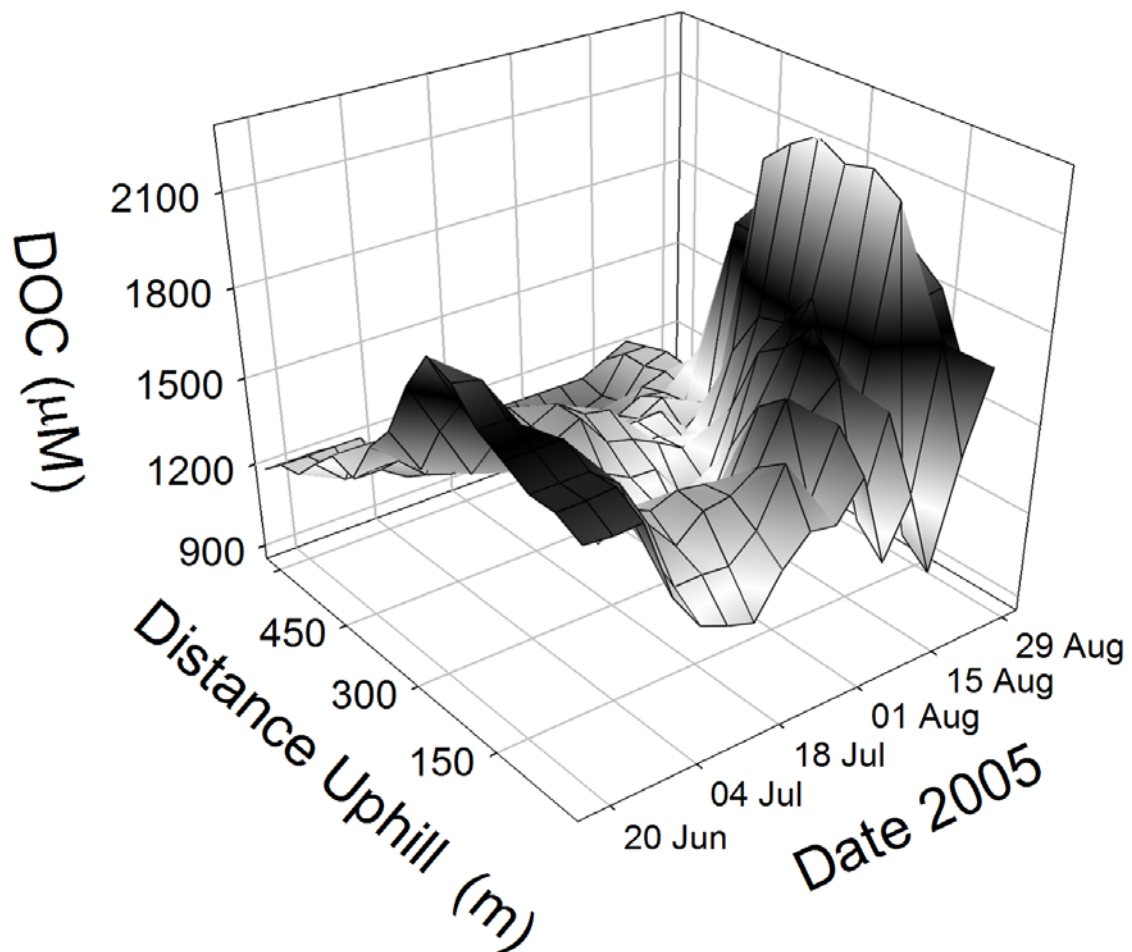


Fig. 6.12. Plot showing the concentration of DOC (μM) in soil waters along the toposequence at Imnavait Creek through the summer of 2005 (X-axis). The stream is located at the bottom of the graph, and the hilltop is at the top of the graph (Y-axis, distance uphill) following the layout in Fig. 6.11.

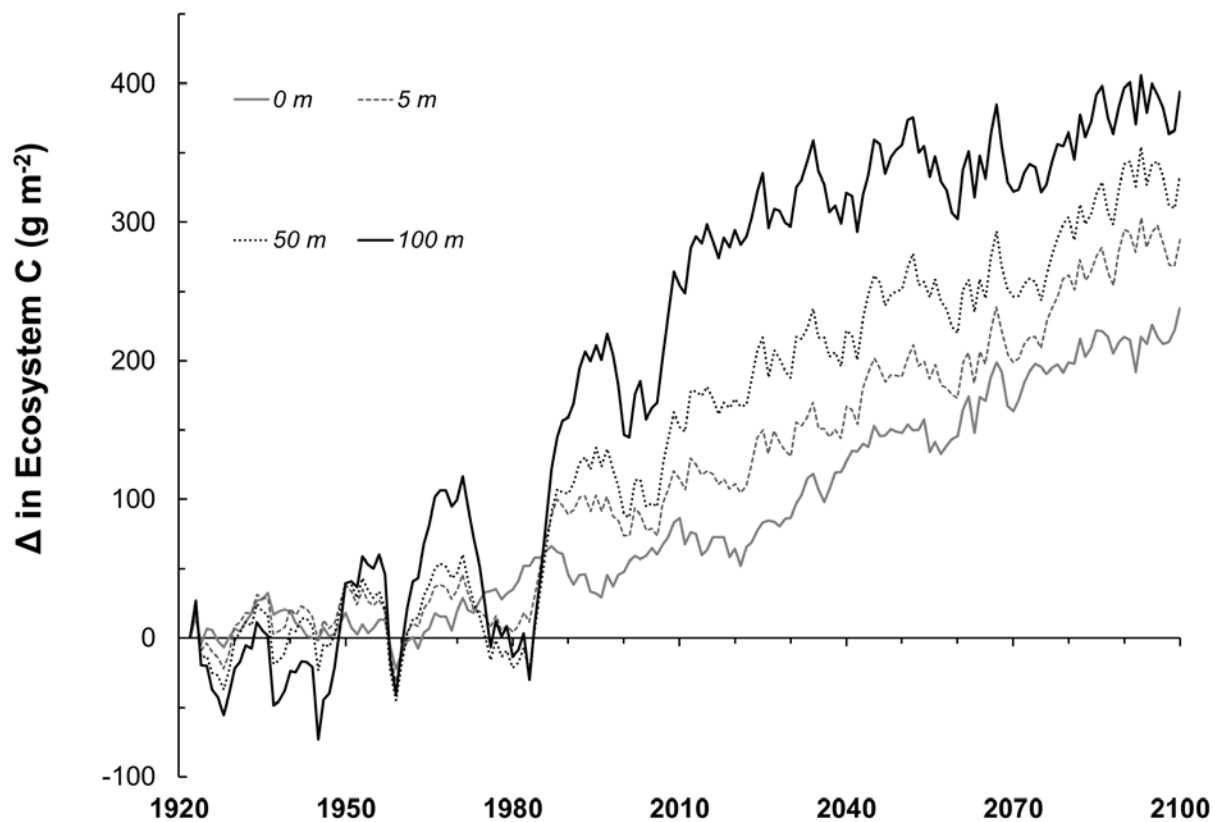


Fig. 6.13. Model-simulated changes in ecosystem C stores (g m^{-2}) along a hillslope transect of tussock tundra with points ranging from 0 to 100 m downslope. Responses of net carbon storage to increasing atmospheric temperature and CO_2 concentrations over the next century are enhanced by the downslope movement of nutrients and water (with permission from Rastetter et al. 2004).

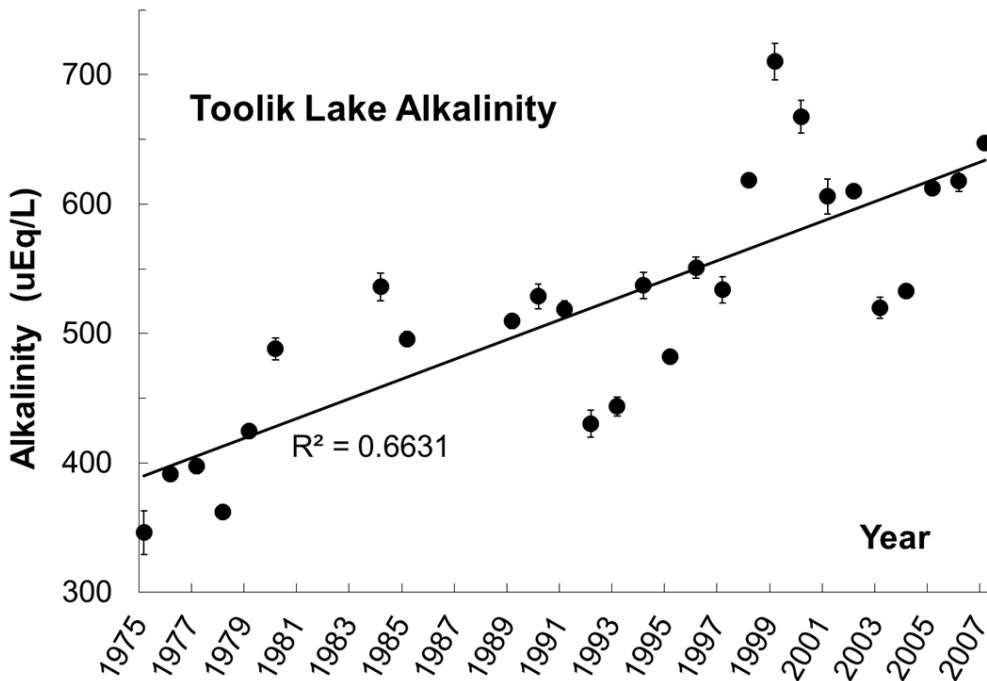
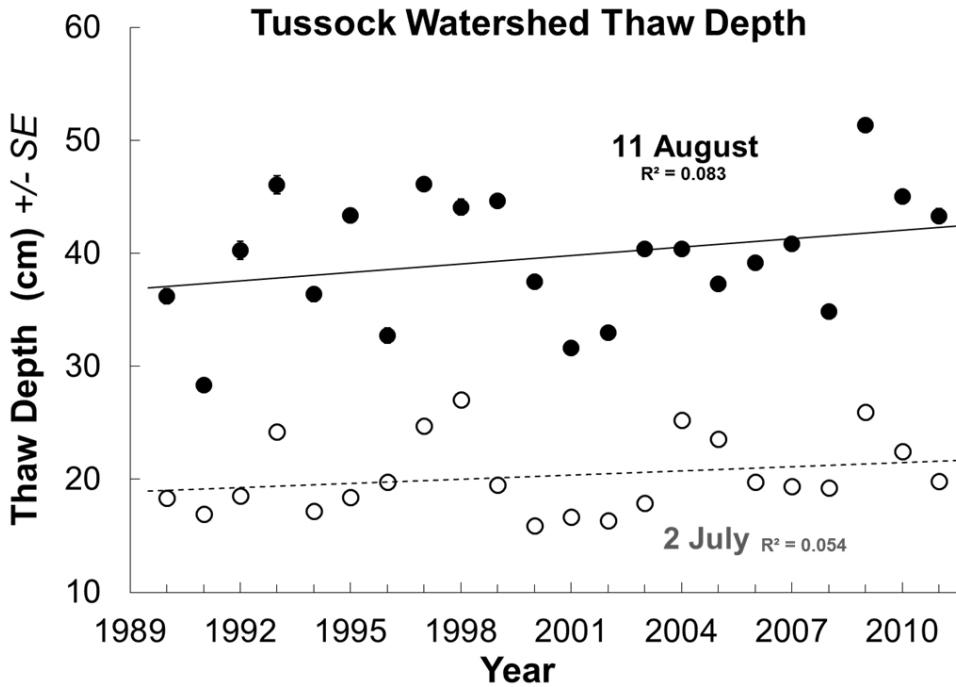


Fig. 6.14. Summer thaw depth in July and August in the Tussock Watershed near Toolik Lake (Top), showing no statistically significant trends over time. The mean summer alkalinity in Toolik Lake (Bottom) has increased over time. Standard error bars of mean values are often hidden by the points in both plots.

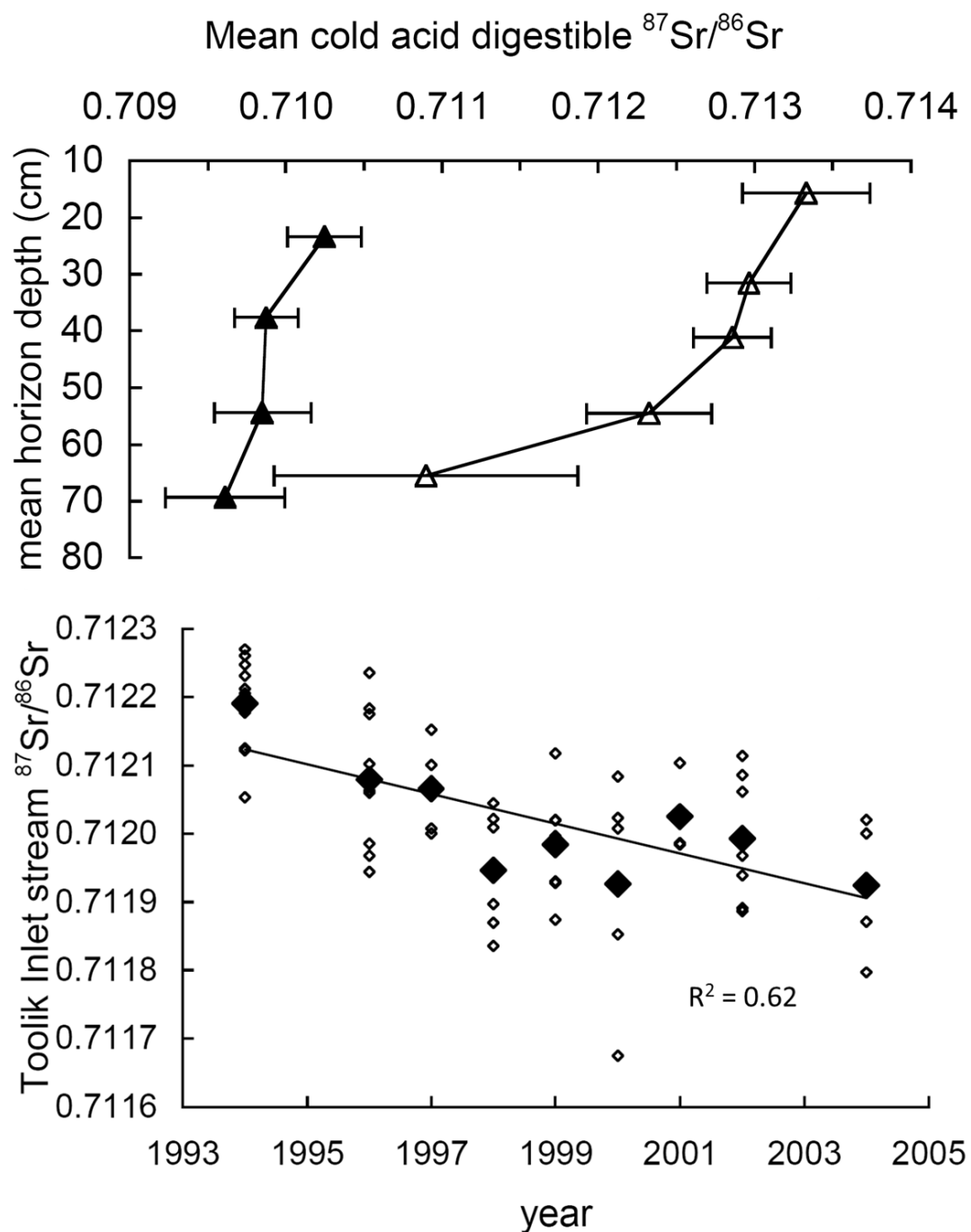


Fig. 6.15. Strontium isotope ratios decrease with depth in older (filled) and younger (open) soils (Top). Strontium isotope ratios in the inlet stream to Toolik Lake over time (Bottom). Modified with permission from Keller et al. (2007, 2010).

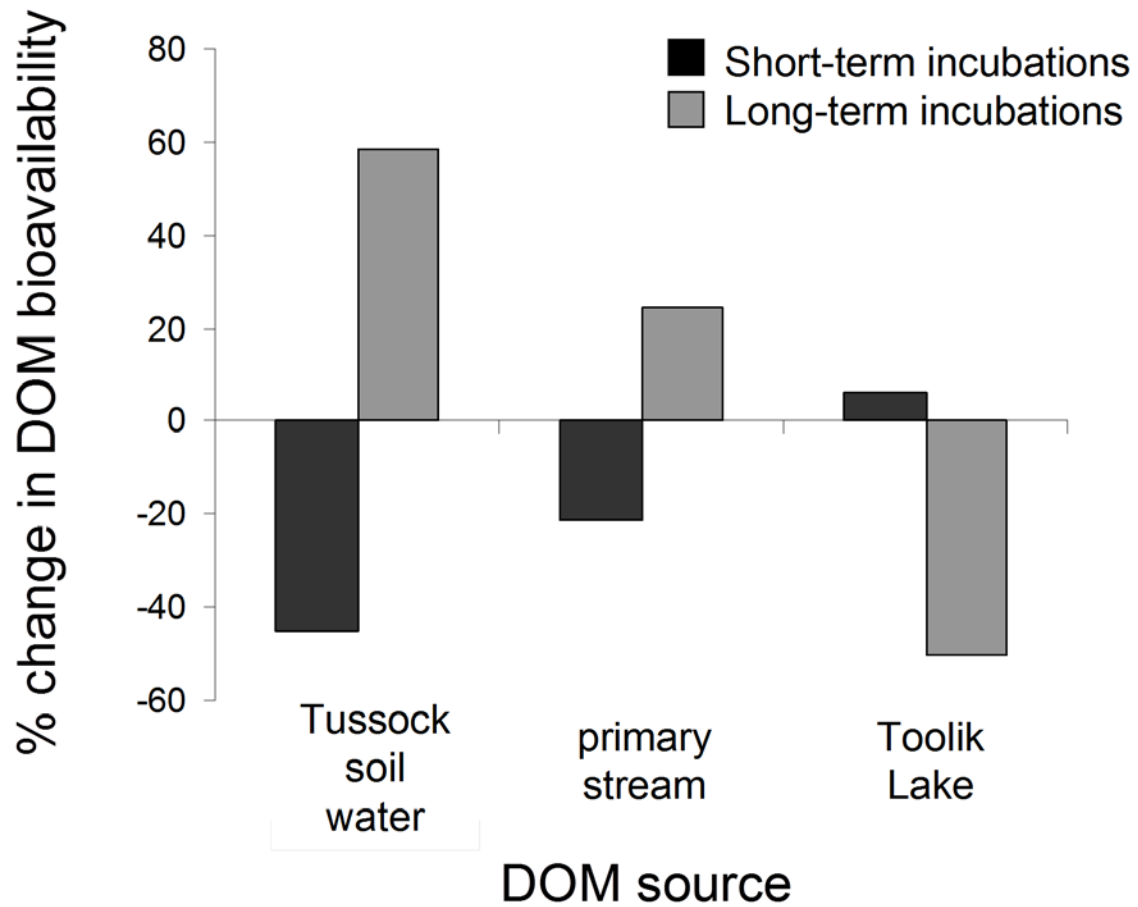


Fig. 6.V1. Effect of photo-oxidation on DOM bioavailability. Bars indicate percent change in bacterial production ($\mu\text{g C L}^{-1} \text{ d}^{-1}$) standardized by DOC concentration (mg C L^{-1}) in short- term (hours) and long-term (weeks). Values from data in Judd et al. (2007).

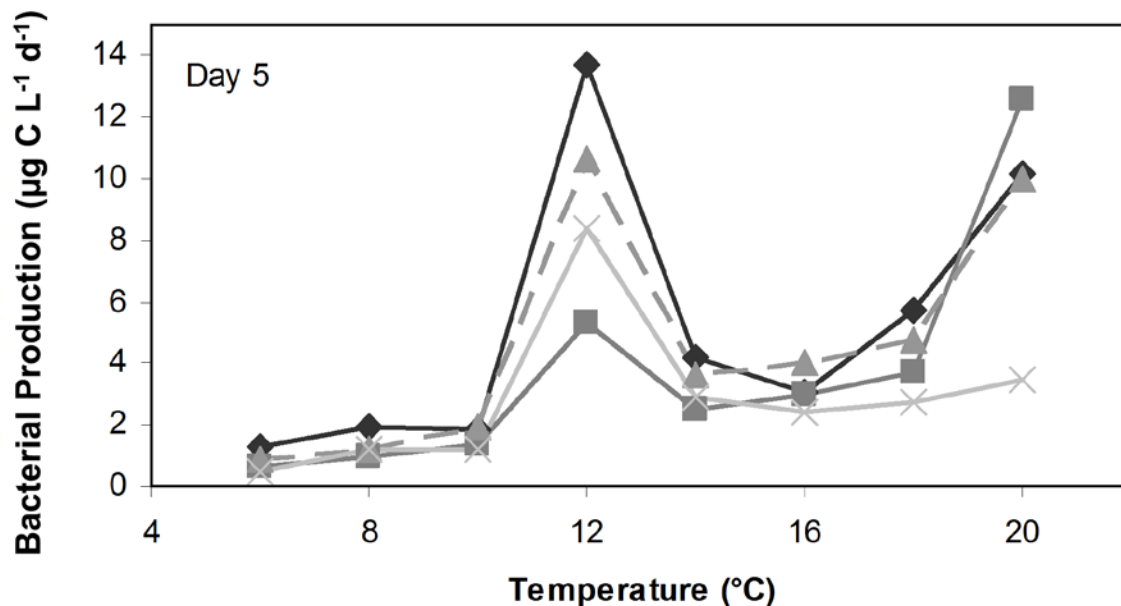


Fig. 6.V2. Bacterial activity at different temperatures after five days of incubation with bacteria and DOM from Toolik Lake inlet and outlet, July 2004. Symbols indicate different locations and carbon sources: Diamonds = inlet community plus inlet DOM (control); Triangles = outlet community plus inlet DOM; Crosses (X) = outlet community plus outlet DOM (control); Squares = inlet community plus outlet DOM. Regardless of C source, two distinct temperature optima developed (modified with permission from Adams et al. 2010).

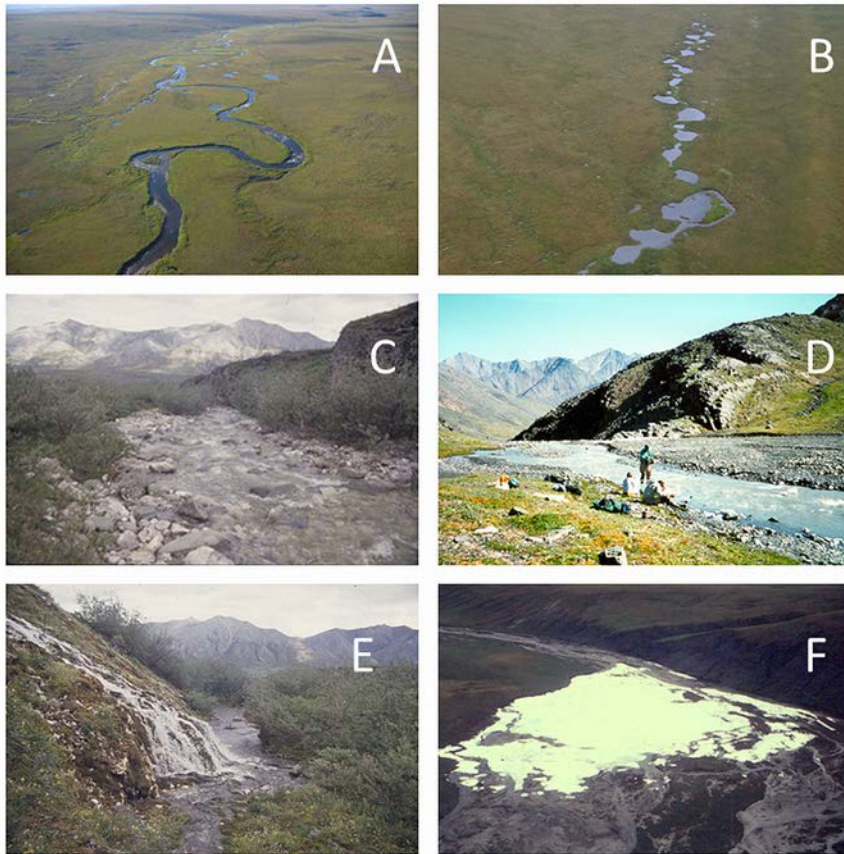


Fig. 7.1. Stream types in the Toolik Lake Region. (A) Meandering tundra stream, Kuparuk River. (B) Beaded tundra stream, Imnavait Creek. (C) Mountain stream, Ivishak Stream. (D) Glacial stream, Gates Glacier. (E) Mountain spring stream, Ivishak Spring. (F) Aufeis from a mountain spring, Flood Creek area. Photo credits: W.B. Bowden except (D) by B. Peterson.

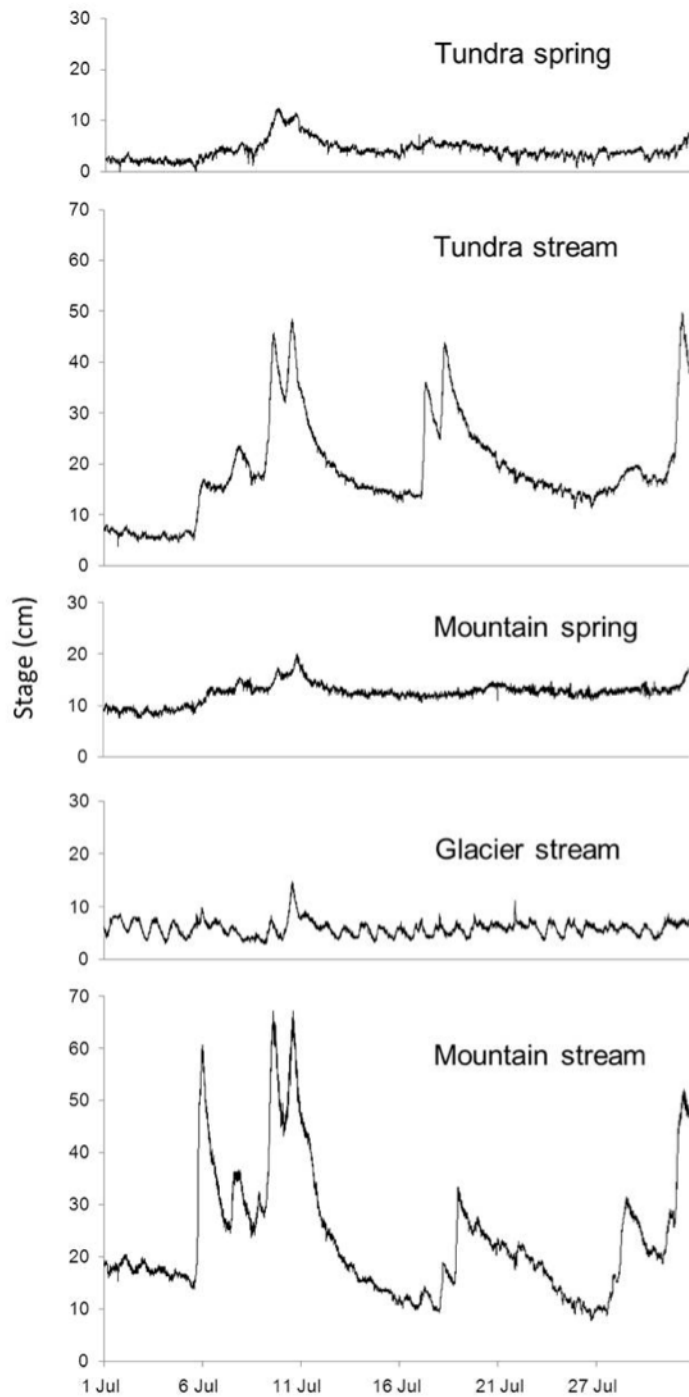


Fig. 7.2. Seasonal variability of stage (water depth) in five types of arctic streams. Discharge is directly related to stage, but the relationship is different for each of these stream types. From Parker (2008).

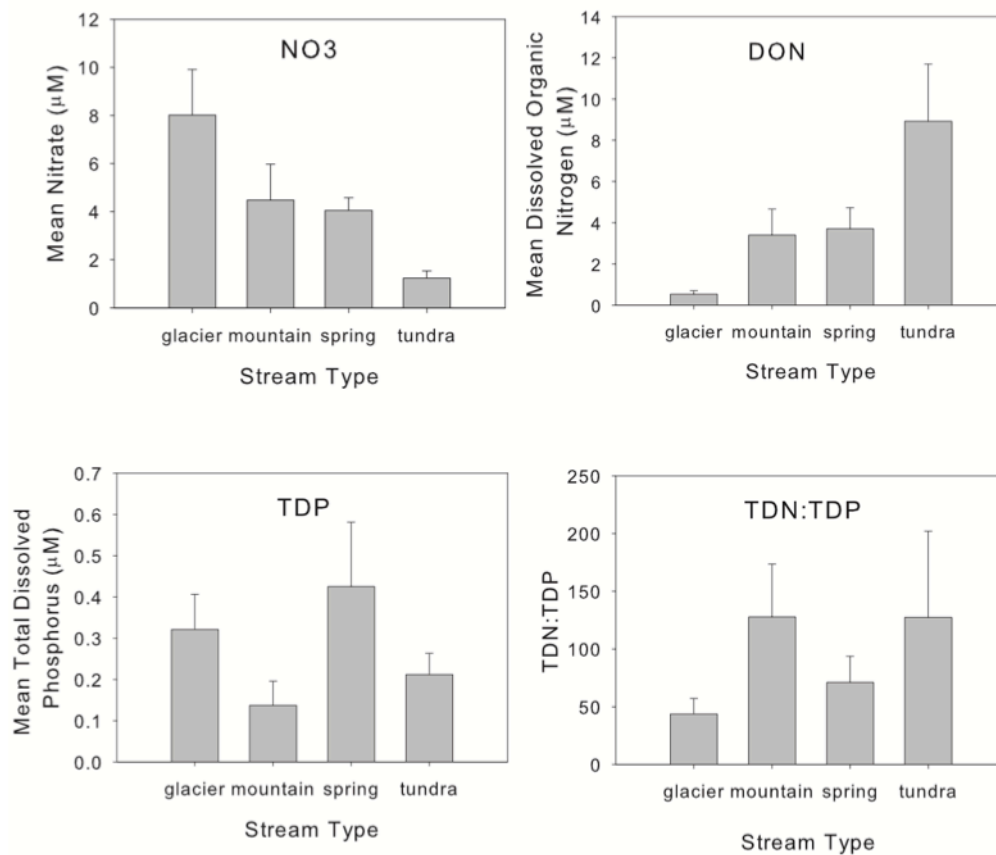


Fig. 7.3. Concentrations of nitrate (NO_3), dissolved organic nitrogen (DON), total dissolved phosphorus (TDP), and the ratio TDN:TDP for streams in the region of Toolik Lake. TDN is effectively the sum of NO_3 plus DON.

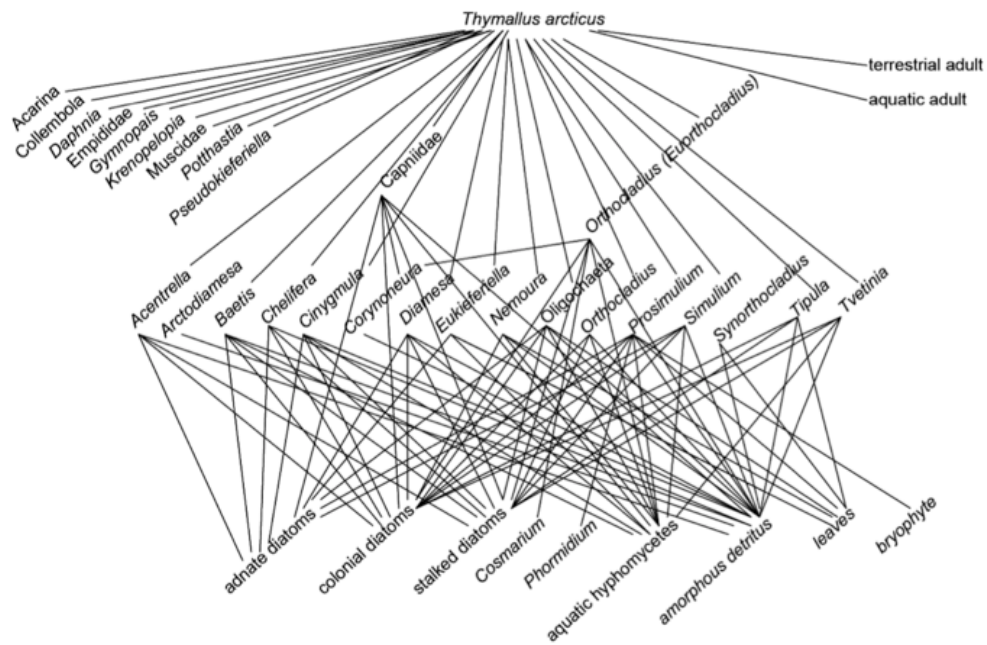


Fig. 7.4. Food web structure in the Kuparuk River, a typical tundra stream. From Parker (2008).

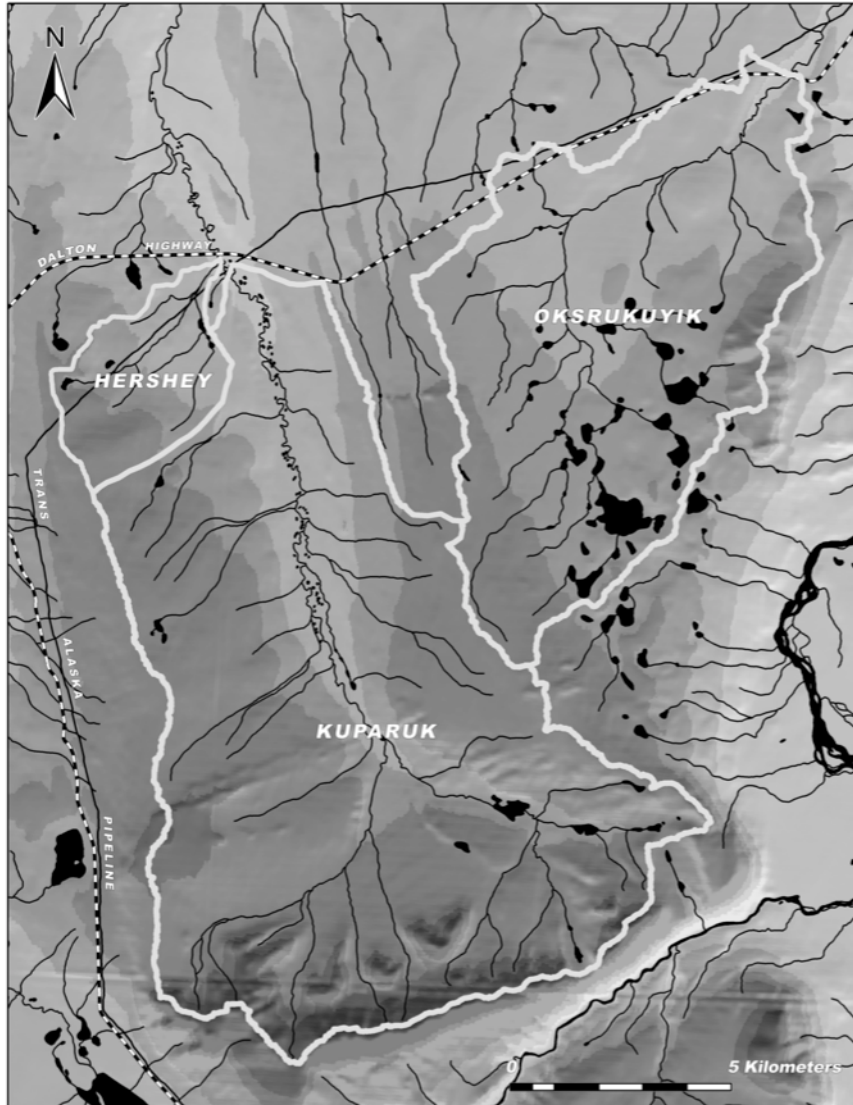
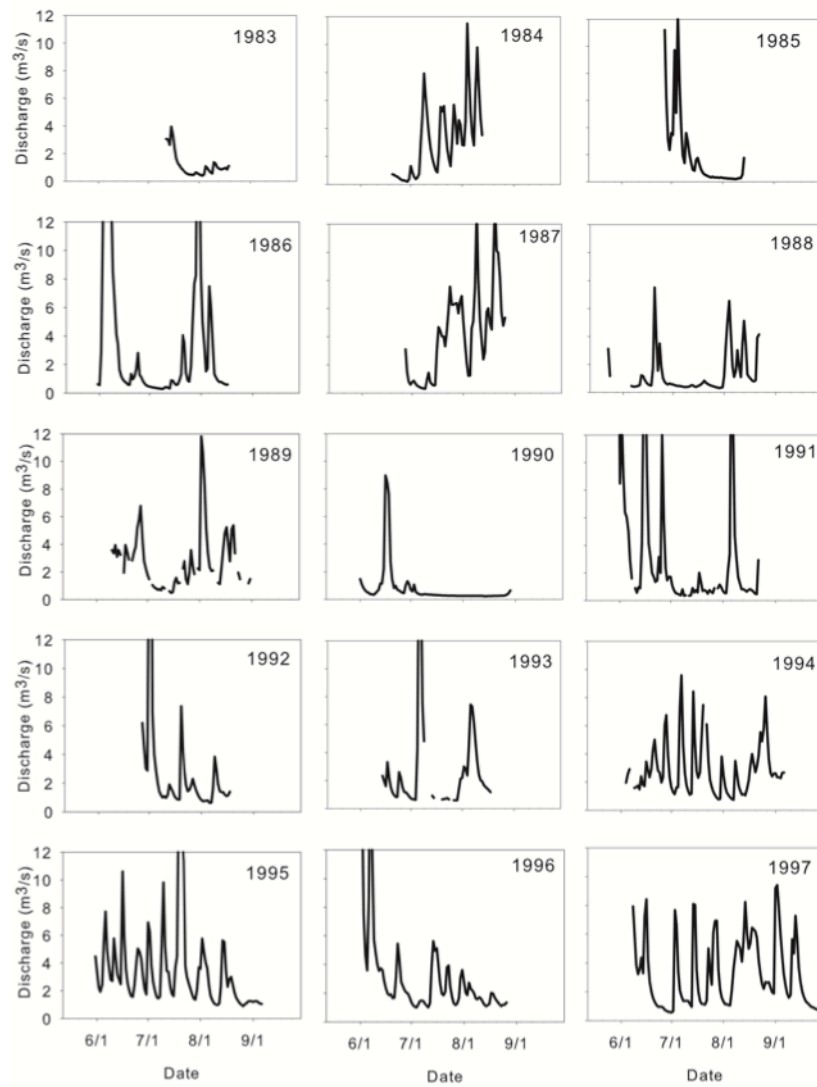


Fig. 7.5. Map of the upper Kugaruk River and Oksrukuyik watersheds (maps from J. Stuckey and R. Fulweber, Toolik Field Station GIS and Remote Sensing Facility).



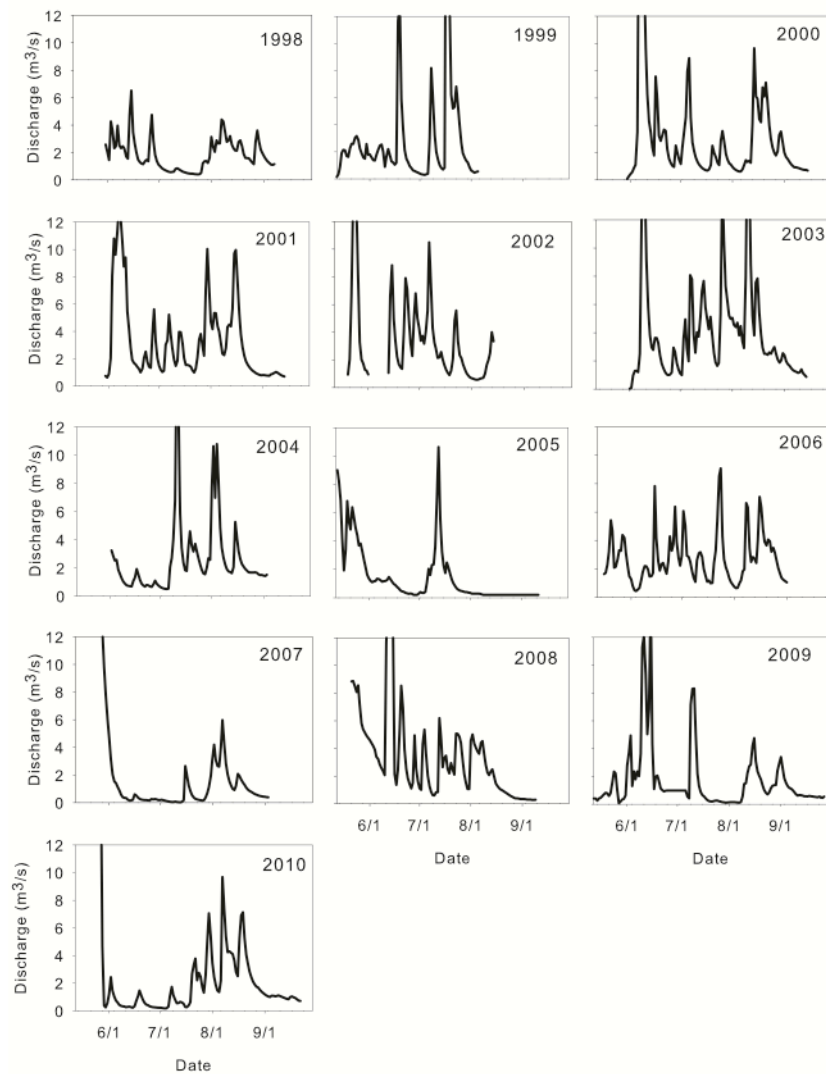


Fig. 7.6A, B. Annual discharge regime of the Kuparuk River, 1983-2010. Updated with permission from the Ecological Society of America.

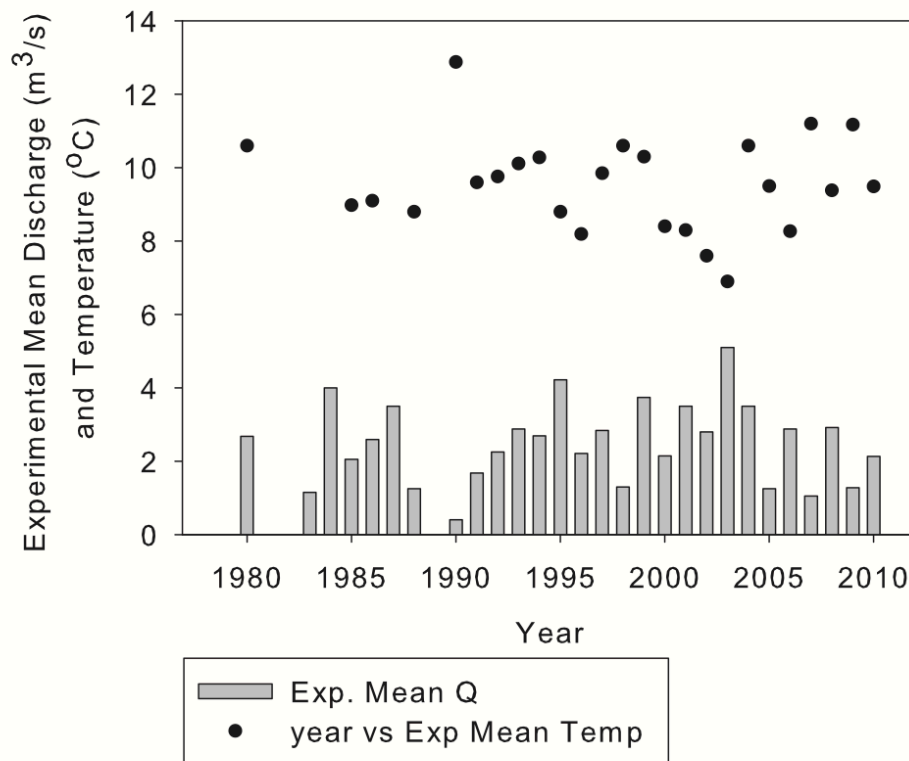


Fig. 7.7. Mean summer discharge and temperature during the fertilization period (June 25- August 16) in the Kuparuk River. Note: dates included in these means may vary slightly year to year, due to technical issues with equipment.

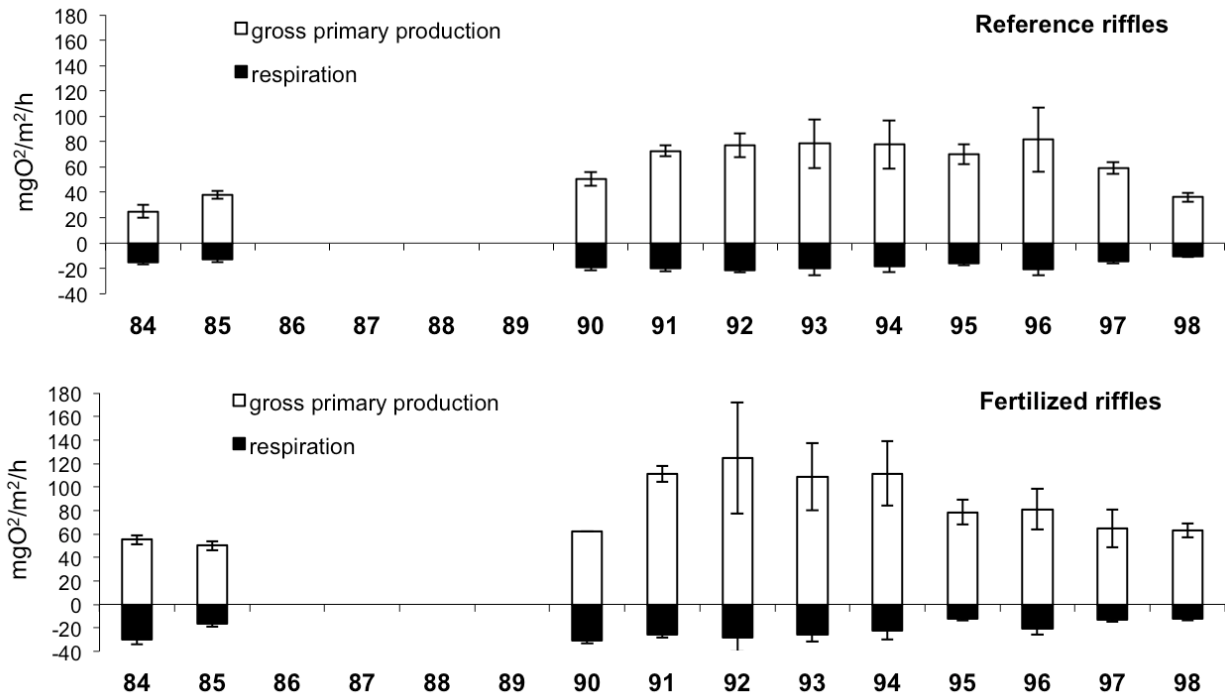


Fig. 7.8. Production and respiration from chamber experiments in the Kuparuk River. From Slavik (2004) with permission from the Ecological Society of America.

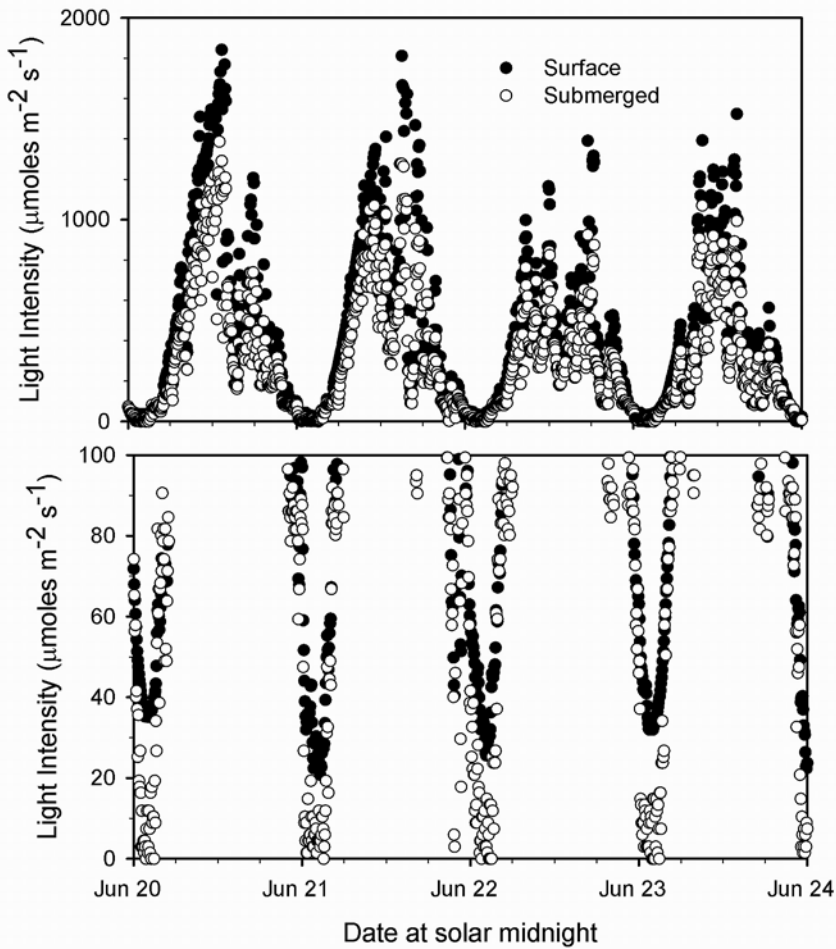


Fig. 7.9. Typical surface and subsurface light levels in the Kuparuk River. (A) 5-minute light recordings over three days near the summer solstice. (B) Magnification of midnight light values. From Cappelletti (2006).

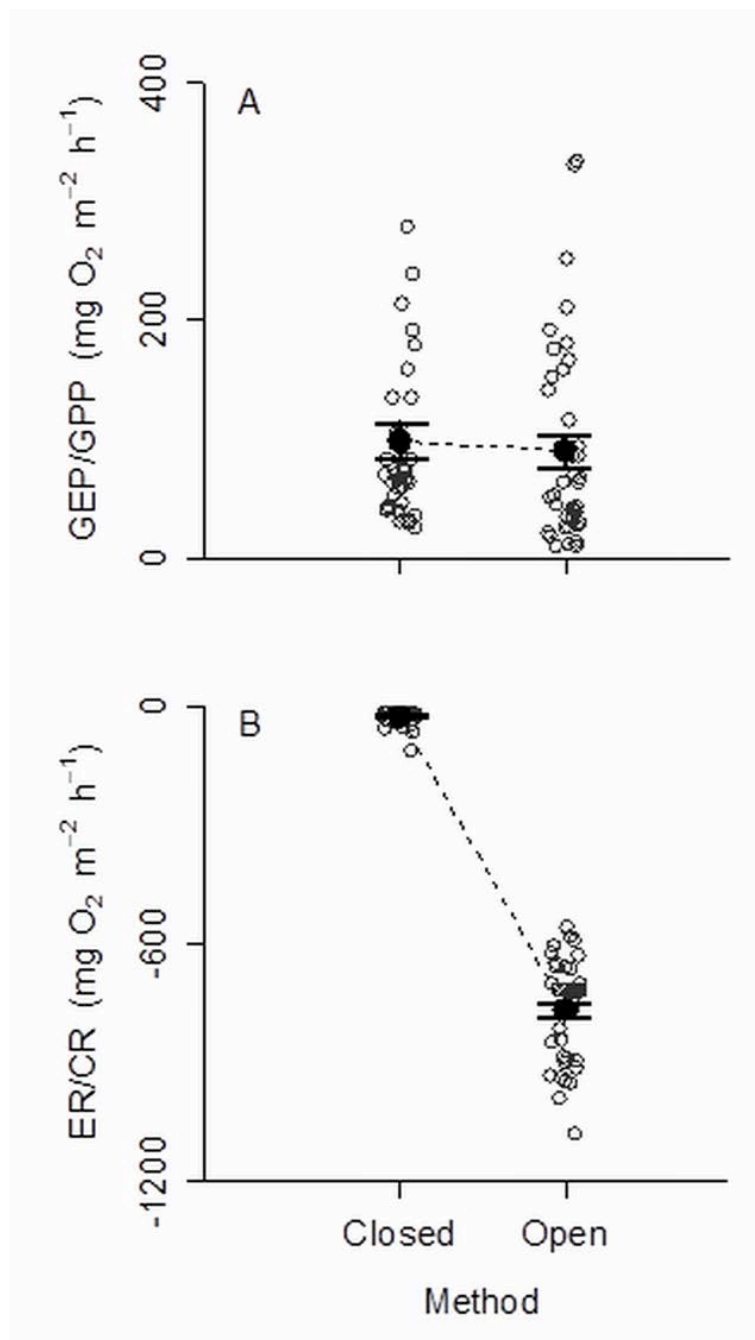


Fig. 7.10. Closed chamber versus open whole-stream estimates of metabolism in the Kuparuk River: (A) Comparison of closed-system gross primary production versus open-system gross ecosystem production (mean \pm 1 SE). (B) Comparison of closed-system community respiration versus open-system respiration (mean \pm 1 SE). From Cappelletti (2006).

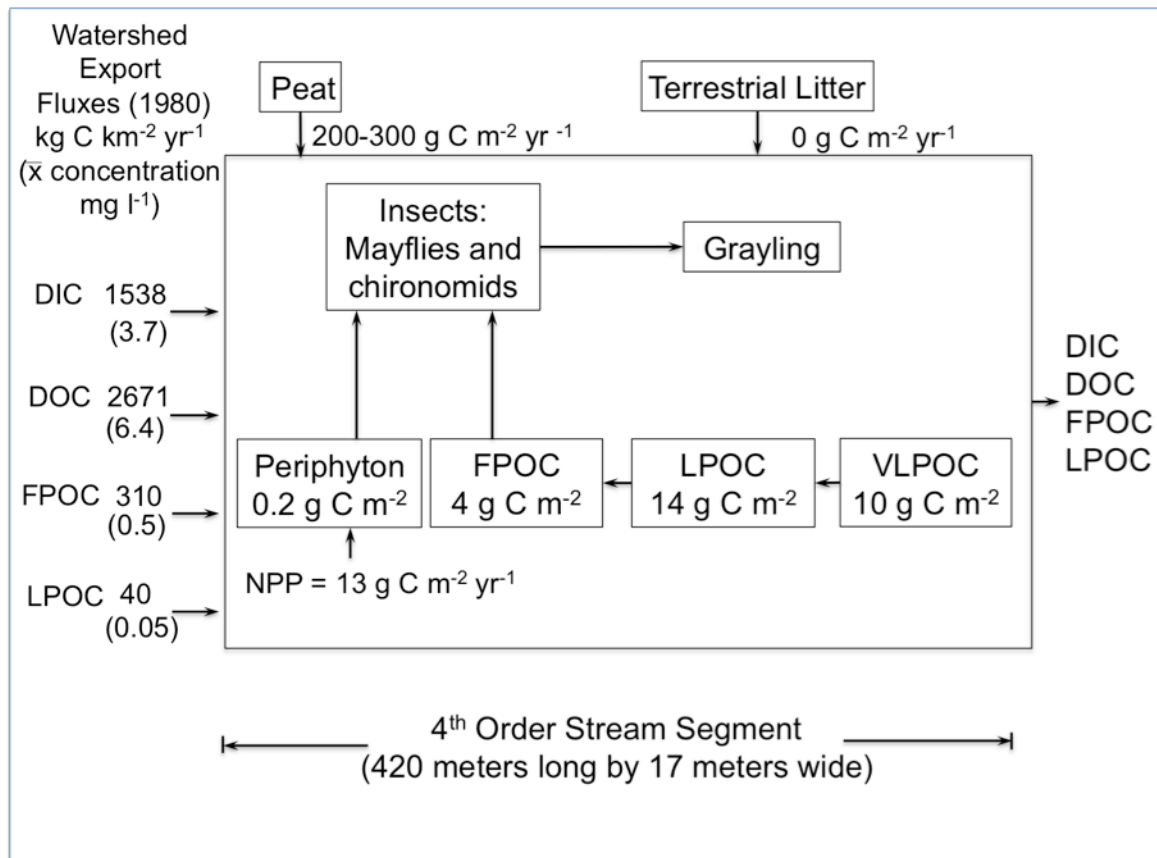


Fig. 7.11. Carbon stocks and fluxes in the Kuparuk River ecosystem.
From Peterson et al. (1986) with permission from the Canadian Journal
of Fisheries and Aquatic Sciences.

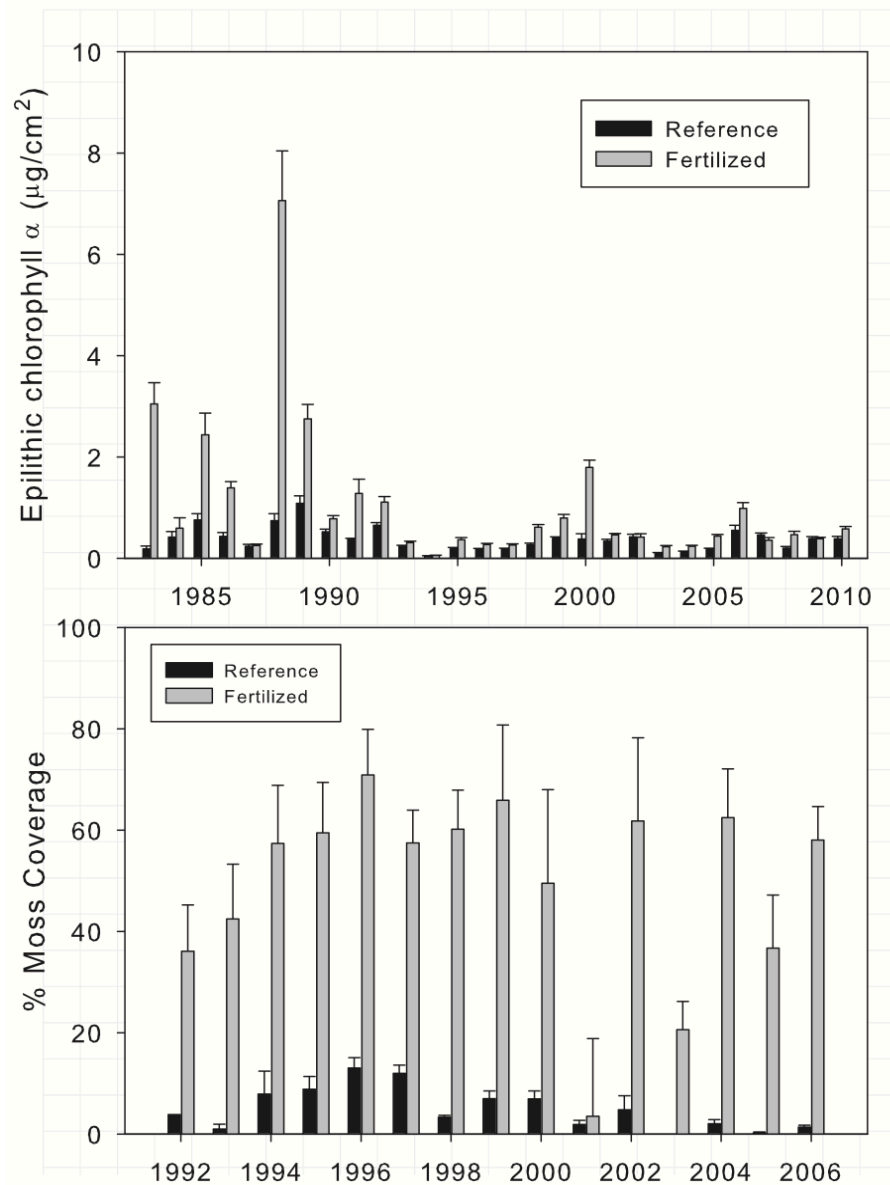


Fig. 7.12. Epilithic total chlorophyll during fertilization (top) and percentage of total bryophyte cover (bottom) in the reference and fertilized reach riffles of the Kuparuk River. Chlorophyll means for 1987 and 1994 only include August values. In 1988, fertilized reach chlorophyll values are inflated due to contamination by green algal filaments. Bryophyte cover was negligible prior to 1992. Data are means

± 1 SE. Graphs are updated versions from Slavik et al. (2004).

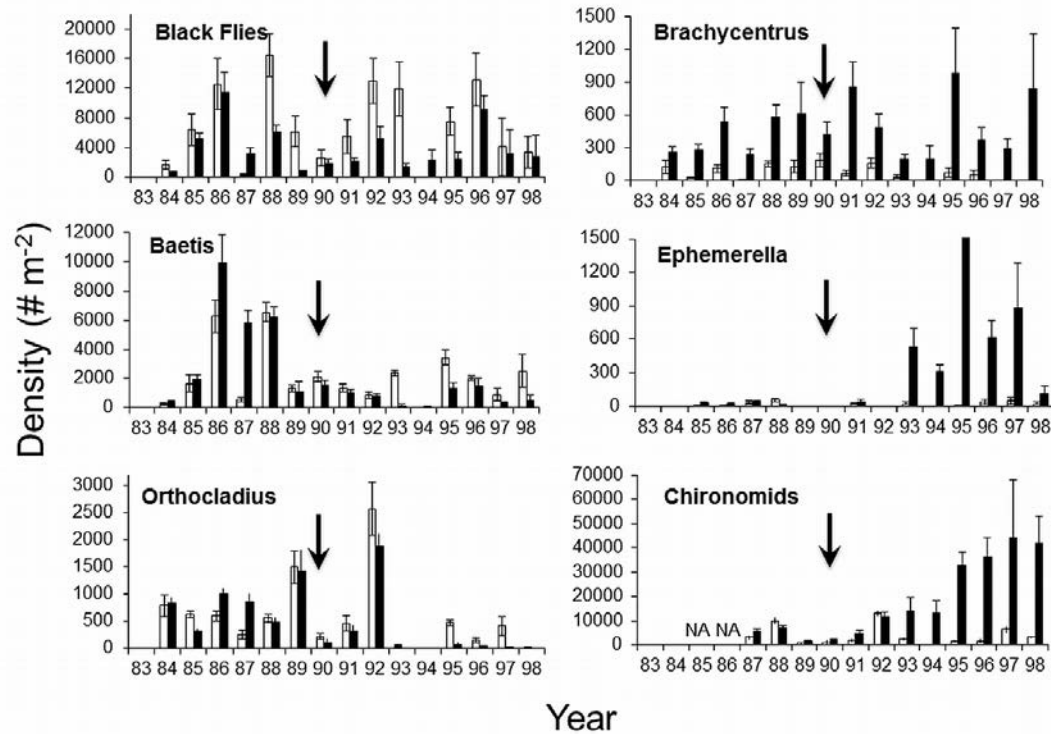


Fig. 7.13A, B. Mean July densities of six major benthic insect taxa in the Kuparuk River from 1983-1998. The shift to a moss-covered fertilized reach caused different changes in insect densities. The species on the left were disadvantaged by the moss; the species on the right benefited from the moss. The mosses appeared in 1990 (indicated by the arrows).

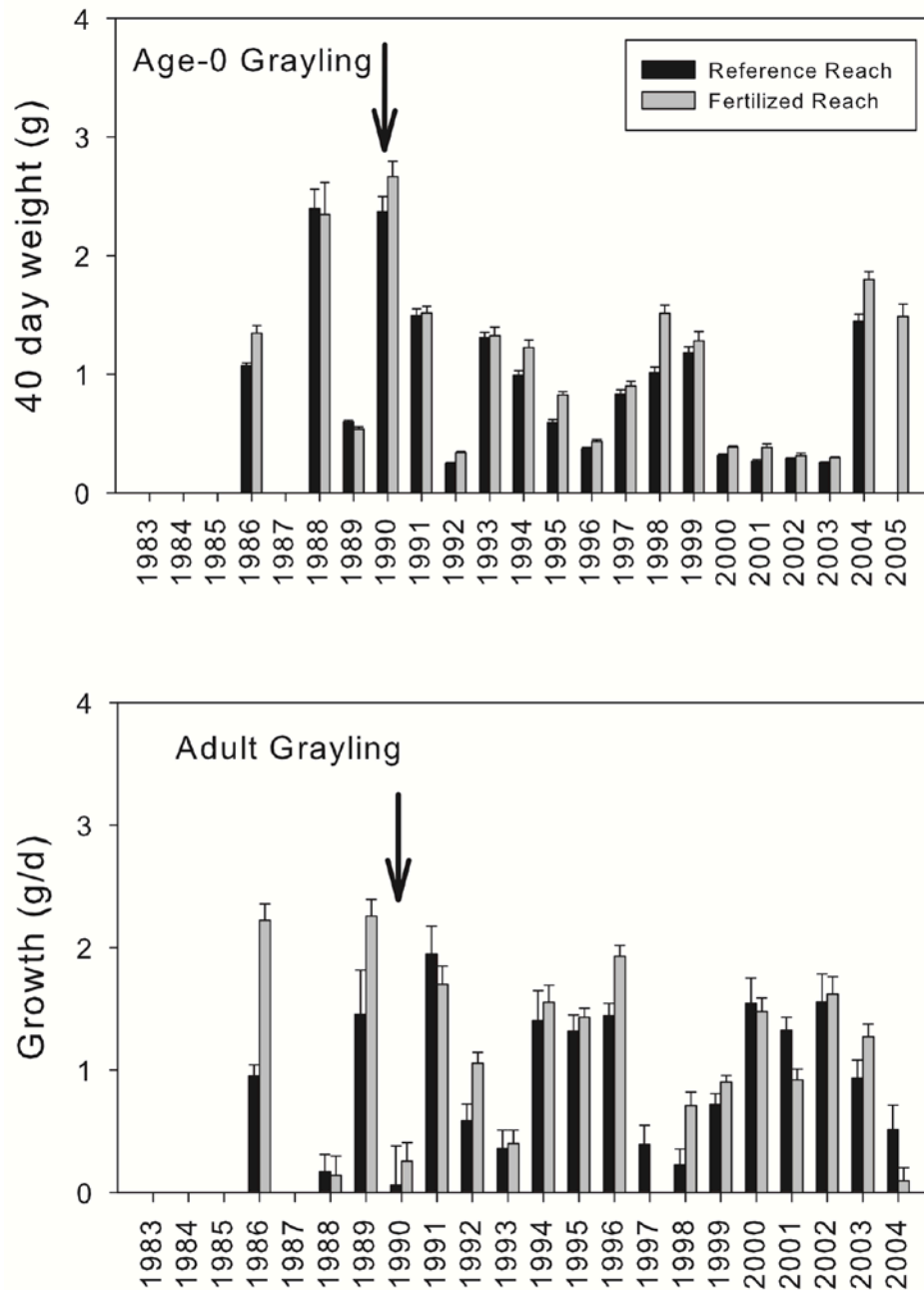


Fig. 7.14. Long-term fish response. (A) Mean age-0 grayling 40-day weight ($\text{g} \pm 1 \text{ SE}$) in the reference and fertilized reaches of the Kuparuk River. (B) Adult grayling growth (mean g d^{-1} , $\pm 1 \text{ SE}$) in the reference and fertilized reaches of the Kuparuk River. $N > 5$ for all years; the mosses appeared in 1990 (arrows). From Deegan et al. (1999) with permission from the American Fisheries Society.

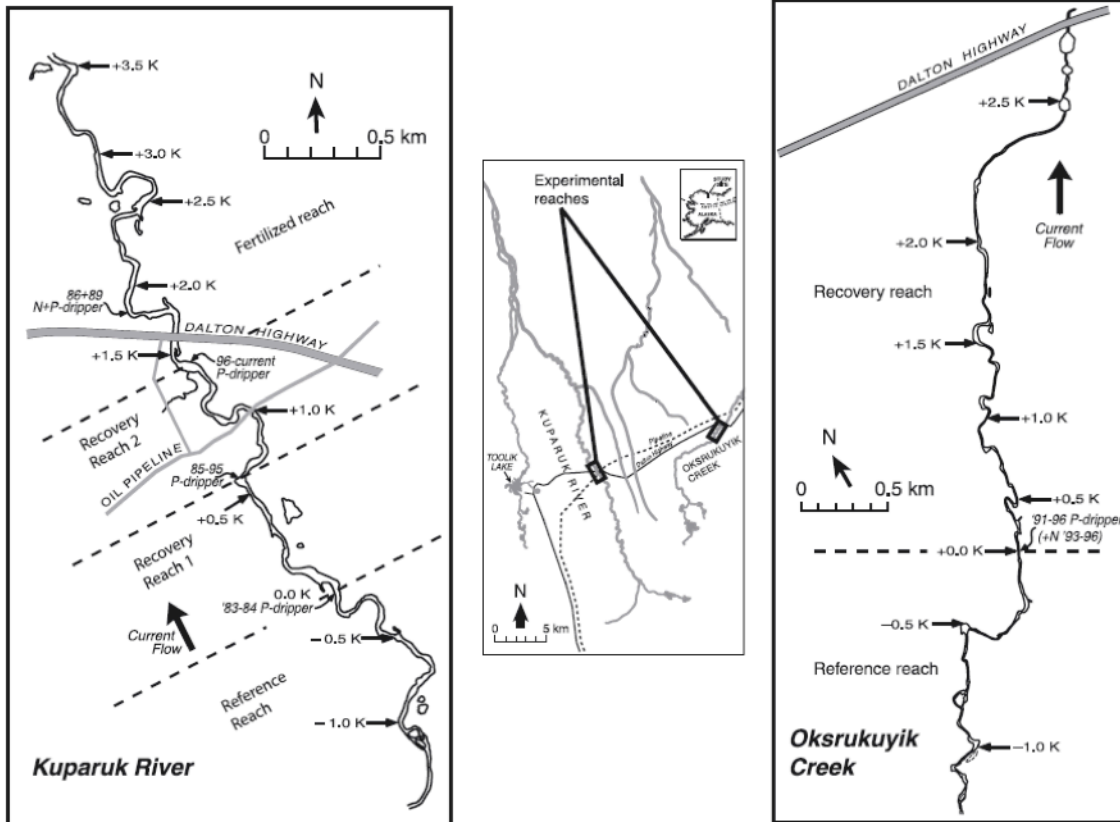


Fig. 7.15. Maps showing the reference and recovery reaches of the Kuparuk River (left) and Oksrukuyik Creek (right), and the location of the two rivers on Alaska's North Slope (center). The phosphorus addition site on the Kuparuk River was moved downstream in 1985 and again in 1996, forming the two recovery reaches: Recovery 1 (fertilized for 2 years) and Recovery 2 (fertilized for 13 years). Oksrukuyik Creek (right) was fertilized for 6 years. From Benstead et al. (2007) with permission from Freshwater Biology.

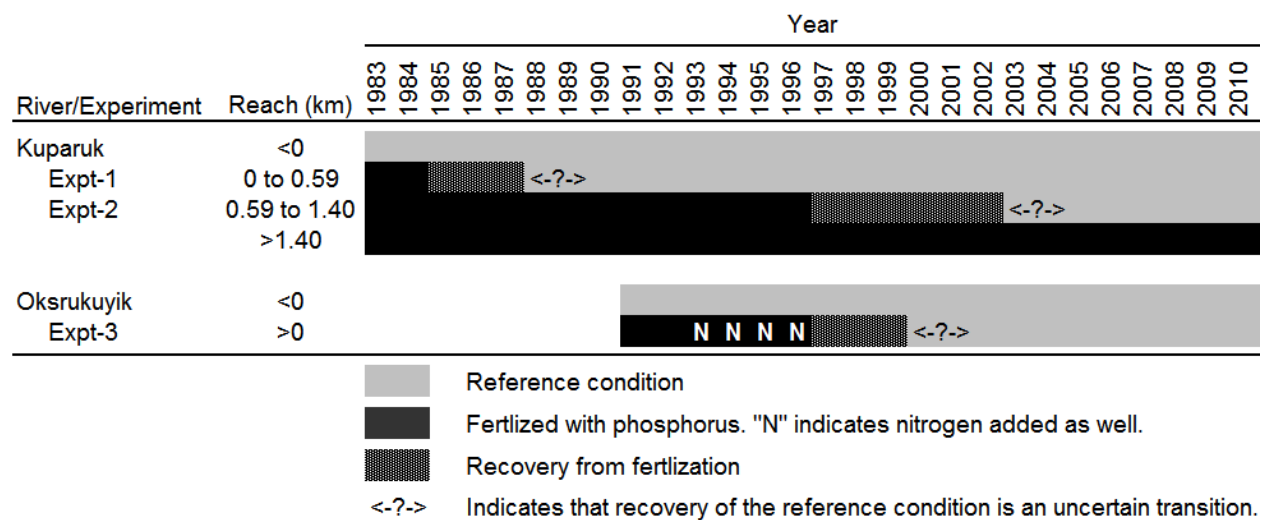


Fig. 7.16. Time course of fertilization experiments on the Kuparuk River and Oksrukuyik Creek near Toolik Lake Alaska indicating the locations (reaches) and time intervals of the recovery process.

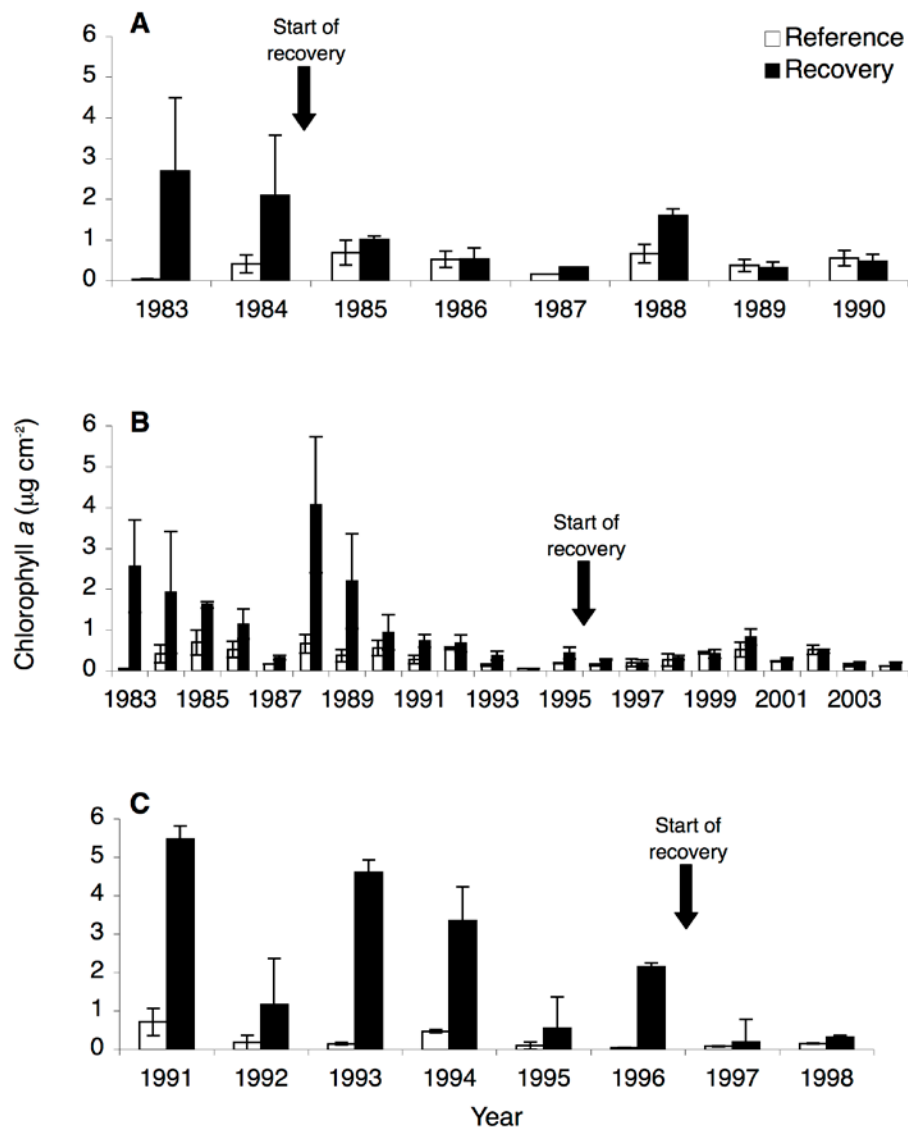


Fig. 7.17. Mean epilithic chlorophyll *a* standing crop (± 1 SE) in reference and recovery reaches of the (A) Kuparuk River, 1983-1990 (first recovery reach), (B) Kuparuk River, 1983-2003 (second recovery reach), and (C) Oksrukuyik Creek, 1991-1998. From Benstead et al. (2007) with permission from Freshwater Biology.

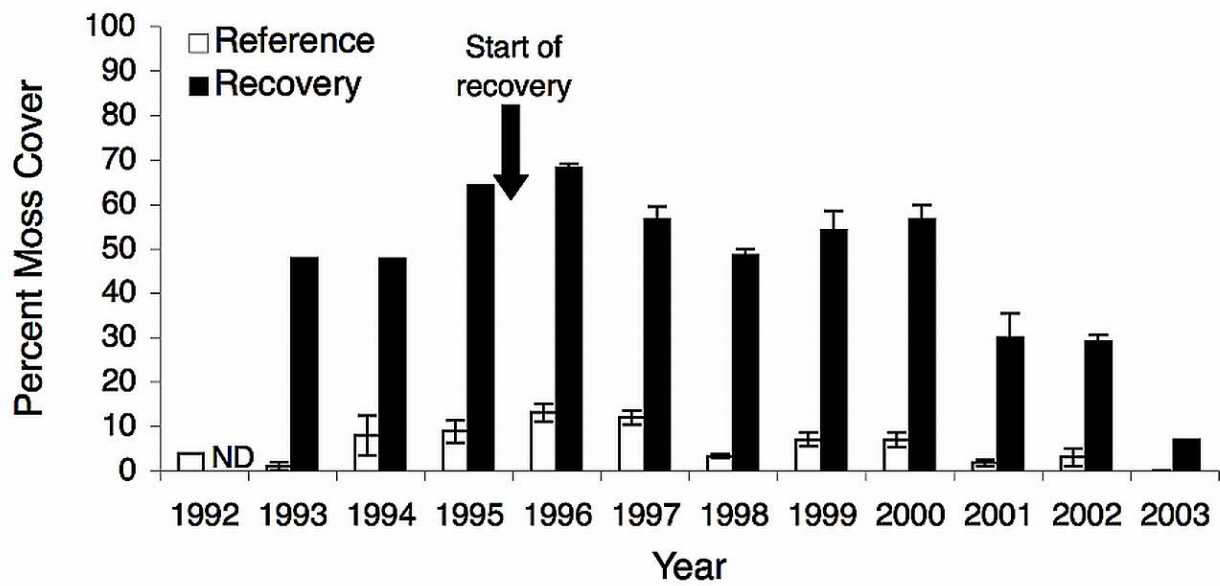


Fig. 7.18. Time course of bryophyte recovery from fertilization in the Kuparuk River. Reproduced with permission from Freshwater Biology.

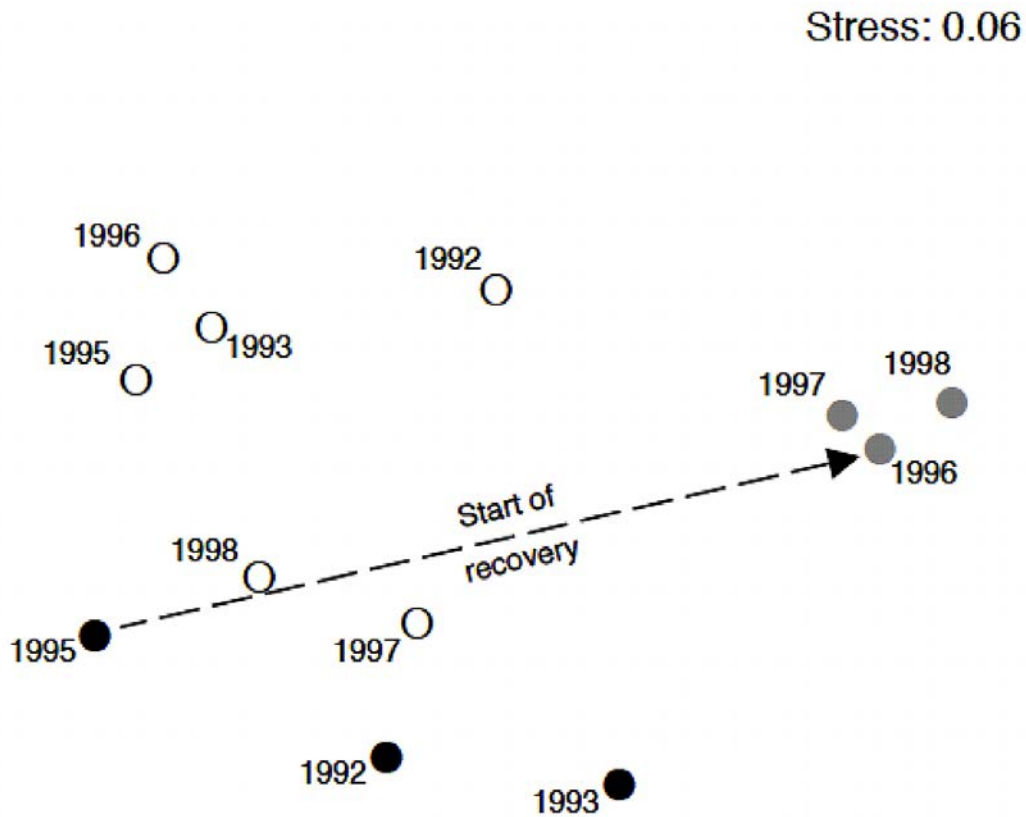


Fig. 7.19. Non-metric multidimensional scaling ordination plot of benthic macroinvertebrate samples based on Bray-Curtis dissimilarities among untransformed density data. Solid symbols are pre-recovery (fertilized) reach, grey symbols are recovery reach, and open symbols are reference reach. Arrow shows transition from fertilized to recovery conditions. No data were available for 1994. Ordination using log-transformed data showed similar patterns of recovery with an identical stress value. From Benstead et al. (2007) with permission from Freshwater Biology.

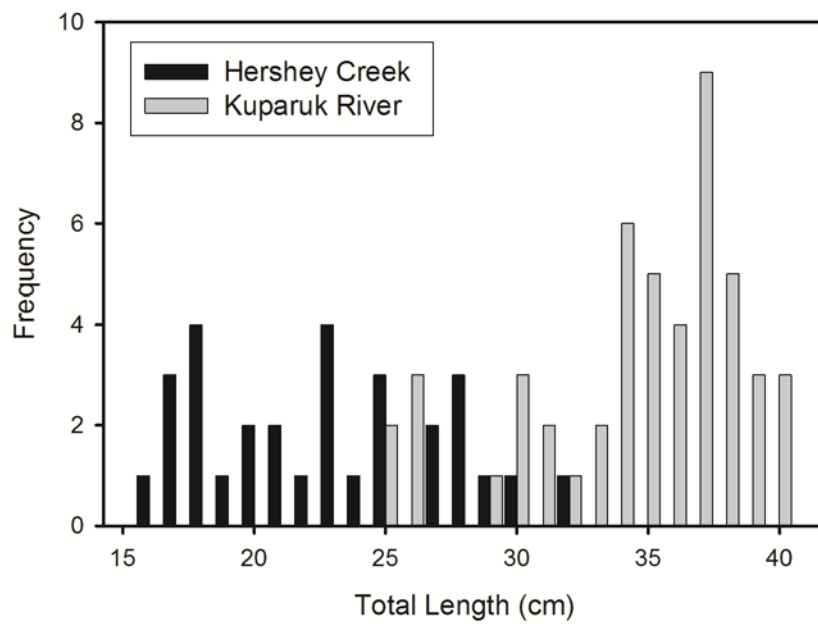


Fig. 7.20. Size distribution of arctic grayling in small (Hershey Creek) and large (Kupaaruk River) streams.

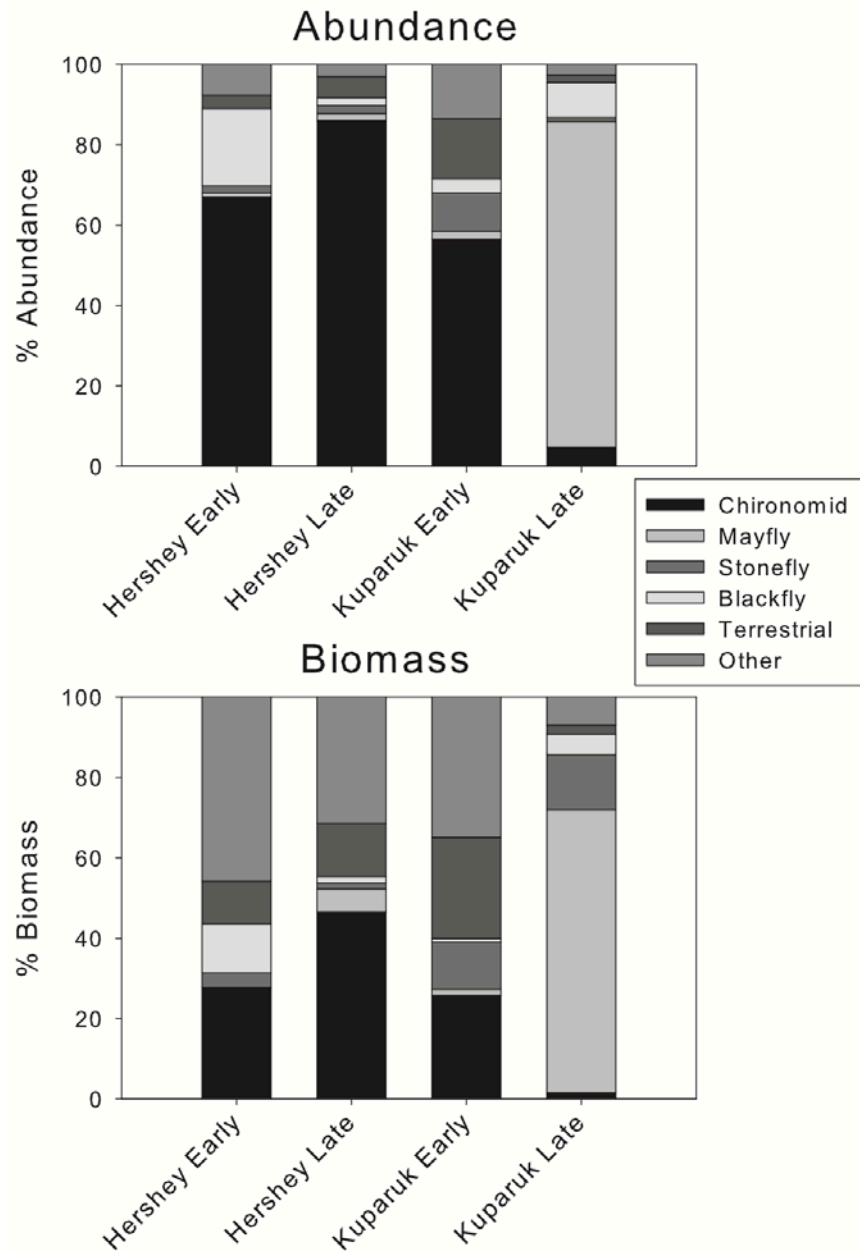


Fig. 7.21. Diets of Arctic grayling in Hershey Creek (n = 58 fish) and the Kuparuk River (n = 51 fish) from 1999-2001. “Early” refers to late June-early July while “late” refers to early August. Abundance is based on number of prey; biomass is based on weight of prey. Stomach contents were obtained by gastric lavage and all insects from the contents were identified. Data from unpublished manuscript of C. MacKenzie and L. Deegan.

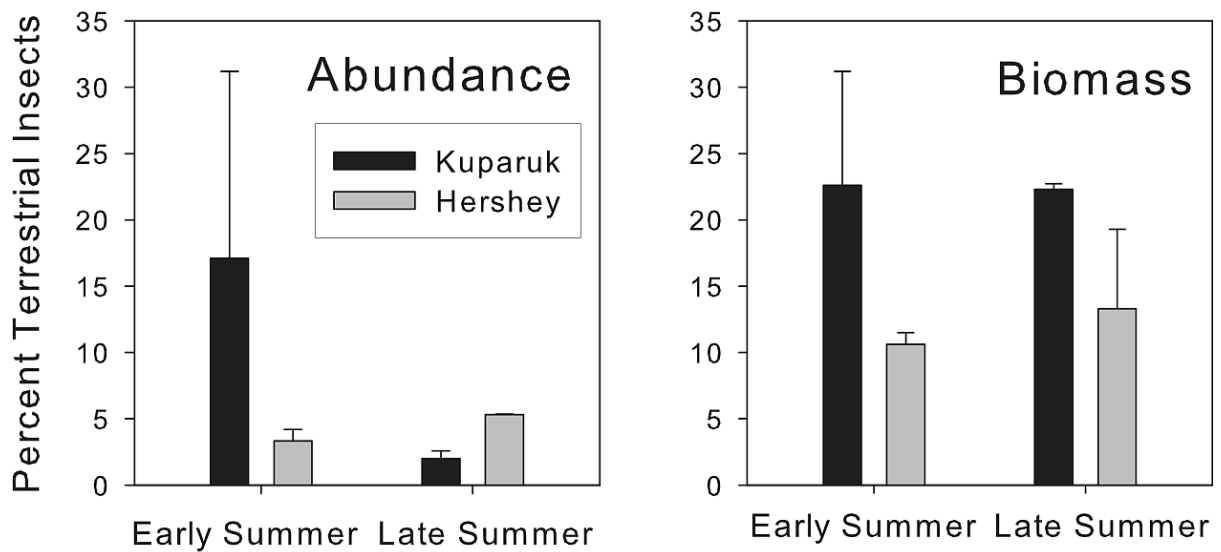


Fig. 7.22. Contribution of terrestrial insects to diets of Arctic grayling in small streams and large rivers. Means values are from the same fish described in Fig. 7.21. The total number of fish represented in each category of this figure across all three seasons are Hershey early $n = 21$, Hershey late $n = 37$, Kuparuk early $n = 24$, and Kuparuk late $n = 27$. There are no data for Kuparuk early fish in 1999.

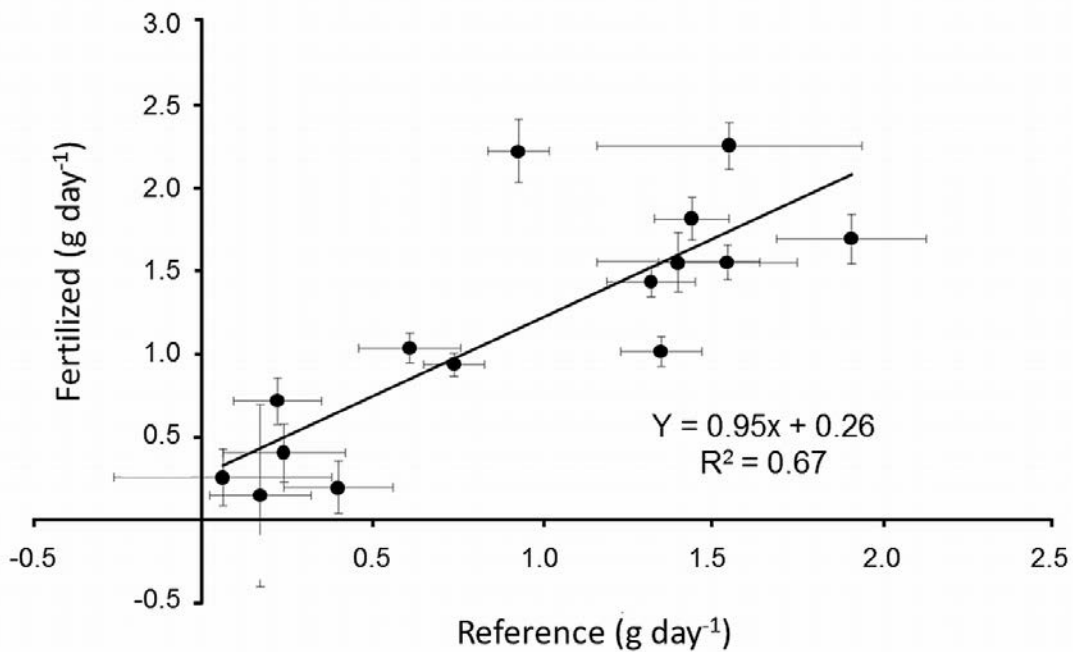


Fig. 7.23. Growth rate of adult arctic grayling in reference and phosphorus enriched reaches of the Kuparuk River between 1986 and 2004. The solid line is the regression between reference and fertilized reaches.

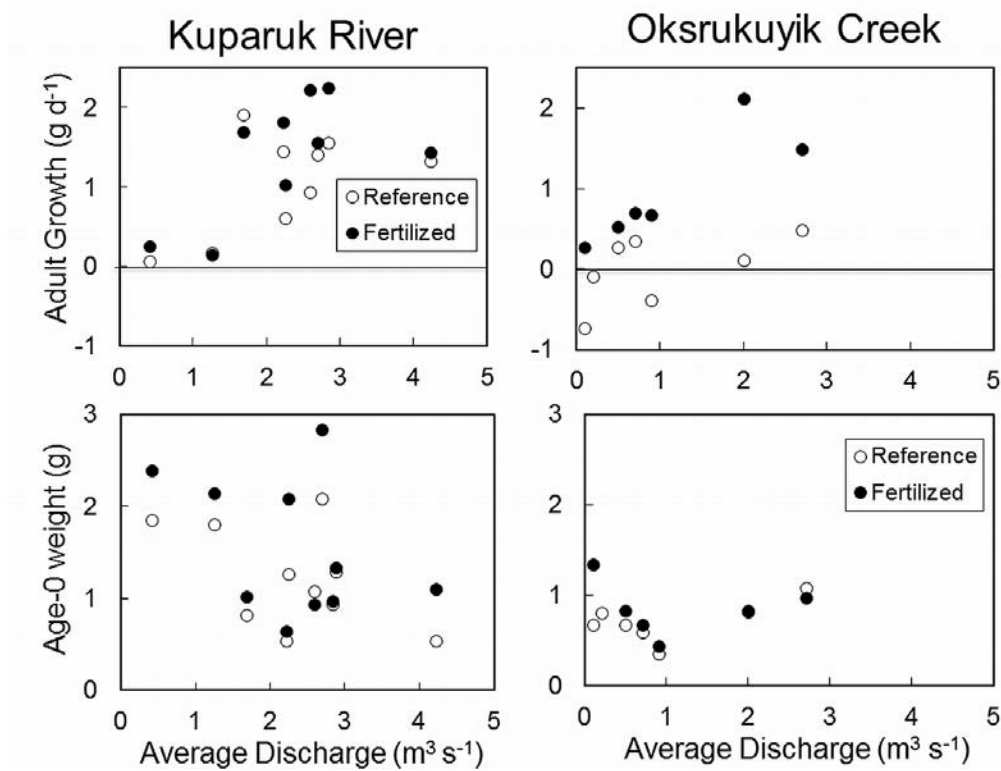


Fig. 7.24. Relationship between growth of adult and young-of-the-year (age 0) grayling and river discharge in the Kuparuk River and Oksrukuyik Creek. From Deegan et al. (1999) with permission from the American Fisheries Society.

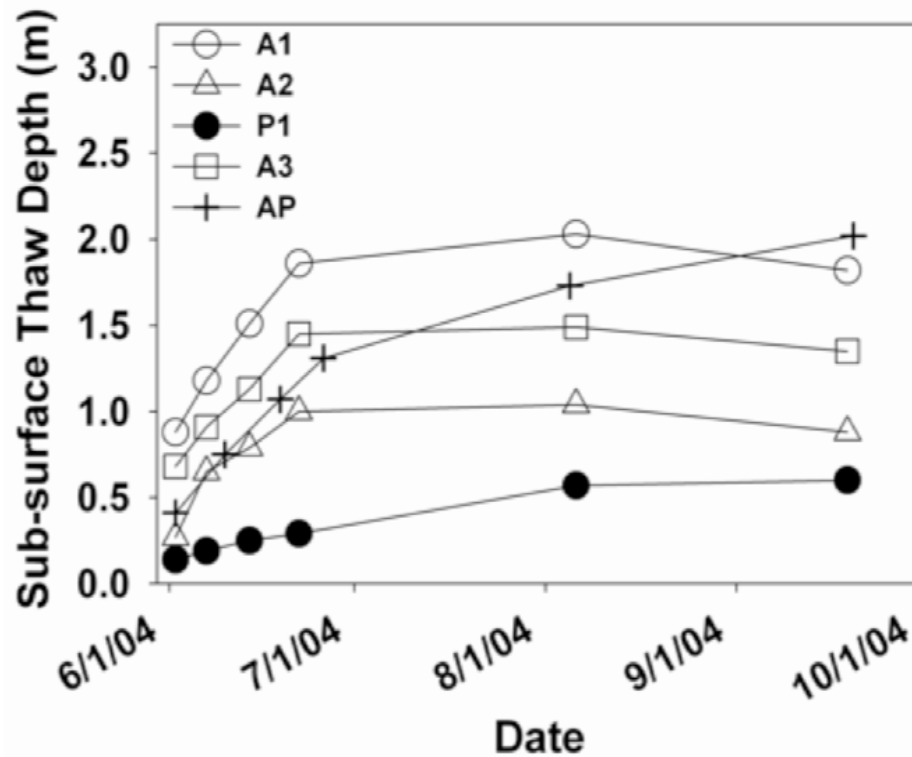


Fig. 7.25. Sub-surface thaw depth determined by ground penetrating radar data for fast-flowing cobble-bottom streams (A1, A2, A3, AP) and one slow-moving, peat-bottomed stream (P). From Zarnetske et al. (2007) with permission from the American Geophysical Union.

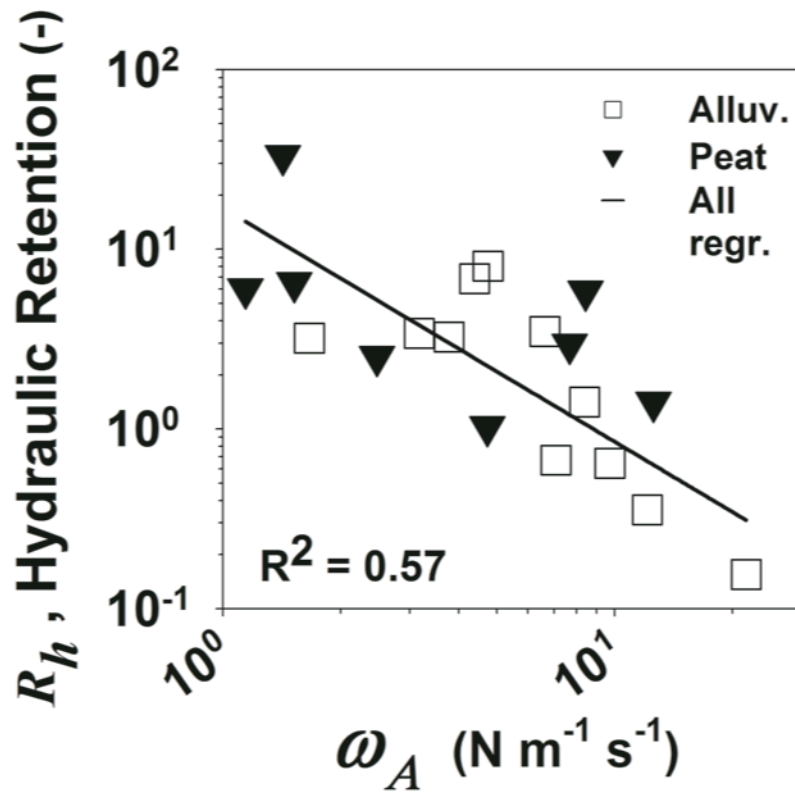


Fig. 7.26. Relationship between hydraulic retention, representing the time spent in storage per meter length of stream, and stream power (x-axis), as determined by numerous conservative solute tracer experiments in arctic streams (Zarnetske et al. 2007, with permission from the American Geophysical Union).

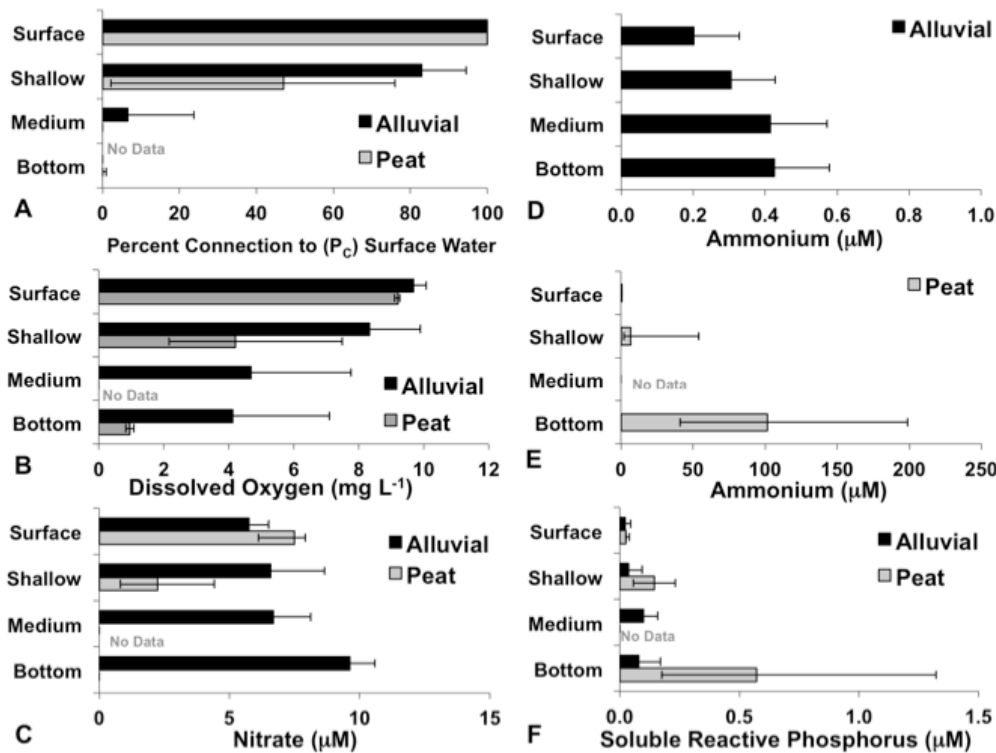


Fig. 7.27. Characteristics of surface waters and hyporheic waters from mini-piezometers installed at three depths in an alluvial stream and two depths in a peat stream, as determined from conservative tracer addition experiments. Note that “Bottom” in the alluvial stream is much deeper (110 cm) than “Bottom” in the peat stream (33 cm). (A) Median percent connectedness (P_c) of hyporheic waters to surface water at the same location. (B) Median dissolved oxygen concentrations. (C) Median nitrate concentrations. (D) and (E) Median ammonium concentrations. Note the change in scale between the alluvial (D) and peat (E) sites. (F) Median phosphate concentrations. From Greenwald et al. (2008) with permission from the American Geophysical Union.

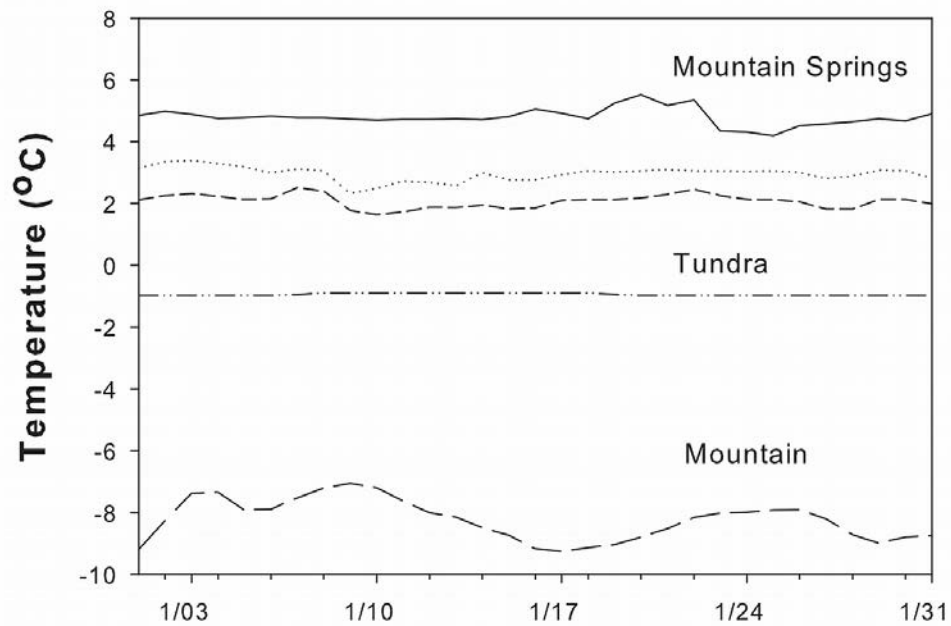


Fig. 7.28. Midwinter (January) temperatures in different types of arctic streams, from Parker (2008).

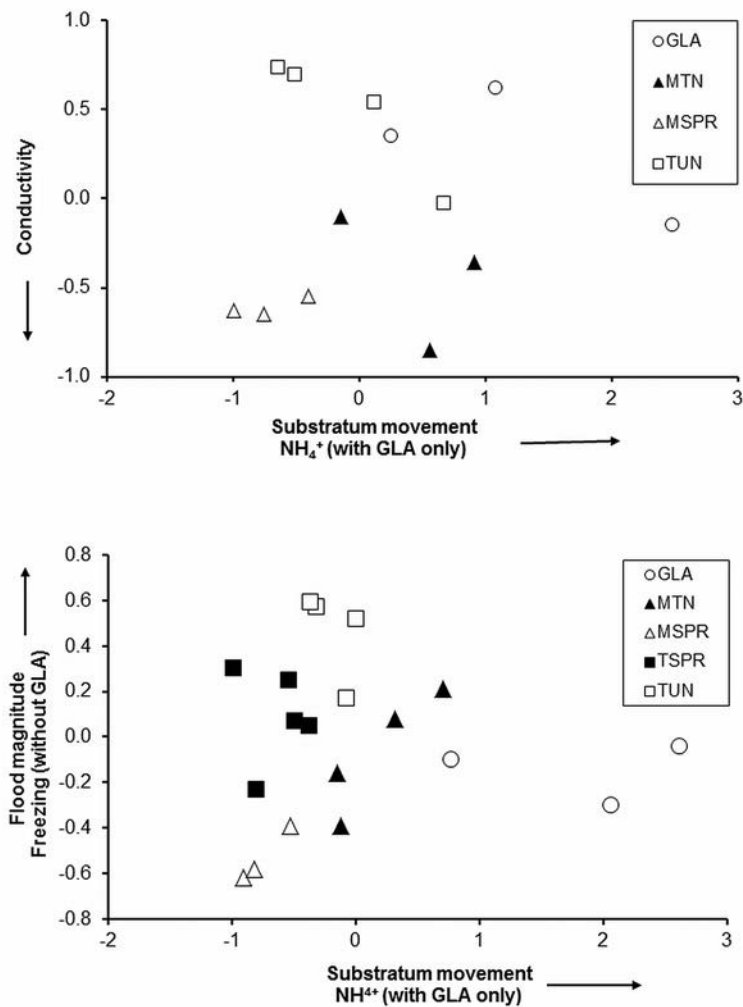


Fig. 7.29. (A) Multidimensional scaling (MDS) analysis based on periphyton biovolume in 17 streams (2D Stress = 0.12). (B) MDS analysis based on invertebrate biomass (2D Stress = 0.08). GLA = glacier stream, MTN = mountain stream, MSPR = mountain spring, TSPR = tundra spring, TUN = tundra stream. From Parker and Huryn (2011) with permission from Freshwater Biology.

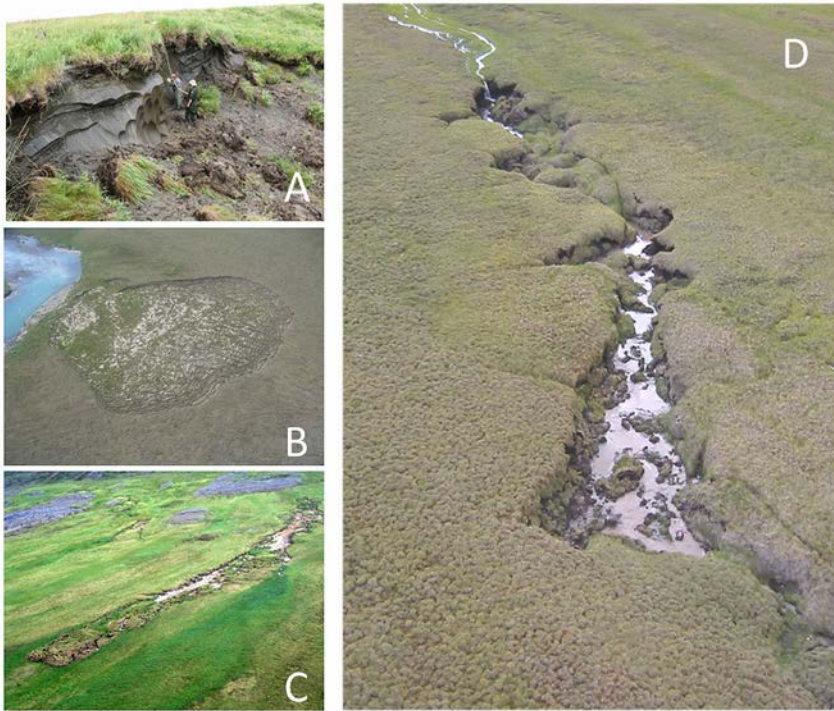


Fig. 7.30. Examples of hillslope failures induced by thermokarst terrain. (A) glacial thermokarst, note the exposed massive ice and people for scale. (B) retrogressive thaw slump, widest dimension is about 100 m. (C) an active layer detachments slide, length is about 800 m. (D) gully thermokarst, length is about 150m. Photo credits W. B. Bowden except (C) by M. Gooseff (reproduced with permission from the American Geophysical Union).

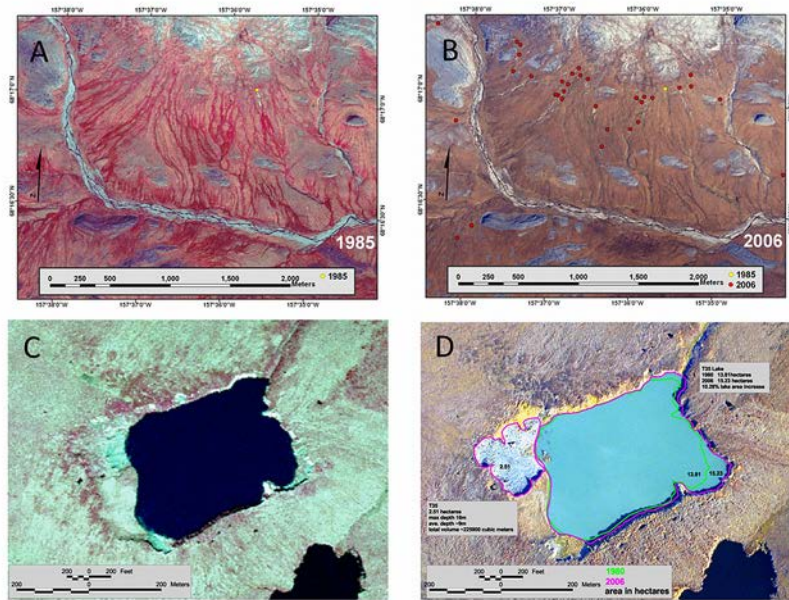


Fig. 7.31. Thermokarst distribution near Feniak Lake: Changes in the past 25 years (A) 1985 Alaska High-Altitude Photography (AHAP) photo (color-infrared) showing 1 active thermokarst feature in 1985 (green dot) and 27 active thermokarst features in 2006 (yellow dots, see panel B). Note the dark red strips of riparian vegetation (mainly *Salix* spp.) along water tracks in this image. (B) 2006 aerial photo (real-color) showing the same location and features as in panel A. (C) 1980 AHAP photo of lake in process of expansion. (D) 2006 air photo with graphics showing 26 years of substantial change (1980-2006). From Gooseff et al. (2009) with permission from the American Geophysical Union.



Fig. 7.32. Toolik River looking north on 28 July 2003. Flow is toward top of the picture. The thermokarst is just off of the image to the left, on the small drainage that can be seen joining the Toolik River at the center right of the image. The change in brightness in the upper (impacted reach of the Toolik River) is due to sediment input from the small tributary. On this date the sediment impact could be seen from the air at least 20 km downstream. For scale, the main river at this point is about 5-10 m wide. Photo credit: W.B. Bowden.

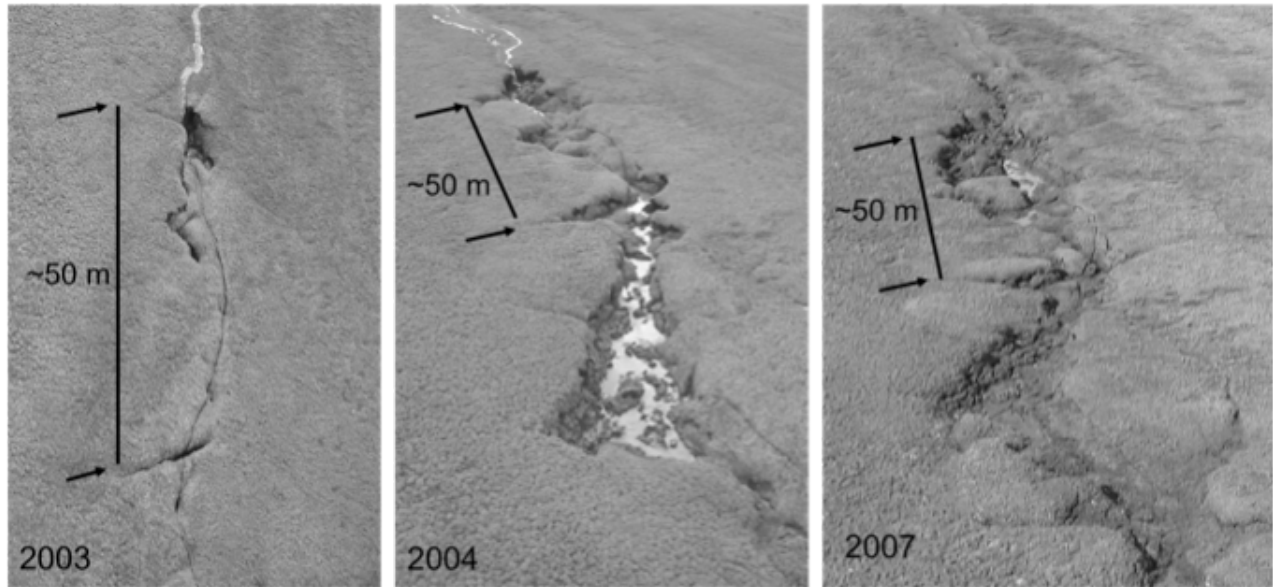


Fig. 7.33. Images of the gully thermokarst on a tributary near the headwaters of the Toolik River shortly after it formed in 2003 and in 2004 and 2007. Note how the feature grows rapidly from 2003 to 2004 and how the edge features collapse and “soften” between 2004 and 2007. From Bowden et al. (2008) with permission from the American Geophysical Union.

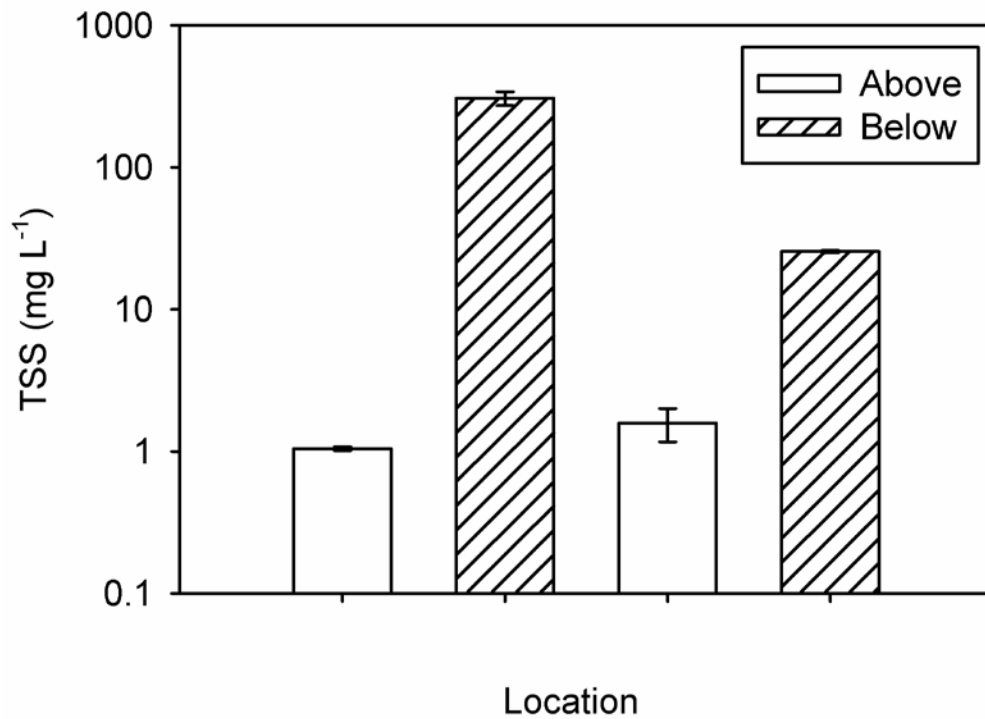


Fig. 7.34. Total suspended sediment concentrations in the small drainage above and below the thermokarst near the Toolik River and above and below the point that this drainage entered the Toolik River. Note the log scale on the TSS concentration axis. The reported values are means and range of values for $n = 3$ thermokarst samples and $n = 2$ junction samples. From Bowden et al. (2008) with permission from the American Geophysical Union.

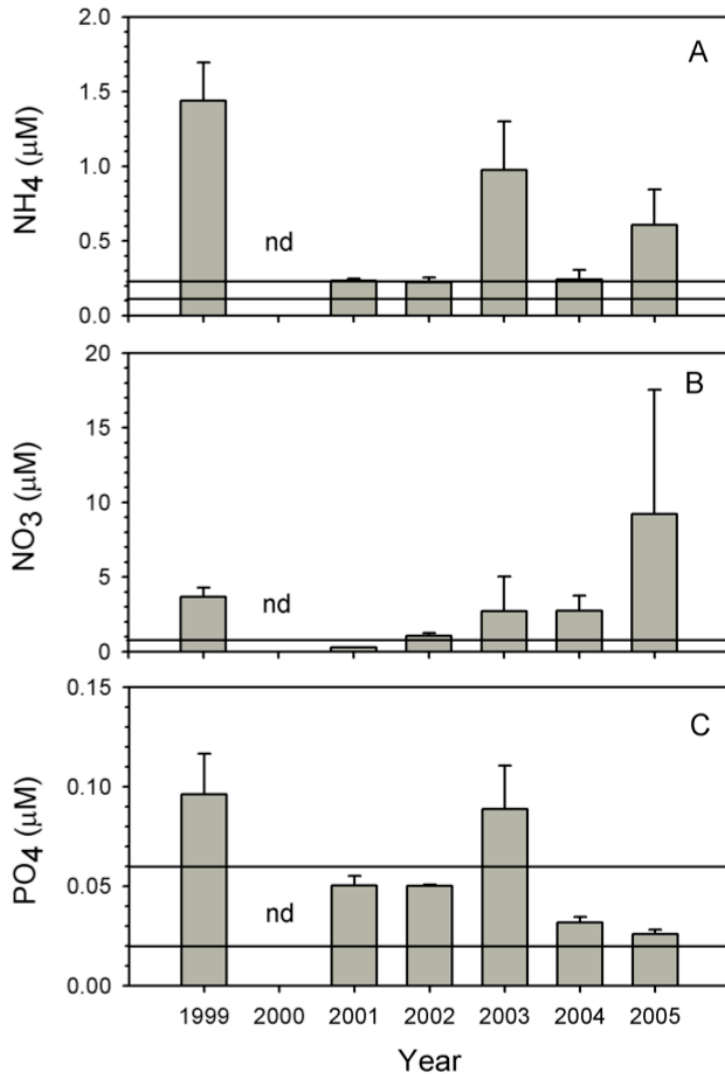


Fig. 7.35. Concentrations of (A) ammonium, (B) nitrate, and (C) phosphate within the stream reaches most impacted by the thermokarst on Imnavait Creek. The bars are the mean values for the stations between 25 m and 350 m, by year. No samples were collected in 2000 (nd). The horizontal lines indicate the 95% confidence intervals for the mean reference values measured in Imnavait Creek. The 95% confidence interval for reference nitrate values included zero so there is only one (upper) boundary line. The error bars are ± 1 SE for $n = 7$ except for 2003, 2005 ($n = 5$), and 2004 ($n = 4$). From Bowden et al. (2008) with permission from the American Geophysical Union.

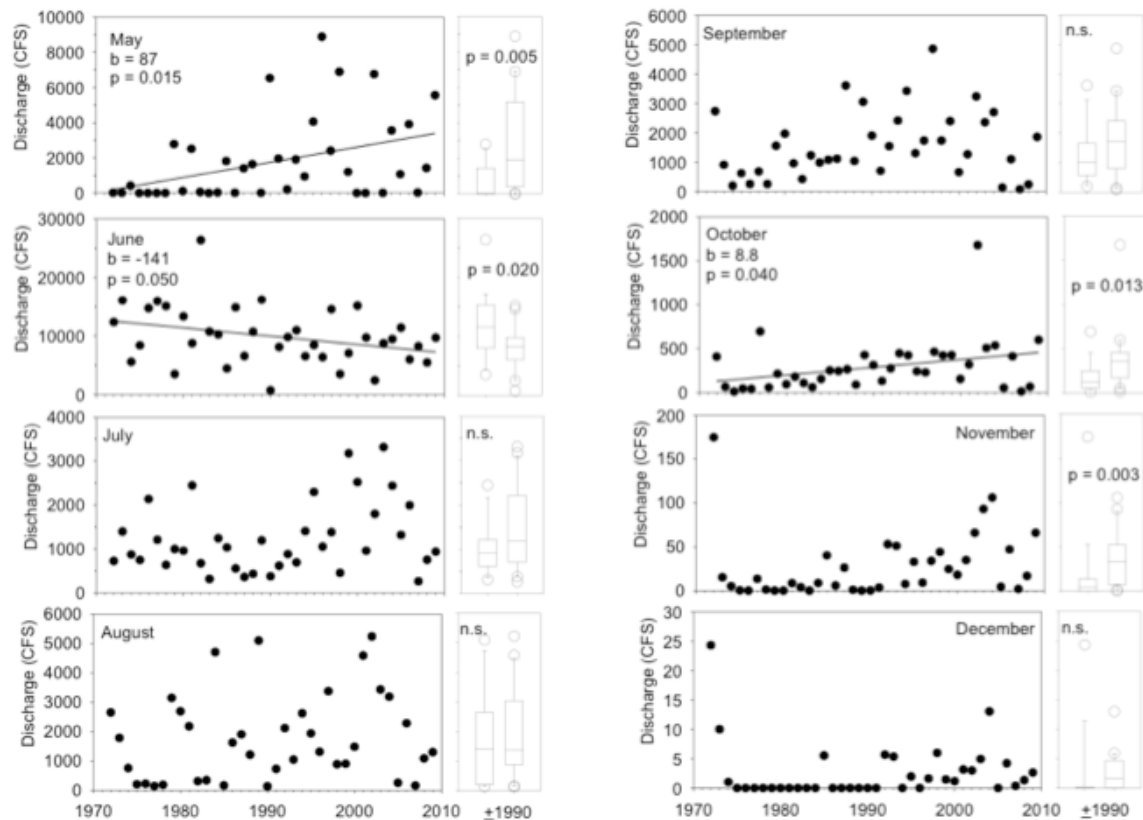


Fig. 7.36. Mean monthly discharge from the USGS gauge (15896000) at the mouth of the Kuparuk River from 1972 to 2010. Significant trends are indicated with a regression line and statistics in the left panel of each monthly pair. The right panel of each pair shows a box and whisker comparison of discharges between the early period of the record (1972-1989) and the late period of the record (1990-2010).

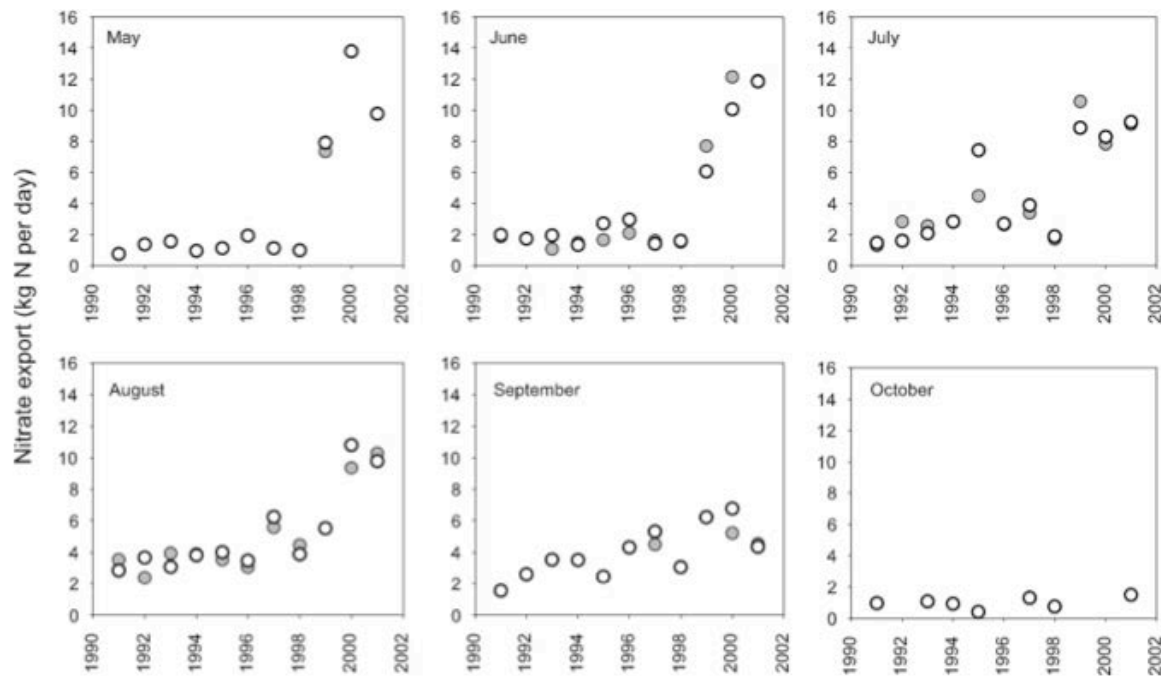


Fig. 7.37. Nitrate export estimates in the upper Kupaaruk River calculated using measured (filled circles) and simulated (open circles) river discharge to drive LOADEST from 1991-2001. Export estimates calculated using measured discharge are largely constrained to June, July, and August because of insufficient discharge data, whereas coupling of LOADEST with simulated discharge allows estimation of export over the complete flow period. From McClelland et al. (2007) with permission from the American Geophysical Union.

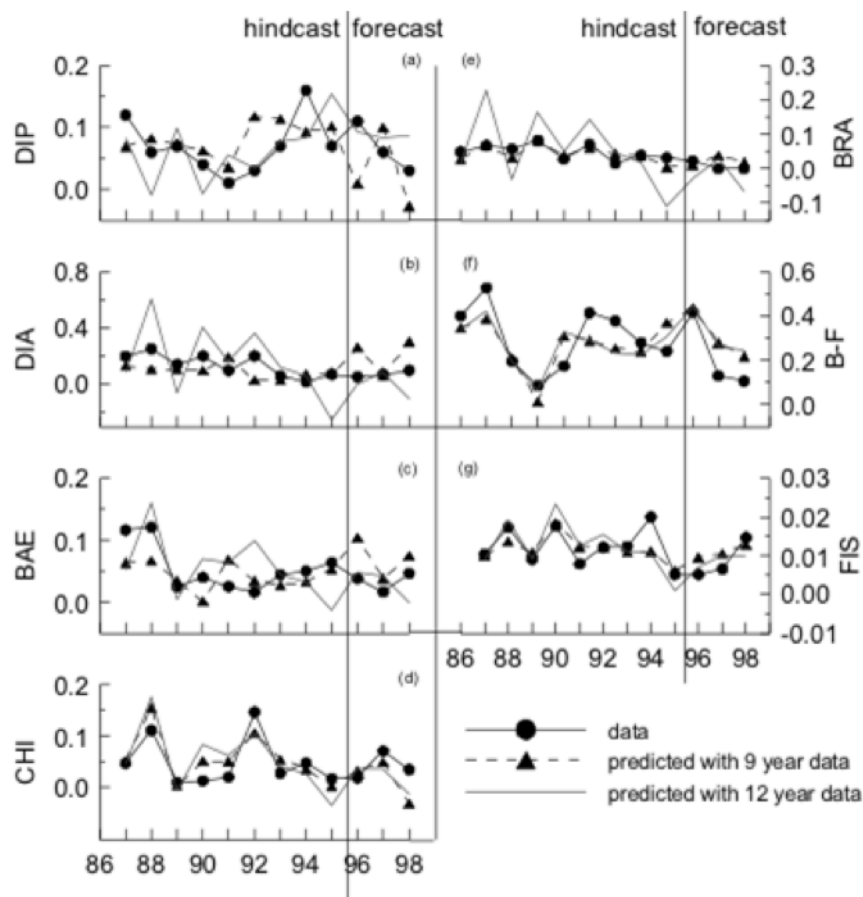


Fig. 7.38. Interactions of arctic communities and biogeochemical cycles with global climate change.

Chapter 7 Vignette Figure Legends

Fig. 7.V1. Inverse model calibration, testing, and predictions.
Comparison of model predictions (filled triangles) with observations (filled circles) in the Kuparuk River reference reach in which only the first nine years of data were used in model fit and the last three years are model forecasts. Solid line is the model result from a run calibrated using all data in a hindcast mode. Units are in mmol P m^{-2} . DIP = dissolved inorganic P, DIA = epilithic diatoms, BAE = *Baetis*, CHI =

chironomids, BRA = *Brachycentrus*, B-F = black flies, and FIS = fish. From Wan et al. (2008) with permission from Ecological Modeling.

Fig. 7.V2. Climate drivers during the period 1990-1999 and forecast for the period 2090-2100 according to an inverse linear model (Wan et al. 2008, with permission from Ecological Modeling).

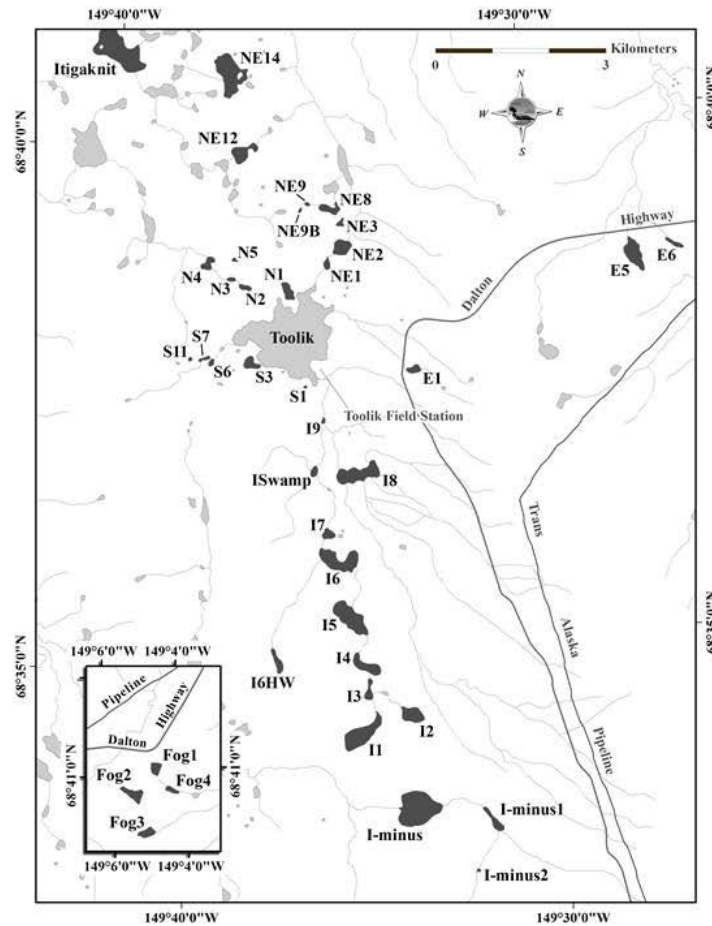


Fig. 8.1. Map of the lakes commonly sampled in the Arctic LTER program. Lakes listed in Table 8.2 that are used for comparisons of effects of lake size and glacial history are shown. Lakes in the insert at the lower left (Fog1-4) are located about 20 km east of Toolik Lake along the Dalton Highway.

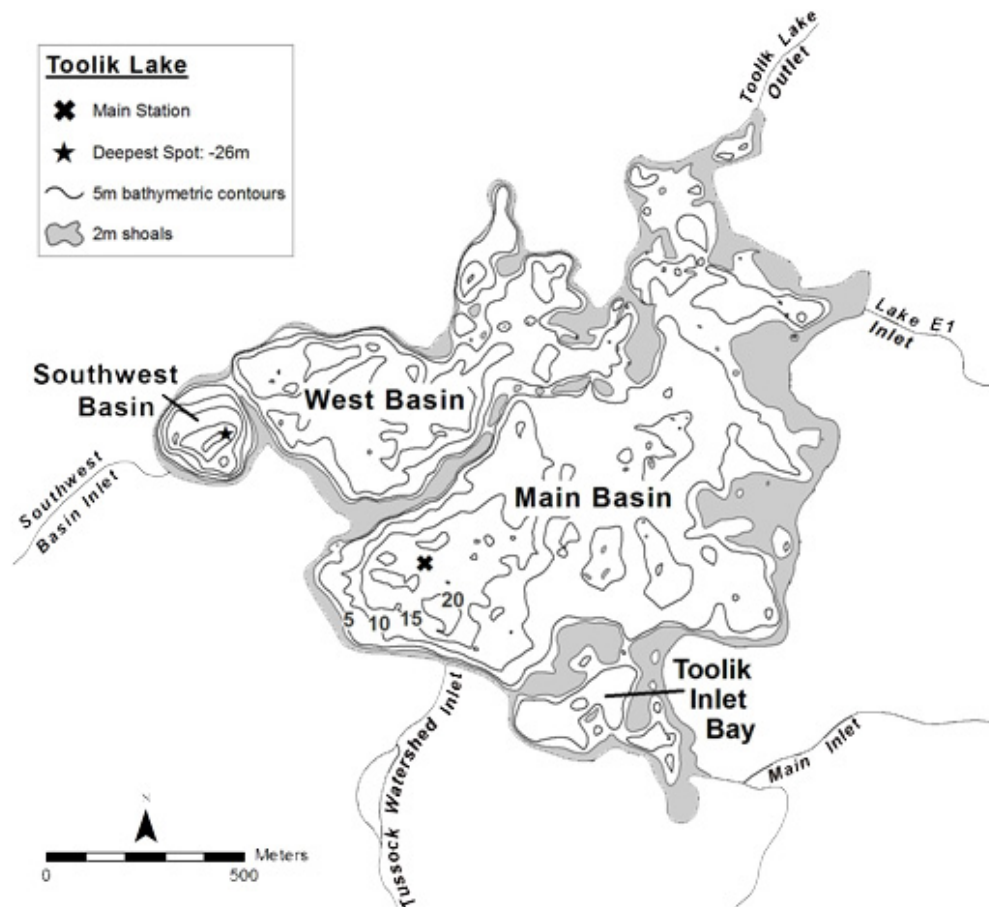


Fig. 8.2. The bathymetry of Toolik Lake is shown with 5 m depth contours. The gray regions depict shoals that separate different kettle basins. The main sampling station is shown with an X and the deepest location with a star. The four dominant inlet streams and one major outlet stream are shown.

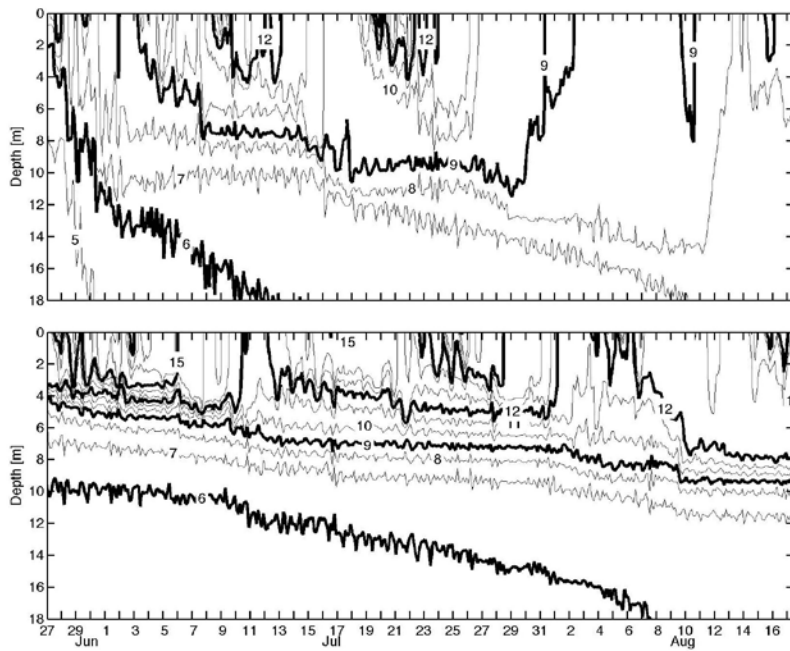


Fig. 8.3. Thermal stratification of Toolik Lake during the cool summer of 2003 (top) and the warm summer of 2004 (bottom).

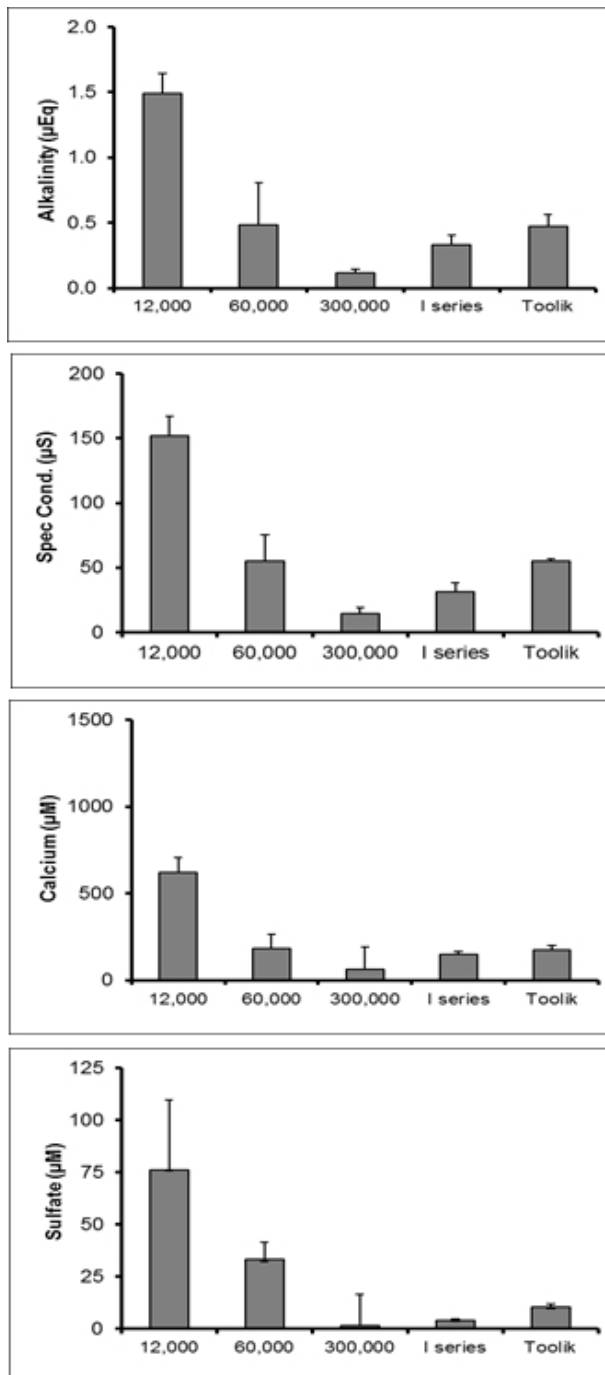


Fig. 8.4. Mean (+ SD) of specific conductivity ($\mu\text{S cm}^{-1}$), alkalinity ($\mu\text{Eq L}^{-1}$), and concentrations of calcium and sulfate (μM) in surface waters of lakes near the Toolik. Numbers on the X-axis represent years before present of last glaciation. I-series and Toolik Lake have watersheds of mixed glacial ages as indicated in Table 8.1.

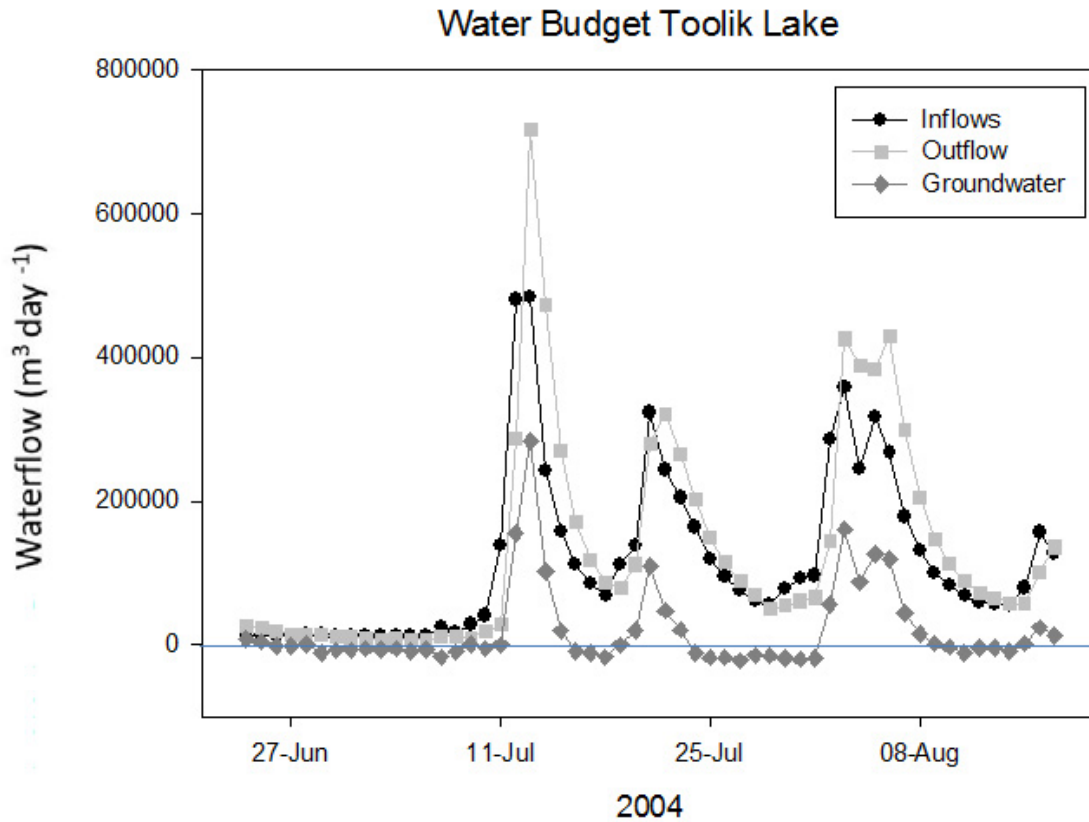


Fig. 8.5. Water budget for Toolik Lake during the summer of 2004.

Inflows include rain and discharge from the inlets, outflow is the discharge through the outlet and evaporation, and groundwater flows are assumed to be the difference between inflow and outflow. Negative values apply to groundwater only and indicate loss from the lake (data from E. Graham, unpublished).

Toolik Lake Food Web

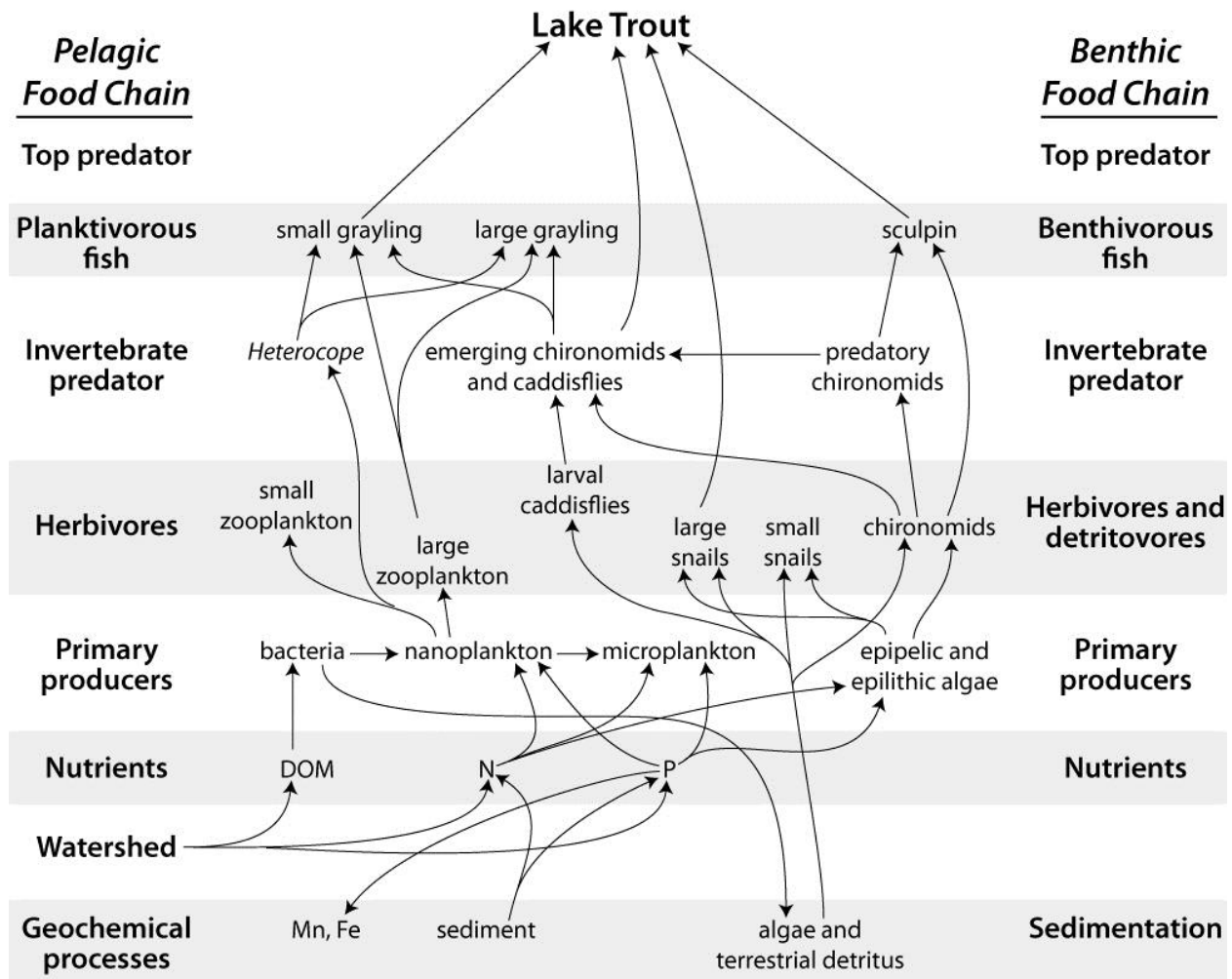


Fig. 8.6. Simplified food web for Toolik Lake as modified from O'Brien et al. (1997) with permission. Identification of pelagic and benthic aspects of trophic levels and associated processes are depicted on left and right sides of diagram respectively. Arrows indicate major pathways to material flow.

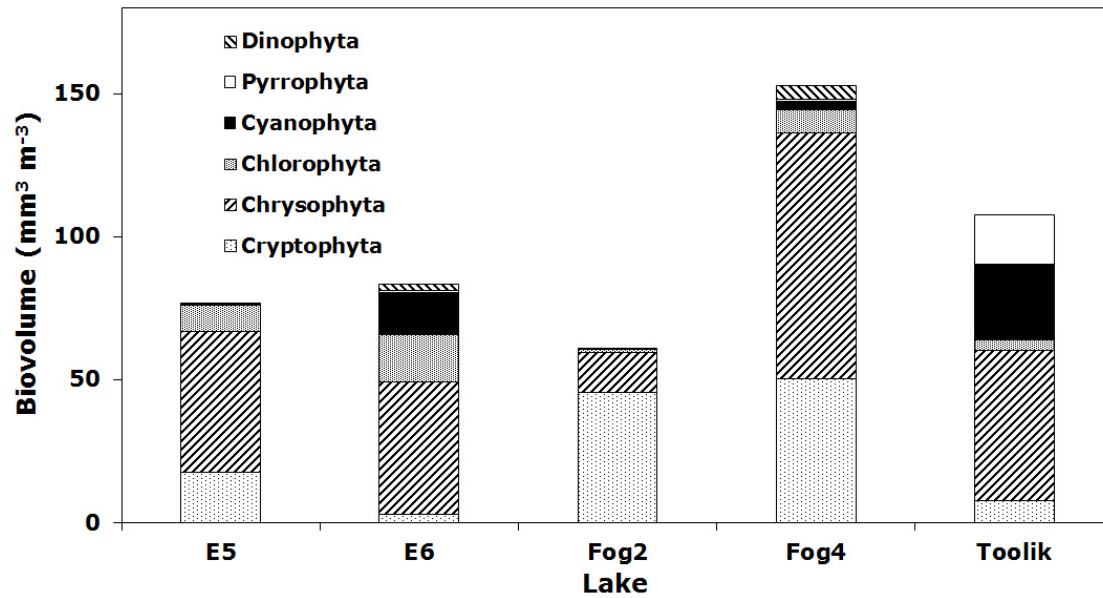


Fig. 8.7. Biovolume of major divisions of phytoplankton present in Lakes E5, E6, Fog2, and Fog4 on 11 July 2002, and in Toolik from August 1998. Lakes E6 and Fog4 are small, shallow lakes. Lakes E5, Fog2, and Toolik are deeper with maximum depths of 12, 20, and 23 m, respectively. Low level fertilization of lakes E5 and E6 began on July 1 of that year.

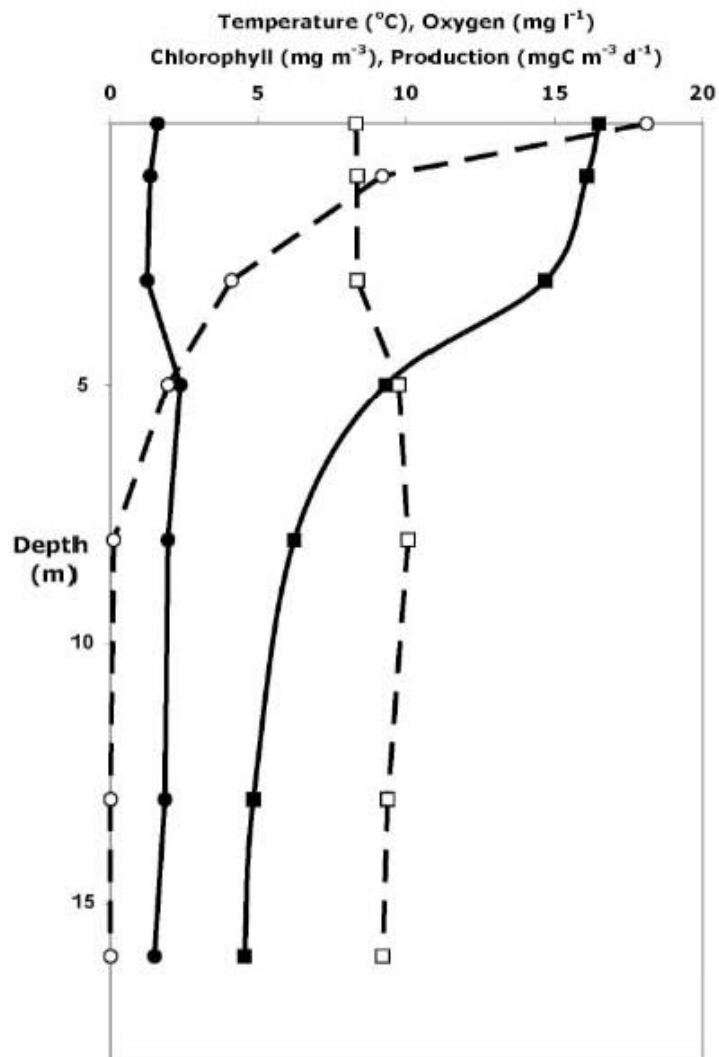


Fig. 8.8. Depth profile of temperature (solid squares and solid line), dissolved oxygen (open squares and dashed line), chlorophyll *a* (solid circles and solid line), and primary production (open circles and dashed line) for Toolik Lake on 9 July 1999.

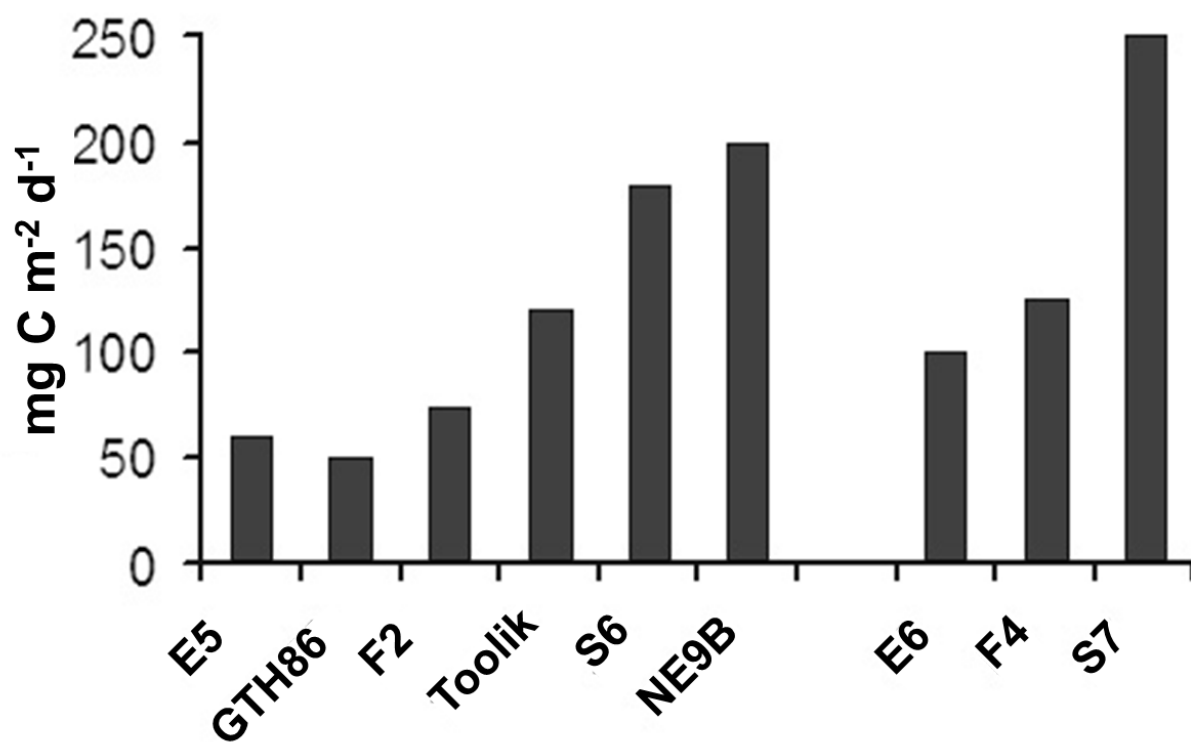


Fig. 8.9. Gross primary production (GPP) estimated from changes in oxygen concentration in light and dark benthic chambers placed at 3 m depth in lakes near Toolik.

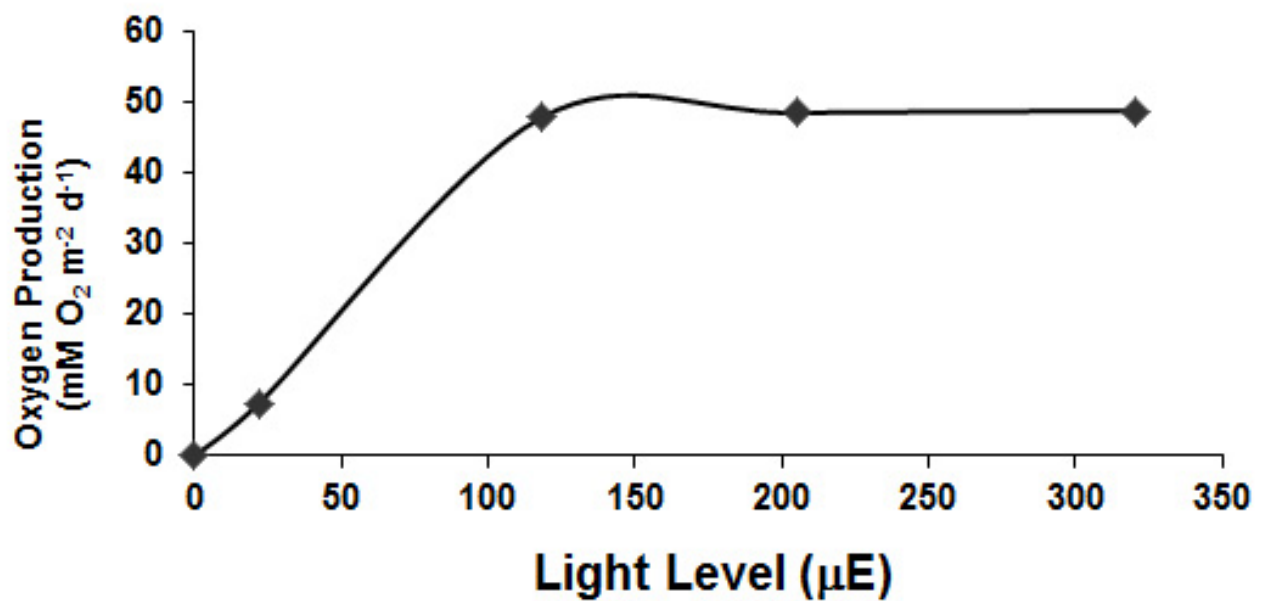


Fig. 8.10. Gross primary production estimated from oxygen production in sediment cores collected from Toolik Lake at 3 m depth and incubated under a range of light intensities ($\mu\text{E m}^{-2} \text{ s}^{-1}$) in the laboratory.

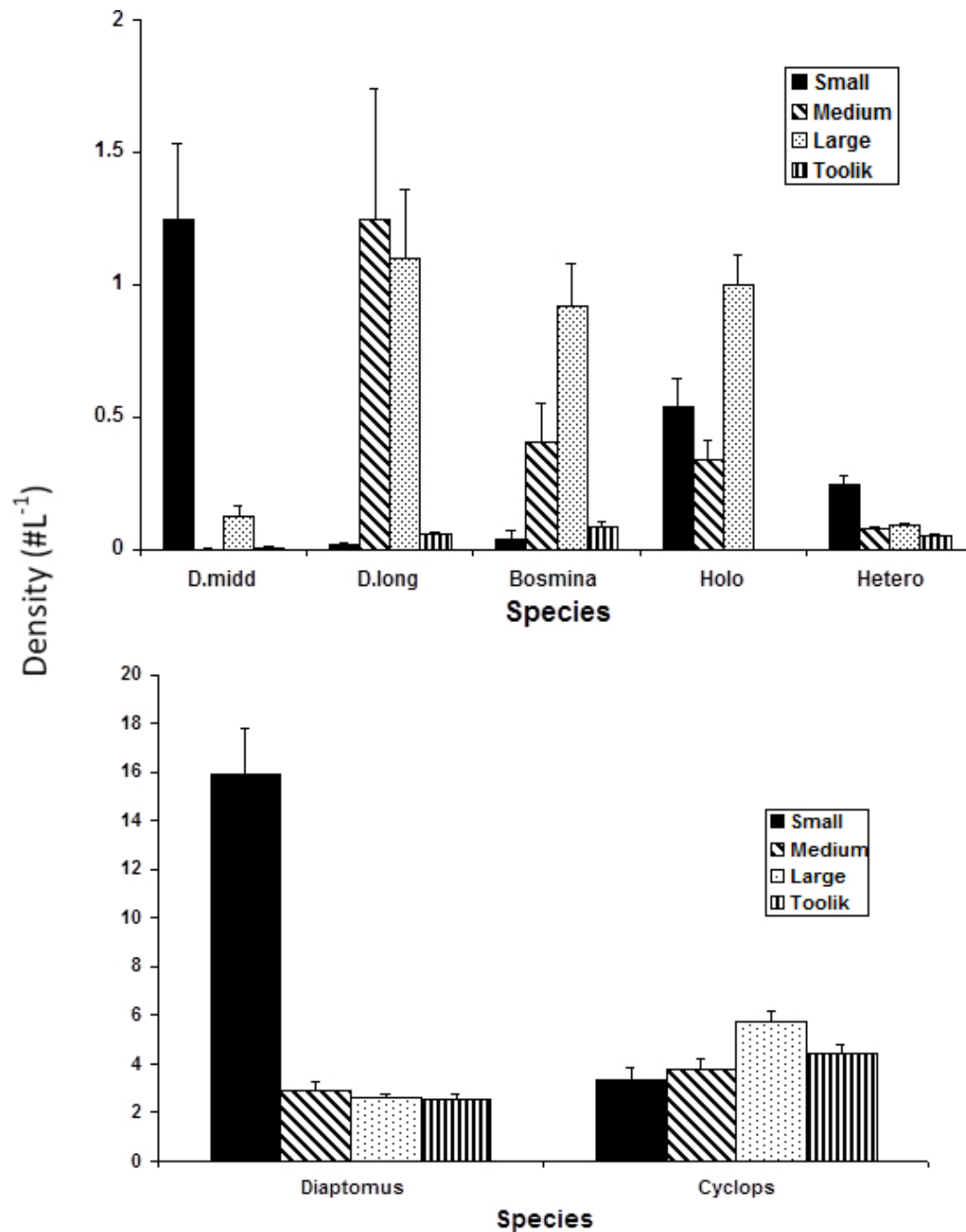


Fig. 8.11. Density of cladocerans (top) and copepods (bottom) in upper portion of the water column in small, medium, and large lakes compared to densities in Toolik Lake. Mean + SE for lakes listed in Table 8.1 for the years 2000-2005. D. midd is *Daphnia middendorffiana*, D. long is *Daphnia longeremis*, Holo is *Holopedium*, and Hetero is *Heterocope septentrionalis*.

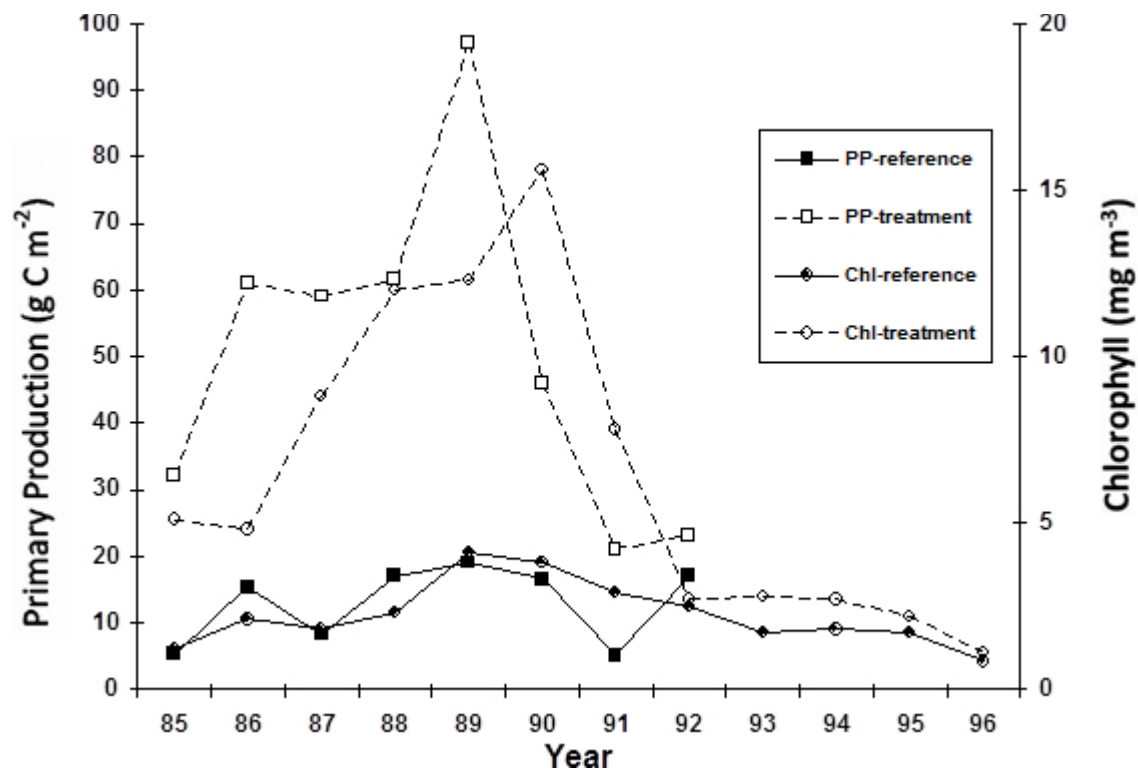


Fig. 8.12. Mean summer concentration of pelagic chlorophyll *a* (circles) and total summer primary productivity (squares) in Lake N2. Filled symbols represent the reference section of the lake; open symbols represent the treated section of the lake. The treated section of this lake was fertilized with dissolved nitrogen and dissolved phosphorus during the summers of 1985-1990. From O'Brien et al. (2005) with permission.

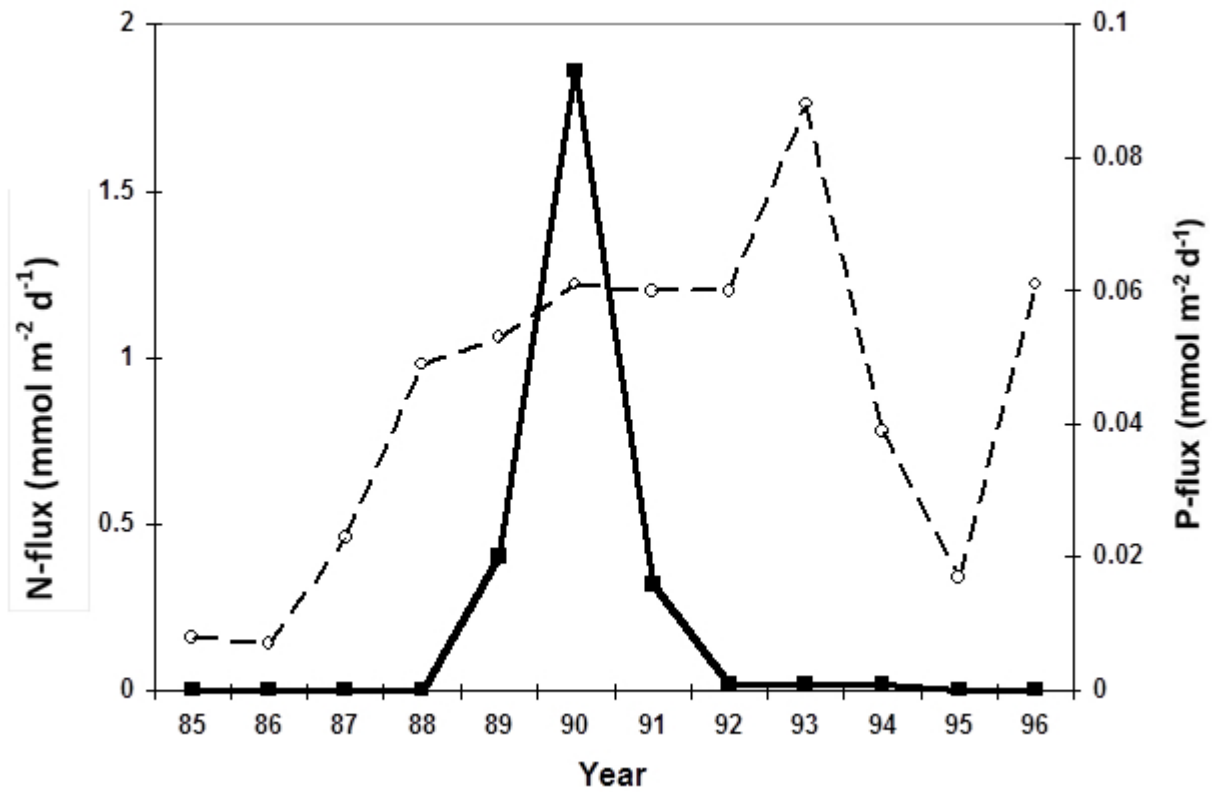


Fig. 8.13. The average daily fluxes of inorganic nitrogen (open circles) and phosphorus (solid squares) from the sediments of the fertilized sector of Lake N2. The treatment fertilization was conducted each summer during from 1985 through 1990.

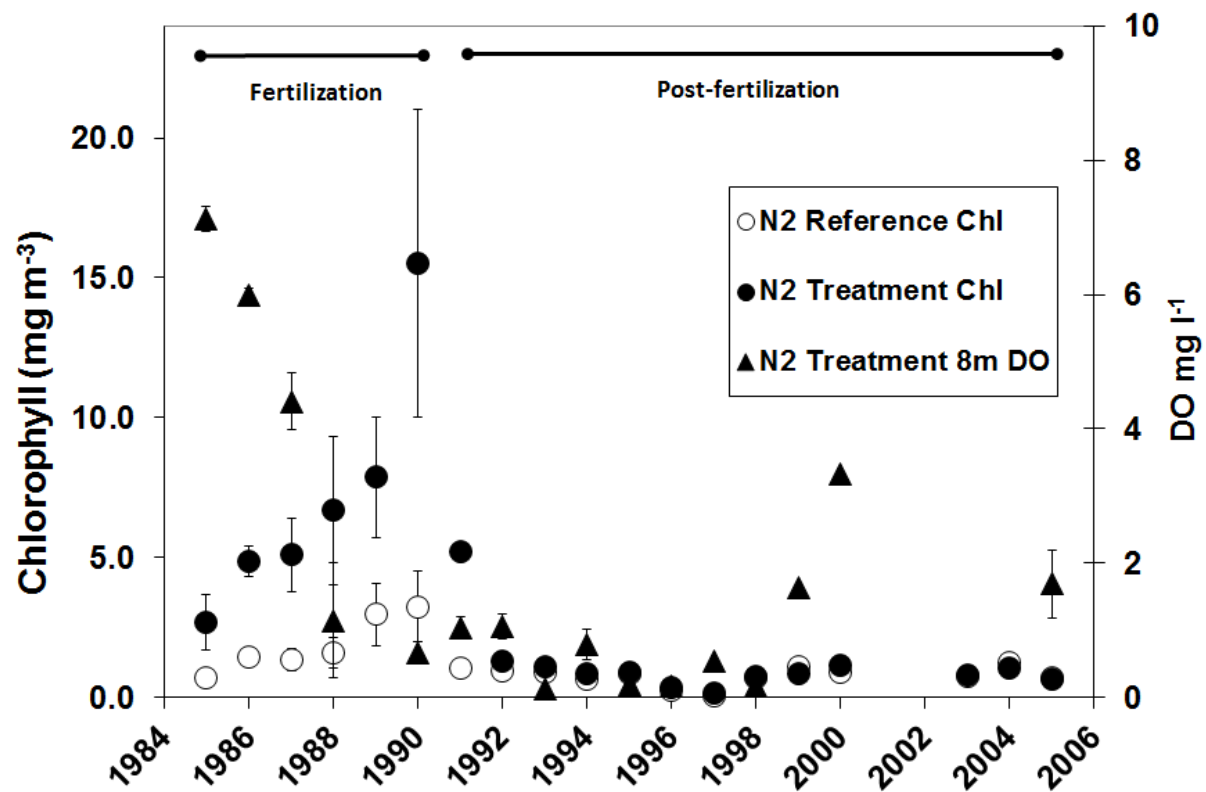


Fig. 8.14. Oxygen concentration near the bottom (8m) of the fertilized treatment in Lake N2 from 1985-2005 along with chlorophyll *a* concentrations in surface waters. Bottom-water oxygen concentrations in the reference side of Lake N2 remained high ($>6 \text{ mg O}_2 \text{ L}^{-1}$) during and after the fertilization.

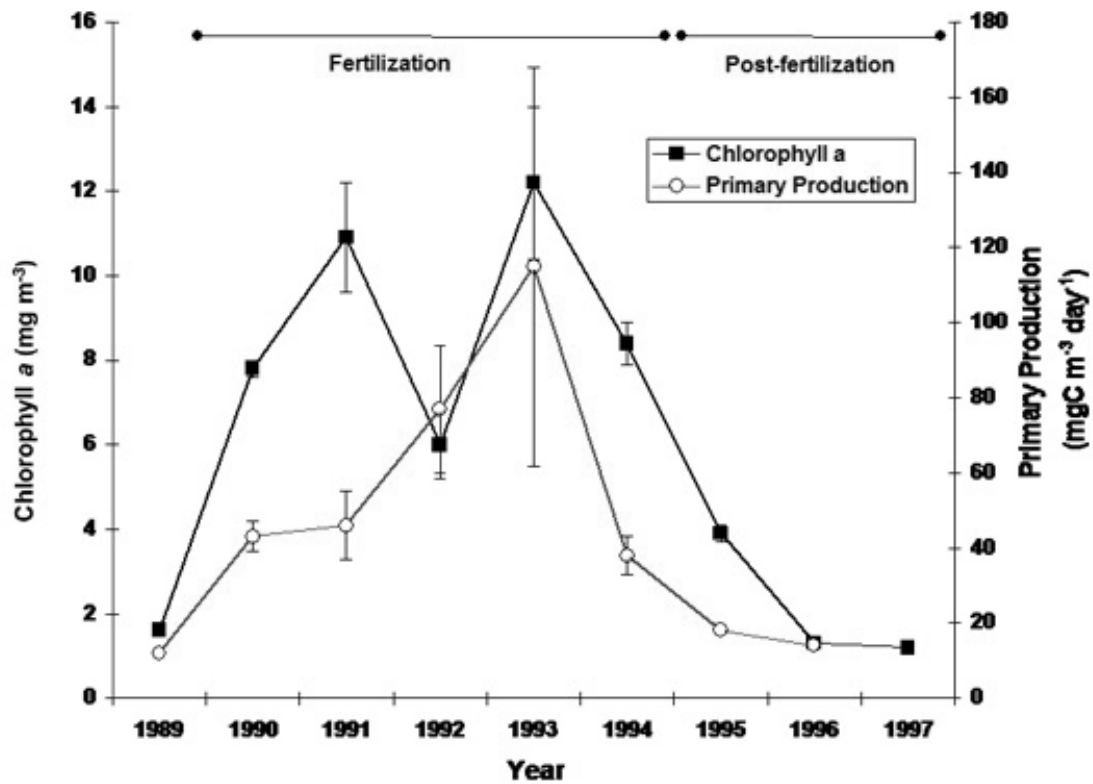


Fig. 8.15. Response of chlorophyll *a* and rates of primary production in the water column of Lake N1 to fertilization. Mean summer values + 1 SD are shown. Addition of phosphoric acid and ammonium nitrate occurred during summer months of 1990-1994. Redrawn from Lienesch et al. (2005) with permission of Springer Publishing Company.

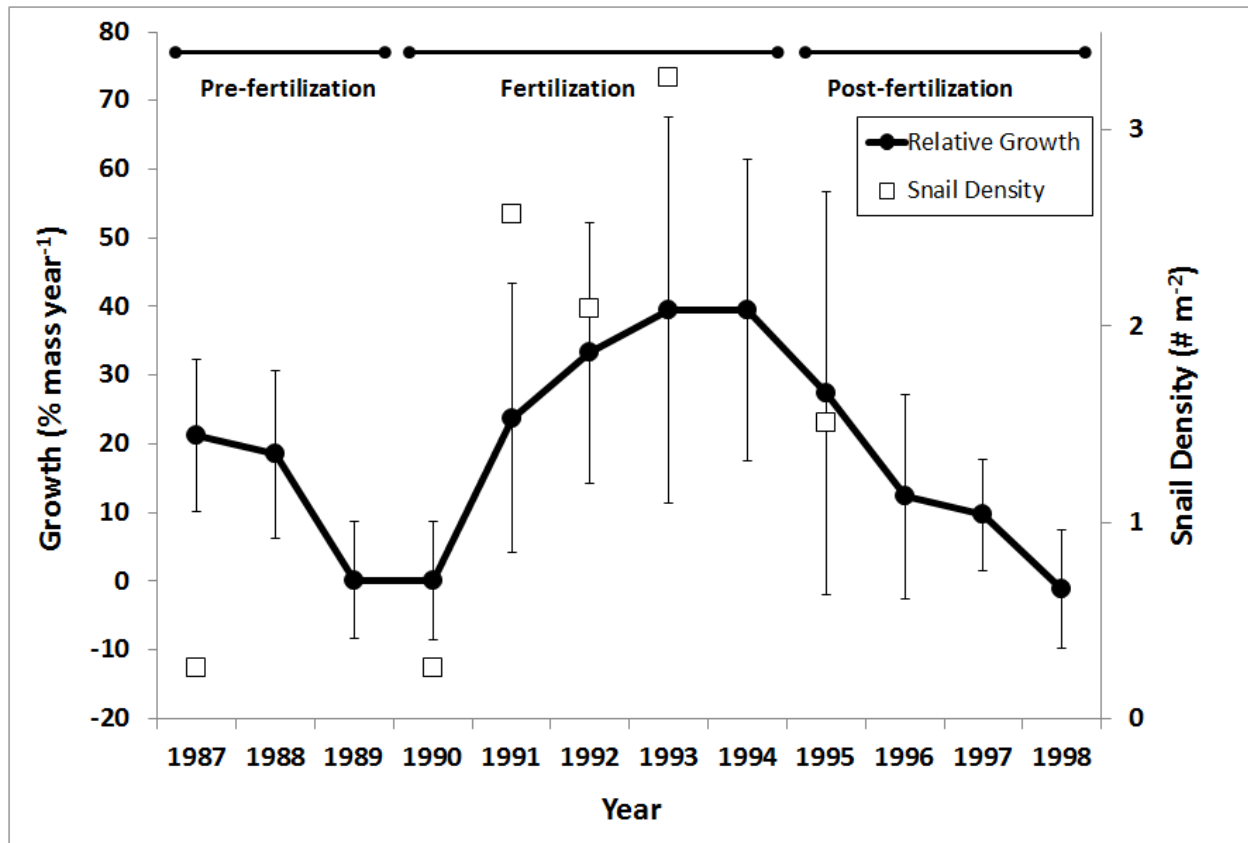


Fig. 8.16. Relative growth of individually tagged lake trout in Lake N1 before during and after fertilization (filled circles are mean values ± 1 SE). Open squares represent density of snails observed by divers. From Lienesch et al. (2005) with permission of Springer Publishing Company.

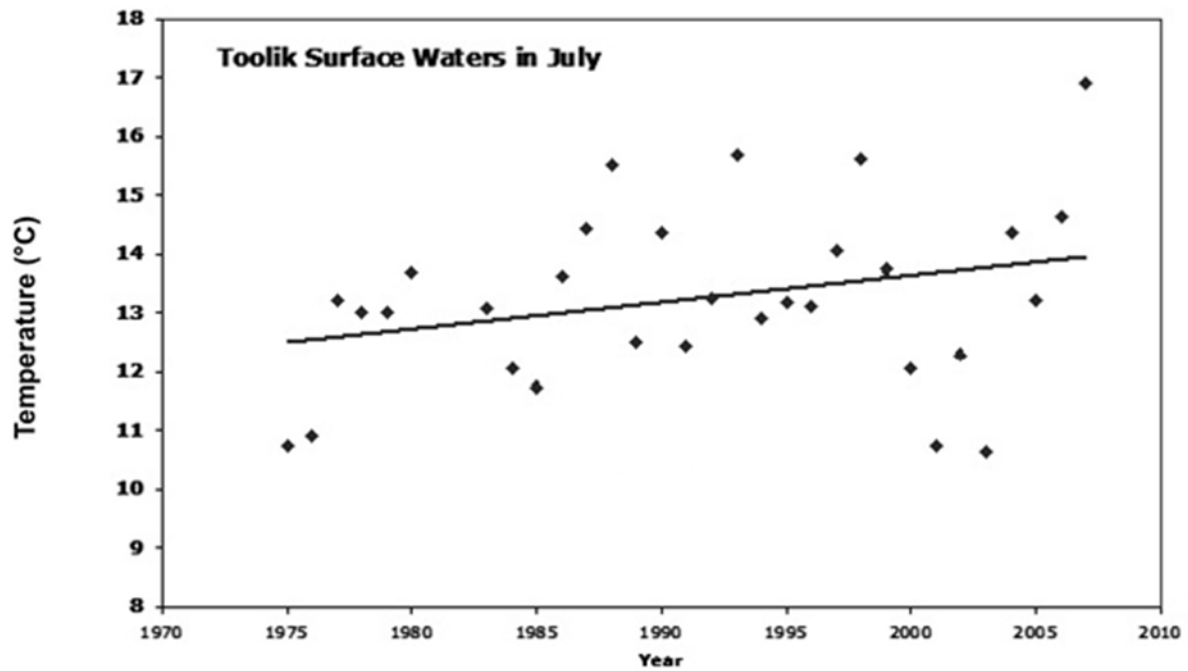


Fig. 8.17. Mean temperature in the epilimnion of Toolik Lake each July 1975-2007. The slope of the regression line ($y = 0.045x - 76$, $R^2 = 0.082$) is not statistically significantly different from zero.

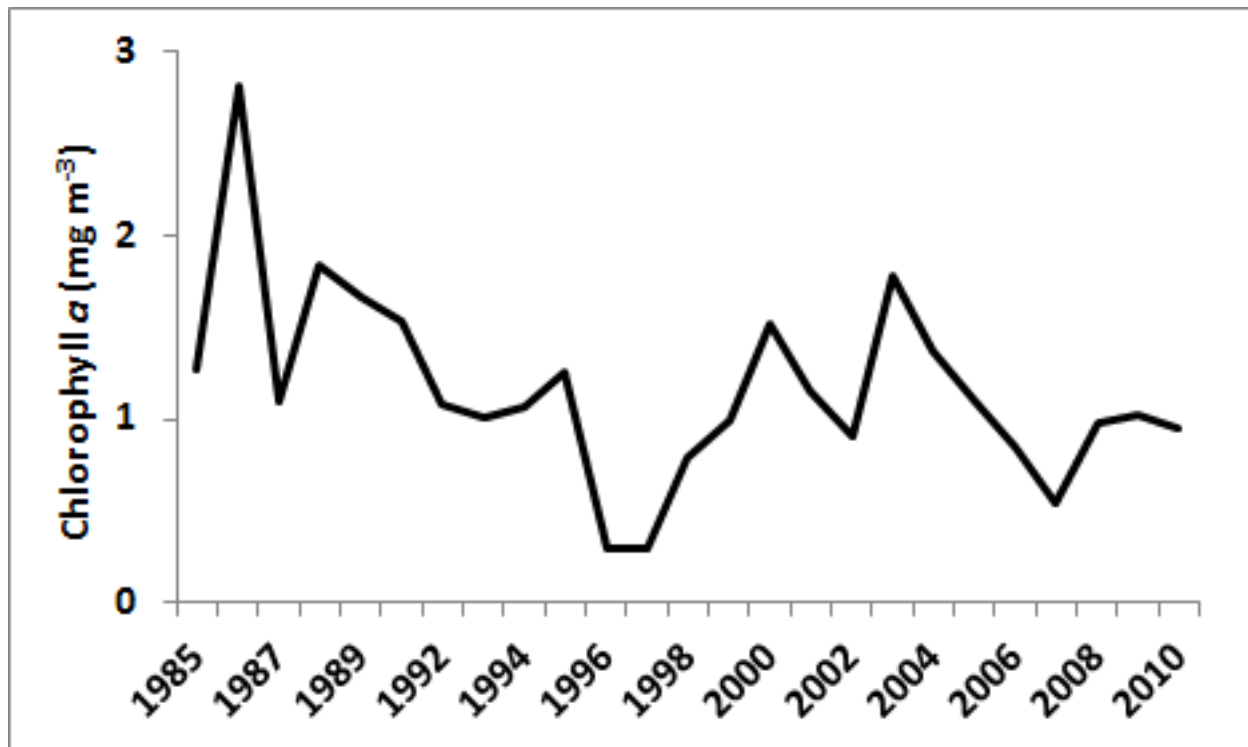


Fig 8.18. Concentration of chlorophyll *a* in the epilimnion (0-3 m) of Toolik Lake during July in years 1985-2010. No overall trend in this data series was present, but large inter-annual differences are apparent. Each data point represents the mean of 6 to 15 epilimnetic samples collected over the month.

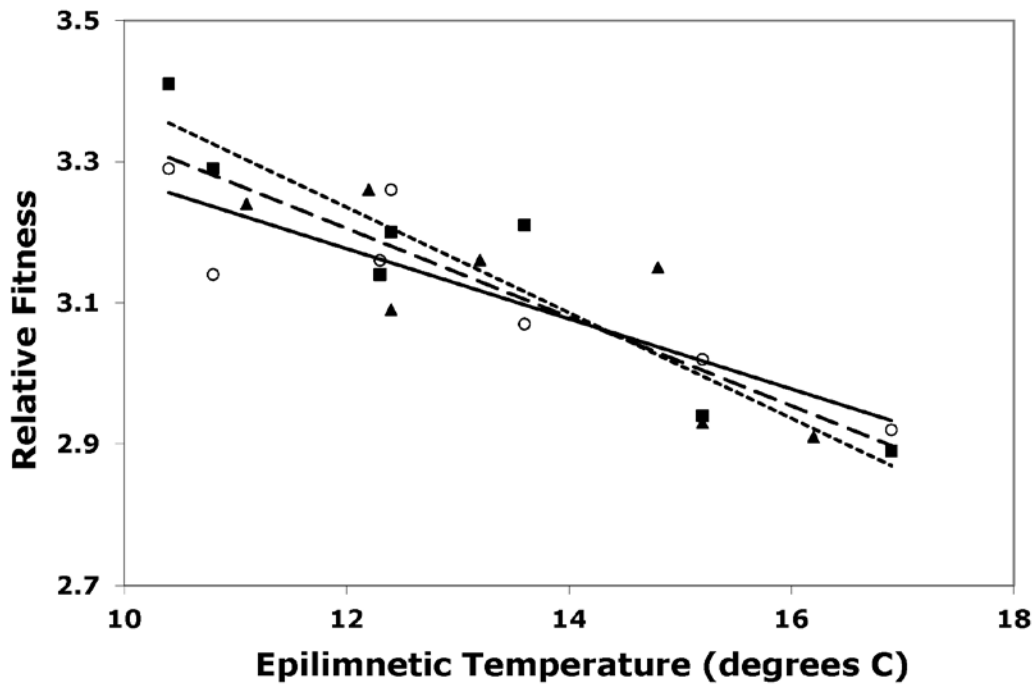


Fig. 8.19. Relative fitness of three species of fish versus epilimnetic temperatures (°C) in lakes NE12 (grayling and lake trout) and Lake Fog2 (char). Fitness is defined as the slope of the length-weight relationship. Closed squares represent lake trout, closed triangles represent arctic grayling, open circles represent arctic char. The regression of relative fitness (y) versus temperature (x) for lake trout is $y = -0.077x + 4.14$ ($R^2 = 0.61$), for grayling is $y = -0.0497x + 3.77$ ($R^2 = 0.68$), and for char is $y = -0.0687x + 4.02$ ($R^2 = 0.84$).

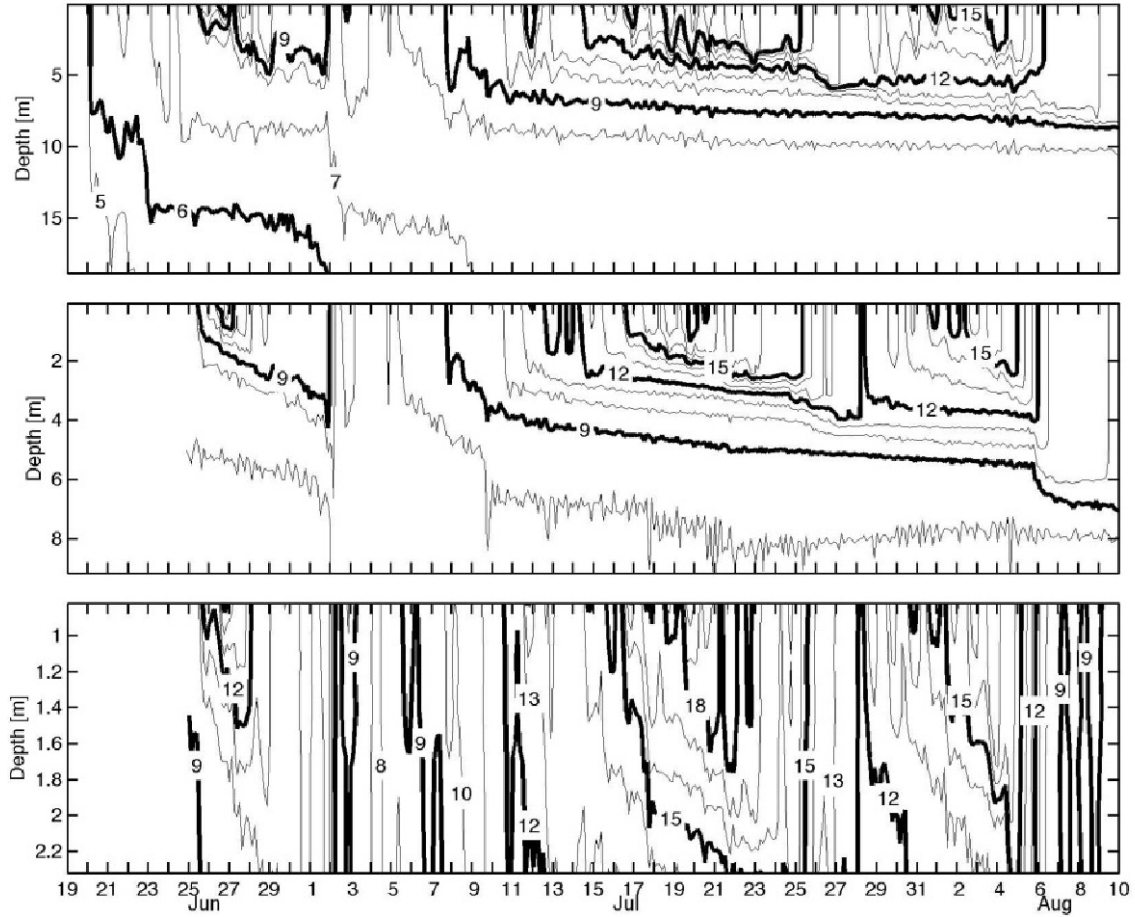


Fig. 8.V1. Time series of temperature (°C) in Toolik Lake (top panel) Lake E5 (middle panel) and Lake E6 (bottom panel) for mid-June to mid-August of 2002. Data were collected using self-contained temperature loggers placed at approximately 1m intervals in each of the lakes. Temperature contours are 1 °C.

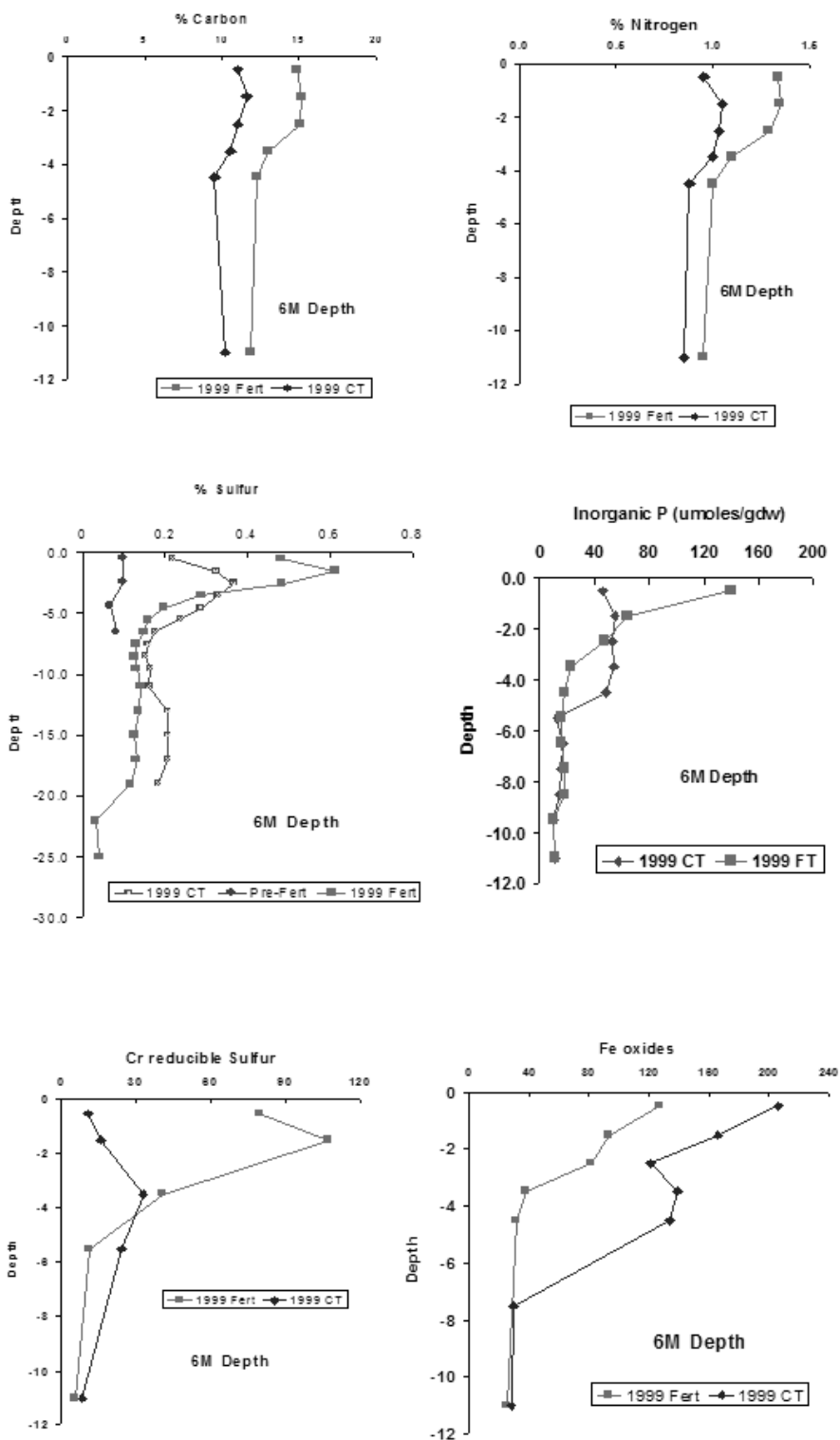


Fig. 8.V2. Carbon, nitrogen, sulfur, phosphorus, and iron in sediments of Lake N2.

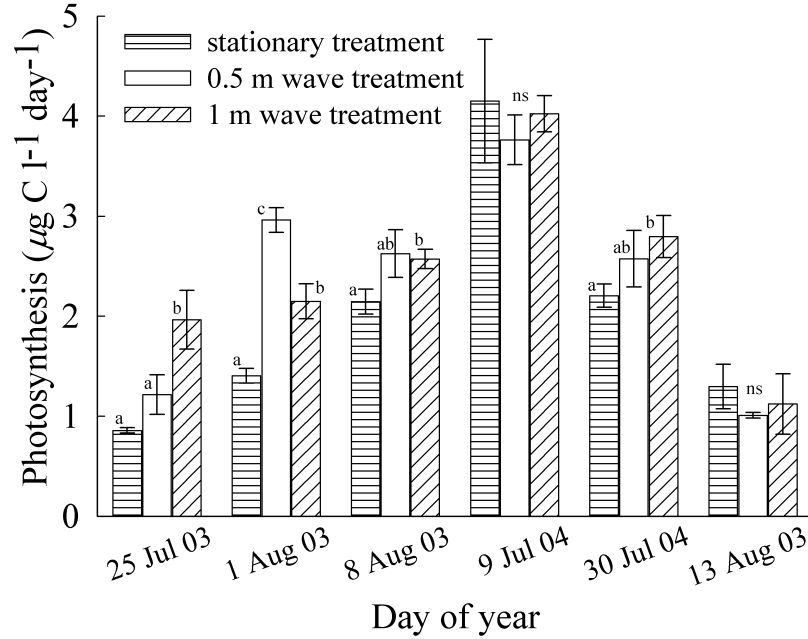


Fig. 8.V3. Phytoplankton primary production ($\mu\text{g C L}^{-1} \text{d}^{-1}$) from a series of *in situ* internal wave experiments in 2003 and 2004. Stationary treatments (depth = 5 m) had generally lower primary production than treatments in which phytoplankton were moved sinusoidally through the water column with average depth of 5 m, period of 4 h, and amplitude in the vertical of 0.5 m or 1 m. Statistically significant differences were indicated by the letters a, b, and c, where 'ns' indicates that there were no significant differences on that date.

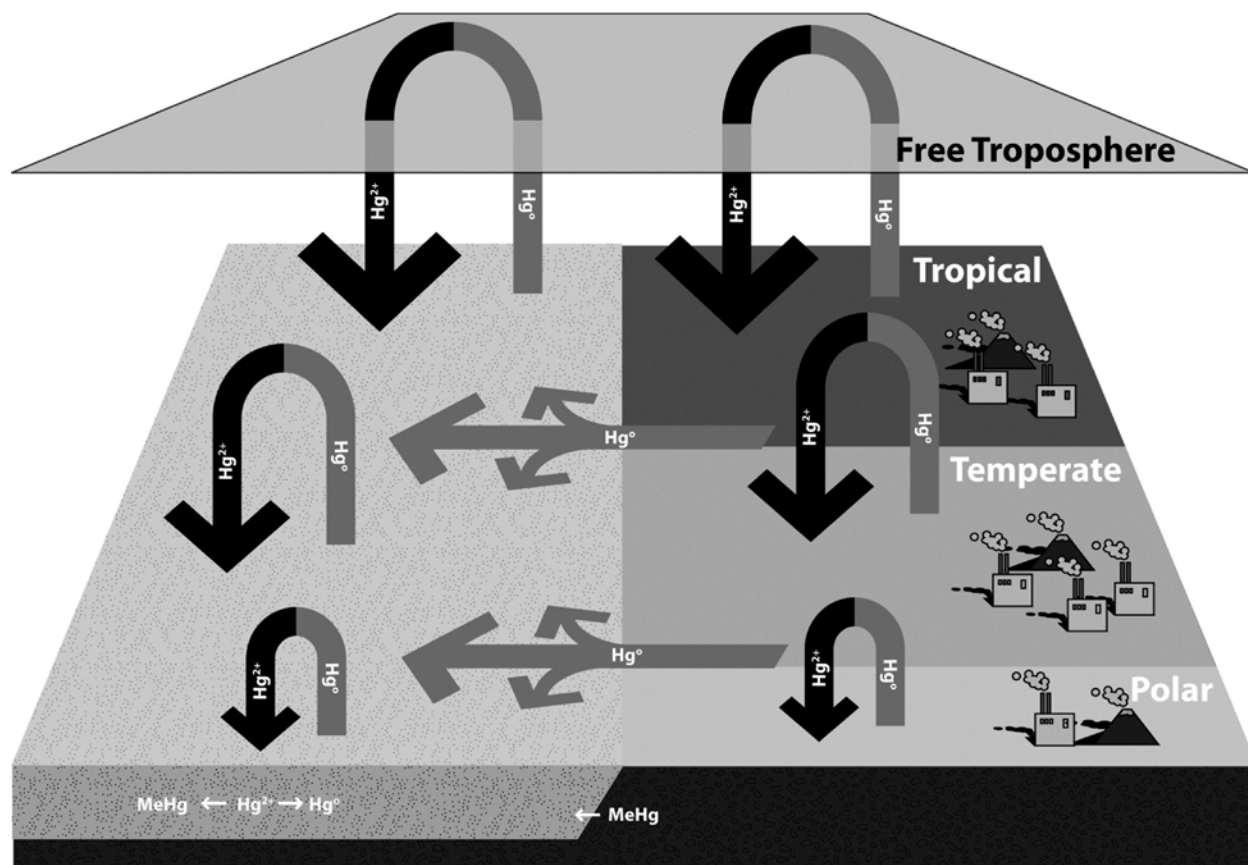


Fig. 9.1. Atmospheric Hg is dispersed globally, largely in the volatile elemental form (Hg^0). Natural and anthropogenic emissions to the atmosphere are sufficiently long-lived to allow intra-hemispheric mixing. Re-emission of this material, both from land and ocean, is a hallmark of the Hg cycle. Similar to that of POPs, Hg re-emission is accelerated by warmer temperatures, but apparently so is the removal of Hg from the atmosphere by oxidation and convective mixing of the lower and free troposphere. This likely prevents Hg from being “globally distilled” in the same way as POPs.

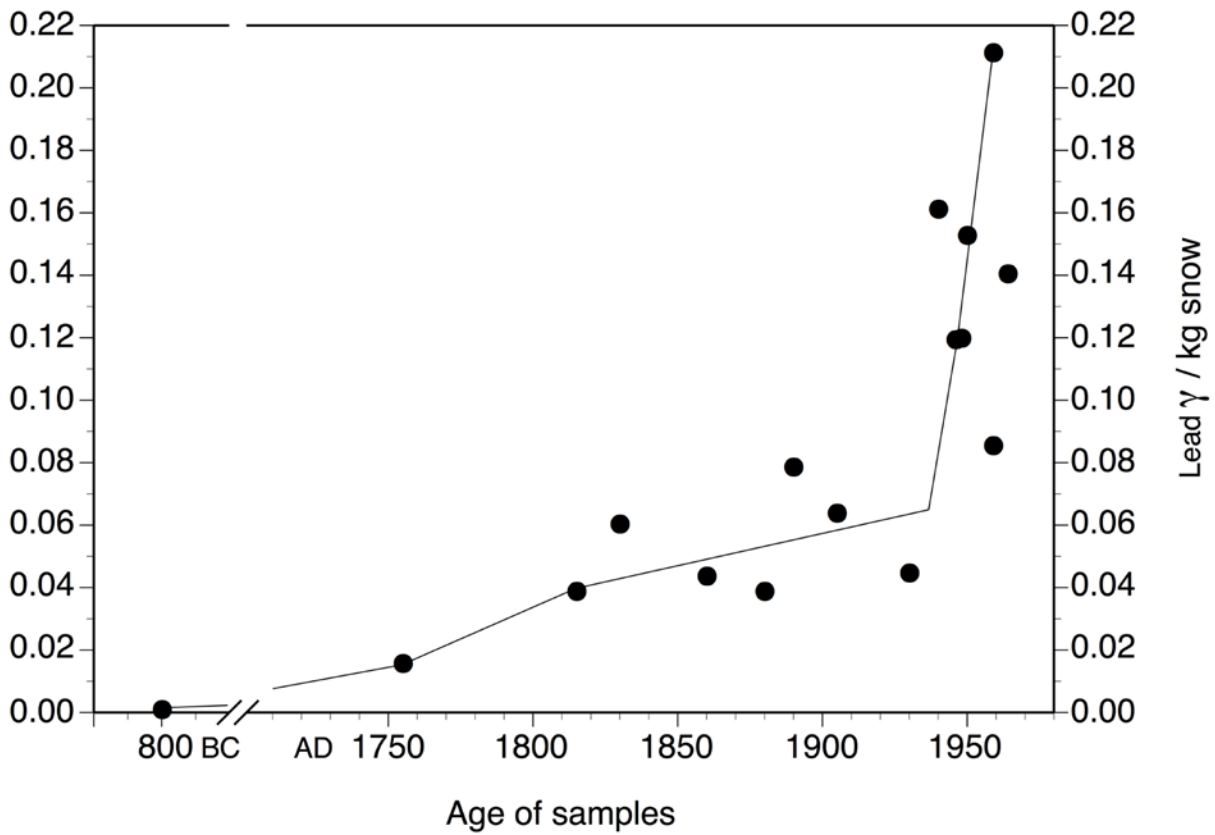


Fig. 9.2. Increase of industrial lead pollution in snow at Camp Century (Greenland) since 800 B.C. (from Murozumi et al. 1969 with permission).

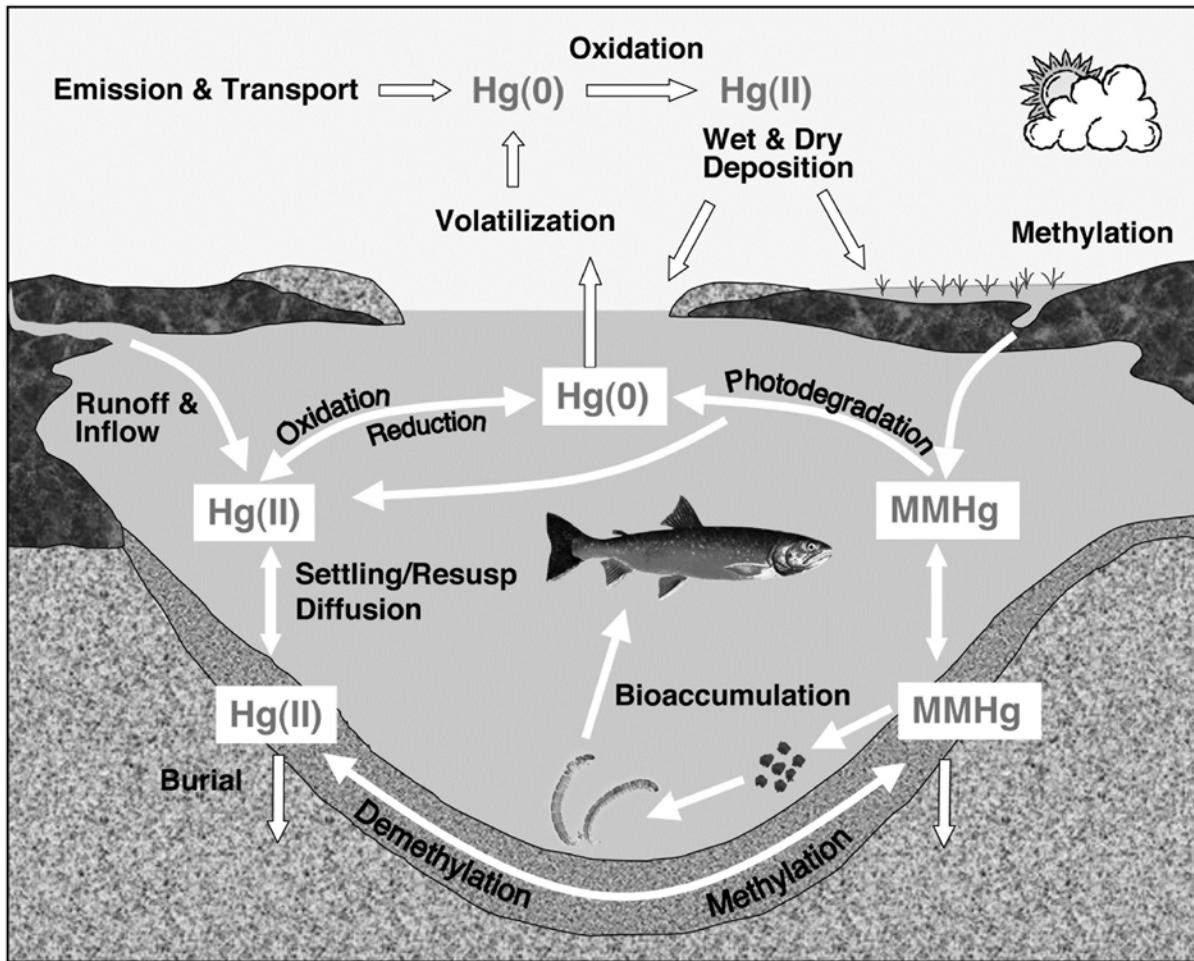


Fig. 9.3. Biogeochemical cycling of Hg in a tundra lake and its watershed. Gaseous elemental mercury [$\text{Hg}(0)$] is oxidized in the atmosphere to reactive gaseous mercury [$\text{Hg}(\text{II})$], and deposited in precipitation and by dry deposition. Bacteria convert a small portion of the incoming $\text{Hg}(\text{II})$ to monomethylmercury (MMHg), which is then bio-concentrated in the aquatic food chain. Various biotic and abiotic reactions interconvert the different forms of Hg, affecting uptake, burial, and evasion back to the atmosphere (data from Engstrom 2007).

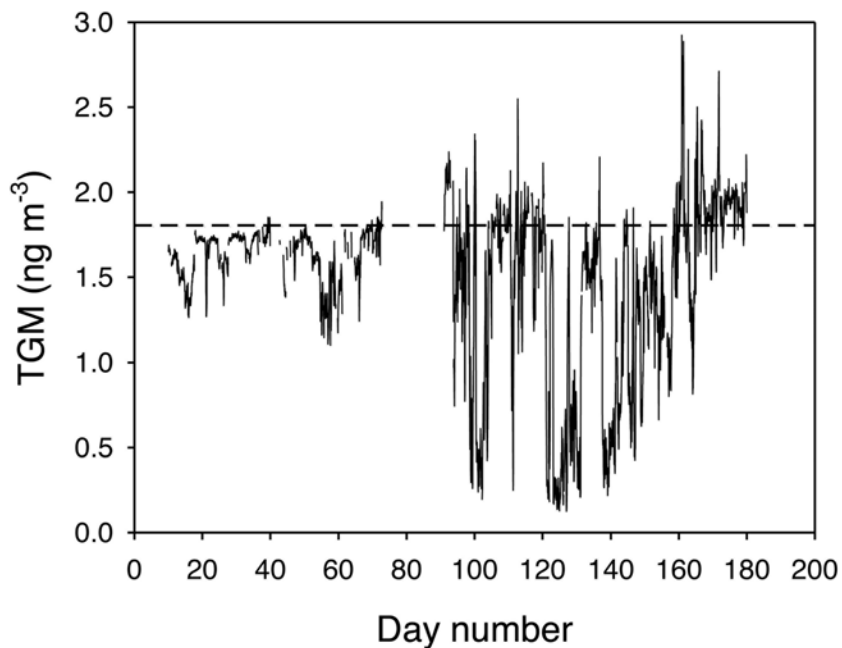


Fig. 9.4. Total gaseous mercury (TGM, > 99% as Hg⁰) in the atmosphere at (a) Alert, Canada, in 1995 (adapted from Schroeder et al. 1998 with the original data provided by S. Steffen). Dashed lines indicate “normal” TGM concentrations (~1.8 ng m⁻³). TGM is reduced significantly during atmospheric mercury depletion events.

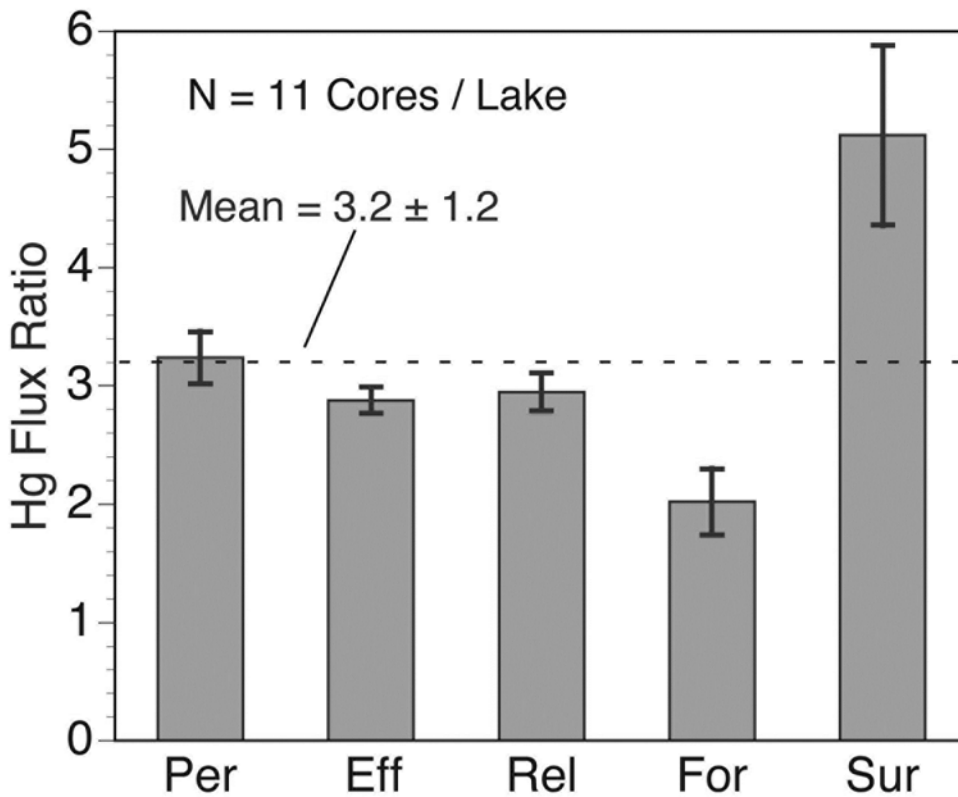


Fig. 9.5. Ratio of Hg accumulation in recent (1990-2000) to pre-industrial (pre-1850) sediments in five study lakes from the Toolik area. These lakes have been named provisionally as Perfect, Efficient, Relaxing, Forgetful, and Surprise (from Fitzgerald et al. 2005 with permission).

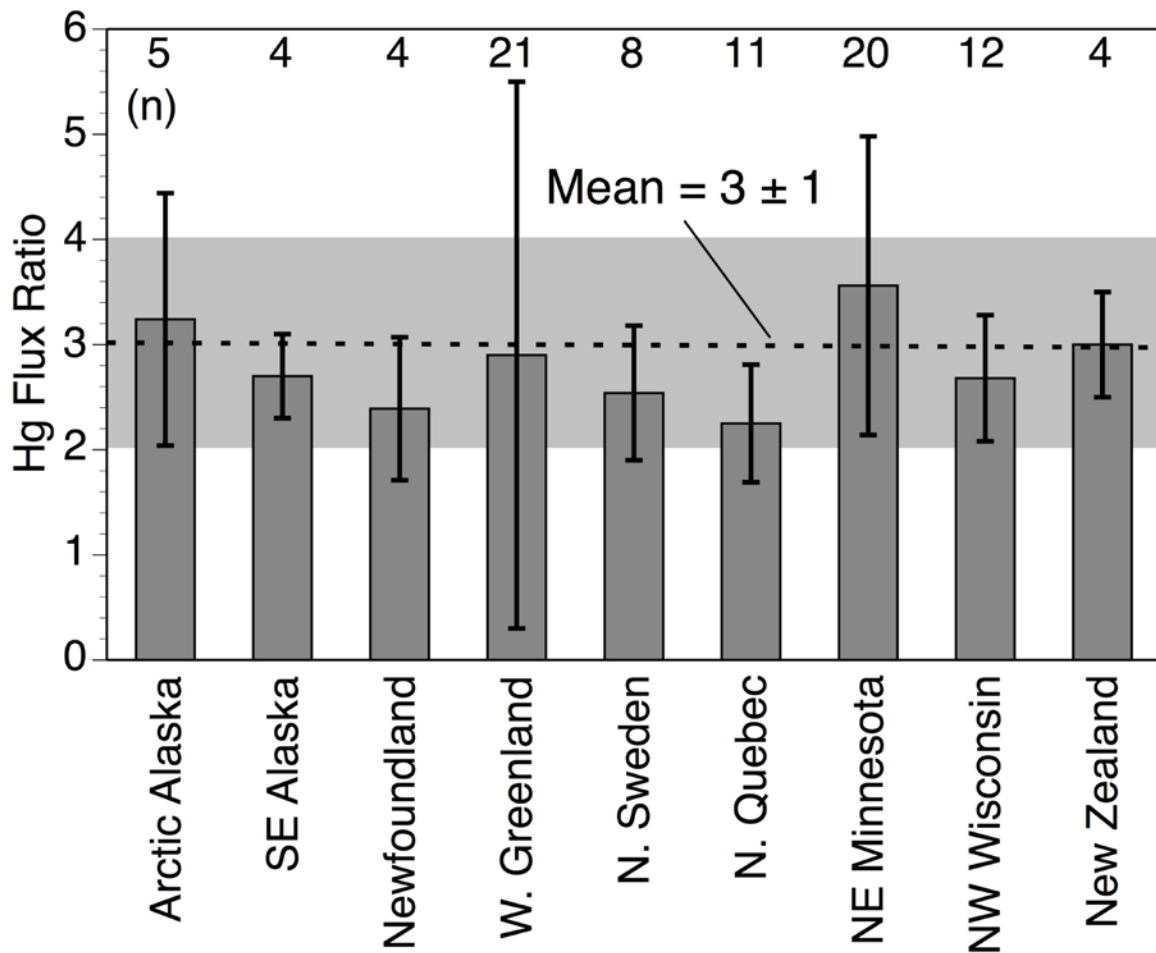


Fig. 9.6. Ratio of Hg accumulation in recent (1990-2000) to pre-industrial (pre-1850) sediments from remote lakes in various regions of the world (n = number of lakes in each study). Eleven cores were analyzed for each lake from arctic Alaska, and six cores per lake were analyzed from southeast Alaska and Newfoundland, one core per lake for all others. Data sources: arctic Alaska near Toolik (Fitzgerald et al. 2005); southeast Alaska and Newfoundland (the authors' unpublished results), northern Sweden (Bindler et al. 2001a); west Greenland (Bindler et al. 2001b); northern Quebec (Lucotte et al. 1995); northeastern Minnesota (Engstrom et al. 2007); north central Wisconsin (Rada et al. 1989); New Zealand (Lamborg et al. 2002).

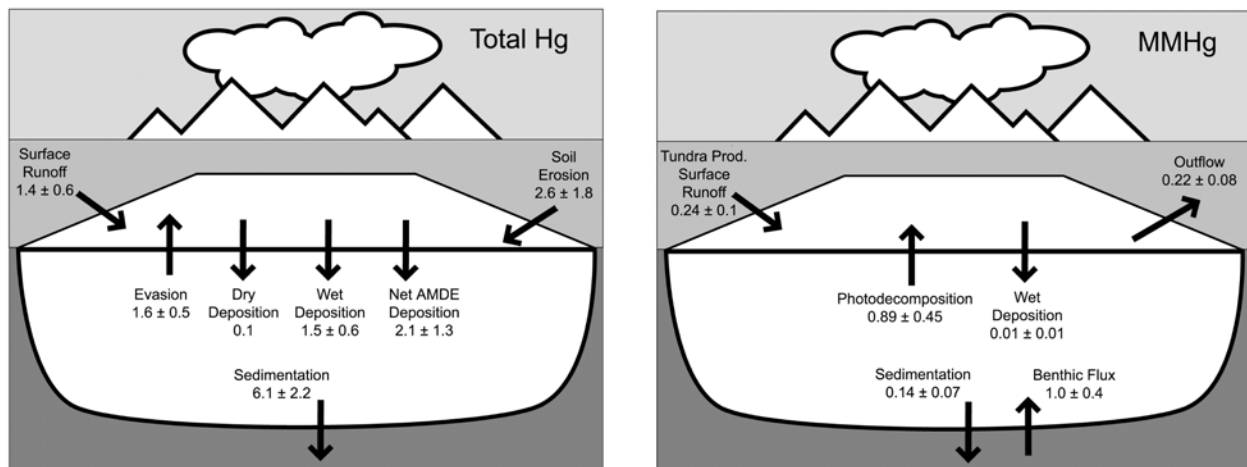


Fig. 9.7. Typical mass balance for (a) total Hg (Fitzgerald et al. 2005) and (b) monomethylmercury (MMHg; from Hammerschmidt et al. 2006 with permission) in small arctic lakes (fluxes are $\mu\text{g m}^{-2} \text{yr}^{-1}$). Total Hg cycling was examined in lakes without outflows.

Chapter 9 Vignette Figure Legends

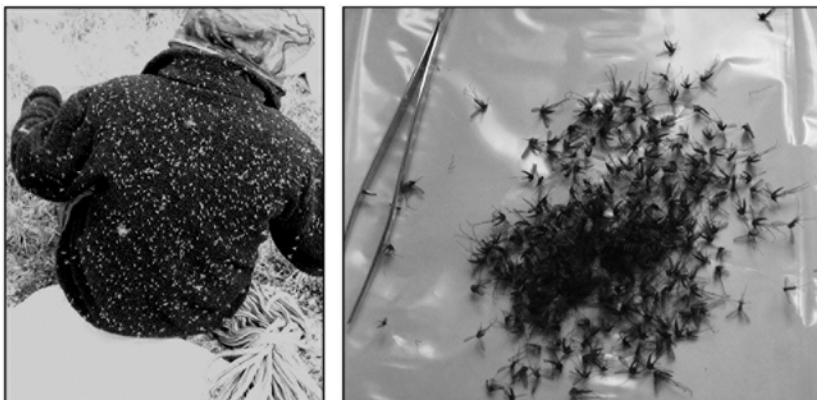


Fig. 9.V1. To the left is a tweed-like mosquito-laden jacket, and on the right collected arctic mosquitoes for MMHg analysis.

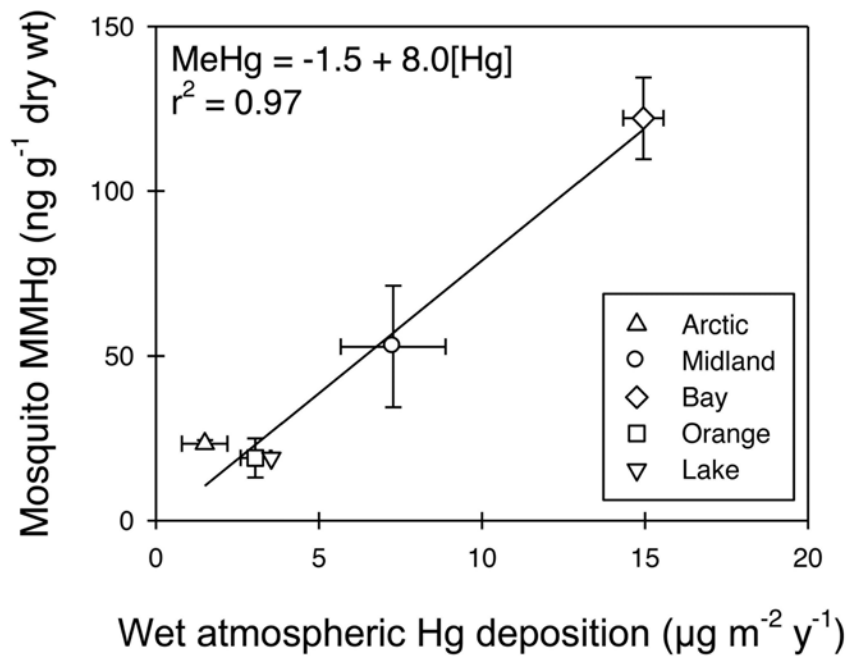


Fig. 9.V2. The mean concentration of MMHg in adult mosquitoes and wet atmospheric deposition of total Hg (± 1 standard error) at arctic tundra, AK; Midland County, MI; Bay County, FL; Orange County, CA; Lake County, CA (redrawn with data presented in Hammerschmidt and Fitzgerald 2005).